Thermodynamics of Low-Dimensional Interacting Quantum Systems: A Hybrid Exact Diagonalization and Density Matrix Renormalization Group Study

A DISSERTATION PRESENTED
BY
SUDIP KUMAR SAHA
TO
THE DEPARTMENT OF PHYSICS
UNIVERSITY OF CALCUTTA

SUBMITTED
FOR THE DEGREE OF
DOCTOR OF PHILOSOPHY (SCIENCE)
IN
PHYSICS (THEORETICAL)

2021

Dedicated to My Parents and my Grandfather Professor Manoranjan Shil

Acknowledgements

I am indebted to my Supervisor Dr. Manoranjan Kumar for his inspiration to pursue research work and his continuous support and patient guidance throughout the Ph.D. tenure. Working with him in several conferences has also helped me to be more familiar with the condensed matter research community.

I owe my deepest gratitude to Professor Zoltán G. Soos for his guidance and many fruitful suggestions throughout the thesis work. I would also like to express my appreciation to Dr. Shaon Sahoo and Dr. Tirthankar Dutta for their suggestions.

I would like to thank my seniors Dr. Dayasindhu Dey and Dr. Hrishit Banerjee for their excellent training in numerical techniques. They have taught me how to analyse and approach a research problem. The Ph.D. programme would not become successful without the guidance, supports and encouragements from the other seniors of our research group, Dr. Aslam Parvej, Dr. Rakesh Das, Dr. Sudipta Pattanayak, Dr. Debasmita Maiti, Monalisa Singh Roy, Dr. Joy Prakash Das, Dr. Santanu Pal, Dr. Sumit Haldar. My juniors, Sk Saniur Rahaman, Koushik Mandal, Jyotirmoy Sau, Monalisa Chatterjee, Manodip Routh, Somashree Ghosal and Sayan Ghosh also helped me to clear my ideas regarding the research topic through fruitful discussions.

I would like to thank S. N. Bose National Centre for Basic Sciences, Kolkata to provide me the opportunity to pursue the research work. I would also like to thank DST-INSPIRE for financial support throughout the Ph.D. tenure.

Publications

Papers to be included in the thesis:

- **Density matrix renormalization group approach to the low temperature thermodynamics of correlated 1d fermionic models**, Sudip Kumar Saha, Debasmita Maiti, Manoranjan Kumar, and Zoltán G. Soos, arXiv:2101.04362 [cond-mat.str-el] (2021).

- **Bond-bond correlations, gap relations and thermodynamics of spin-1/2 chains with spin-Peierls transitions and bond-order-wave phases**, Sudip Kumar Saha, Manoranjan Kumar, and Zoltán G. Soos, Journal of Magnetism and Magnetic Materials **519**, 167472 (2021).

- **Modeling the spin-Peierls transition of spin-1/2 chains with correlated states: $J_1 - J_2$ model, $CuGeO_3$, and TTF–$CuS_4C_4(CF_3)_4$**, Sudip Kumar Saha, Monalisa Singh Roy, Manoranjan Kumar, and Zoltán G. Soos, Physical Review B **101**, 054411 (2020).

- **Hybrid exact diagonalization and density matrix renormalization group approach to the thermodynamics of one-dimensional quantum models**, Sudip Kumar Saha, Dayasindhu Dey, Manoranjan Kumar, and Zoltán G. Soos, Physical Review B **99**, 195144 (2019).

Other publications :

- **Low temperature thermodynamics of the antiferromagnetic J_1J_2 model: Entropy, critical points, and spin gap**, Sudip Kumar Saha, Manodip Routh, Manoranjan Kumar, and Zoltán G. Soos, Physical Review B **103**, 245139 (2021).

- **Topological transitions to weyl states in bulk Bi_2Se_3: Effect of hydrostatic pressure and doping**, Sudip Kumar Saha, Hrishit Banerjee, and Manoranjan Kumar, Journal of Applied Physics **129**, 085103 (2021).

- **Haldane and dimer phases in a frustrated spin chain: an exact groundstate and associated topological phase transition**, Shaon Sahoo, Dayasindhu Dey, Sudip Kumar Saha, and Manoranjan Kumar, Journal of Physics: Condensed Matter **32**, 335601 (2020).

- **B-site disorder driven multiple magnetic phases: Griffiths phase, re-entrant cluster glass, and exchange bias in Pr_2CoFeO_6** Arkadeb Pal, Prajyoti Singh, V. K. Gangwar, Surajit Ghosh, P. Prakash, Sudip Kumar Saha, Amitabh Das, Manoranjan Kumar, A. K. Ghosh, and Sandip Chatterjee, Applied Physics Letters **114**, 252403 (2019).

- **Characterization of Majorana-Ising phase transition in a helical liquid system** Sudip Kumar Saha, Dayasindhu Dey, Monalisa Singh Roy, Sujit Sarkar, and Manoranjan Kumar, Journal of Magnetism and Magnetic Materials **475**, 257 (2019).

- **A study of topological quantum phase transition and Majorana localization length for the interacting helical liquid system**, Dayasindhu Dey, Sudip Kumar Saha, Prosenjit Singha Deo, Manoranjan Kumar, and Sujit Sarkar, Journal of the Physical Society of Japan **86**, 074002 (2017).

Contents

Listing of figures

1 Introduction

In the last couple of decades, electronic devices have become an integral part of human civilization and our dependence on these devices is growing day by day. The development of new theoretical ideas and synthesis of new materials have led to quantum jump in designing the smart and energy efficient devices. Recent discoveries of superconductors, semiconductors, and magnetic properties of materials have completely revolutionised the modern devices. Most of these exotic properties are controlled by the kinetic energy of electrons and Coulomb repulsion between them. However, study of competing kinetic and repulsive energy seems simple, but the many body nature of Coulomb repulsion makes the study complicated and challenging. Therefore, the study of the quantum many body system is one of the most challenging and active areas of research. In fact, this field of research is full of surprises due to the existence of various exotic phases in the condensed matter systems.

The quantum many body effect is omnipresent in condensed matter electronic systems, but it becomes dominant in low-dimensional systems due to confinement of electrons, for example, one dimensional (1D) Luttinger liquid systems [17–20] or a 1D interacting spin system where charge degrees of freedom is frozen and may have competing nearest and next nearest neighbor spin exchange interaction [21]. Sometimes the competing interactions may give rise to frustration in the system where a rich phase diagram is observed at low temperature T. In many fermionic systems charge and spin degrees of freedom can be active and may show metal-insulator transition, charge density wave, Néel order etc. There are many three dimensional

materials where the electronic activity is confined to only one direction and gives rise to an effective one dimensional electronic system. $LiCuSbO_4$ [22], $LiCuVO_4$ [23], $CuGeO_3$ [24] are some of the representative materials where only spin degrees of freedom is active and all the exchange interactions are confined to one direction. Similarly, the Alkali M-TCNQ salts (M = Na, K, Rb or Cs) are some of the best examples where electrons are confined in 1D [25].

In condensed matter system many body interaction is always present, but in some cases the repulsive Coulomb interaction is screened and the electrons behave like a single particle. In majority of the condensed matter systems the many body effect is an essential part. In a fermionic system each orbital can have four probable occupancy, i.e the number of degrees of freedom increases as 4^N where N is the number of orbitals. In spin systems where charge degrees of freedom is frozen, degrees of freedom goes as 2^N. Therefore, exact solutions of these systems are limited to small systems using exact diagonalization (ED). In most of the cases analytical solutions of many body model systems are nearly impossible. Later we will discuss those limitations in detail. Let's first introduce briefly the quantum many body models.

1.1 Brief introduction of quantum many body models

In condensed matter physics we deal with systems with large number (Avogadro number $N_A \sim 10^{23}$) of atoms or molecules in a mole. Each atom has nucleus and electrons with finite kinetic energy and these entities also interact with each other through Coulomb interaction. The simplest Hamiltonian can be written as

$$H = \frac{-\hbar^2}{2}\sum_{i=1}^{N}\frac{\nabla_i^2}{M_i} + \sum_{i=1}^{n}\frac{\nabla_i^2}{m_i} + \frac{1}{4\pi\varepsilon_0}\left(\sum_{i<j}^{N,N}\frac{Z_i Z_j e^2}{|\mathbf{R}_i - \mathbf{R}_j|} + \sum_{i,j}^{N,n}\frac{Z_i e^2}{|\mathbf{R}_i - \mathbf{r}_j|} + \sum_{i<j}^{n,n}\frac{e^2}{|\mathbf{r}_i - \mathbf{r}_j|}\right). \quad (1.1)$$

In Eq. 1.1, M_i, m and Z_i are masses of the positively charged nucleus of atom, the electron and the atomic number of the i^{th} atom, respectively. R_i and r_i are the coordinates of i^{th} nucleus and electron. N and n are the numbers of nucleus and electrons respectively. In limit of Born-Oppenheimer approximation the nuclei degrees of freedom can be ignored as the mass of nucleus is much larger than that of electron, and nucleus motion can be safely assumed to be frozen. Therefore, interacting electrons can be moving in a stationary potential background generated by the nucleus or ions. The Hamiltonian in Eq. 1.1 can be

simplified and written only for electronic degrees of freedom as

$$H = \frac{-\hbar^2}{2}\sum_{i=1}^{n}\frac{\nabla_i^2}{m_i} + W(\mathbf{r}_i) + \sum_{i<j}^{n,n}\frac{e^2}{|\mathbf{r}_i - \mathbf{r}_j|}. \tag{1.2}$$

The first term corresponds to kinetic energy or hopping term of electrons, and the second term corresponds to chemical potential or site energy which takes care of all the background potential energy as well as atomic properties of system. The third term accounts for the summation of all the interactions between electrons.

For a fermionic system where both the spin and charge degrees of freedom are active, the Hamiltonian in Eq. 1.2 can be expressed in terms of fermionic operators in second quantization [26] as

$$\begin{aligned} H &= \sum_{ij} H_{ij} c_i^\dagger c_j + \frac{1}{2}\sum_{ijkl} V_{ijkl} c_j^\dagger c_l^\dagger c_k c_i, \\ H_{ij} &= \int d^3 r \theta_i(\mathbf{r})^* \left[\frac{-\hbar^2}{2m}\nabla^2 + W(\mathbf{r})\right] \theta_j(\mathbf{r}), \\ V_{ijkl} &= \int d^3 r_1 \int d^3 r_2 \theta_j(\mathbf{r}_1)^* \theta_i(\mathbf{r}_1) V(\mathbf{r}_1 - \mathbf{r}_2) \theta_l(\mathbf{r}_2)^* \theta_k(\mathbf{r}_2). \end{aligned} \tag{1.3}$$

Here, the operators $c_i^\dagger(c_i)$ create (annihilate) an electron at site i and $\theta_i(\mathbf{r})$ are the set of basis configuration (orbitals) for the fermionic system. The first term in the first part of the Hamiltonian accounts for the hopping of electrons between sites i and j and the second term is the site energy. The second part in Eq. 1.3 depicts the Coulomb interaction term between electrons.

The Eq. 1.3 reduces to the simplest fermionic model when the electron hopping is restricted to only between nearest neighbor sites and Coulomb interaction is effective only if two electrons sit on the same site. The Hamiltonian can be represented as

$$H = -t\sum_{<i,j>,\sigma}(c_{i,\sigma}^\dagger c_{j,\sigma} + h.c.) + \mu\sum_{i,\sigma} c_{i,\sigma}^\dagger c_{i,\sigma} + U\sum_i n_{i,\uparrow} n_{i,\downarrow}. \tag{1.4}$$

Here, the operators $c_{i,\sigma}^\dagger(c_{i,\sigma})$ create (annihilate) an electron with spin σ at site i, $h.c.$ is the Hermitian conjugate and $n_{i,\sigma} = \sum_\sigma c_{i,\sigma}^\dagger c_{i,\sigma}$ is the number operator. The first term denotes the hopping of electrons between nearest neighbor sites, t is transfer integral term between site i and j. The second term is the site energy or chemical potential energy of a site and controls the electronic population. The third term ac-

counts for the onsite Coulomb repulsion between electrons sitting at the same site with opposite spins and U is Coulomb energy integral on involving same four orbital terms.

The Hubbard model can be analyzed in different limits of parameters and it is interesting to see the effect of strong interaction U in the Hubbard model and various limits of hopping term t limits. In the atomic limit at $t = 0$, the energy levels are largely degenerate and increasing t leads to band formation or metallic behaviour. For a fermionic system at half-filling and in large U limit the doubly occupied sites are not energetically preferable and hopping of electrons is hindered in order to avoid the double occupancy of sites. The electrons' spins have antiferromagnetic (AFM) arrangement on the lattice and stay localized to avoid the double occupancy formation. In strong U limit the system opens a gap of order U. At $U \to \infty$, the charge degrees of freedom is completely frozen and only spin degrees of freedom persist. This metal to insulator transition as a function of U/t is called Mott transition.

Each site in a fermionic system can be occupied in four possible ways, i.e., it can be empty ($|0\rangle$), occupied with single electron with either up or down spin orientation ($|\uparrow\rangle$ or $|\downarrow\rangle$) or doubly occupied with spin up and down ($|\uparrow\downarrow\rangle$). In large U limit and at any arbitrary filling, the low energy spectrum does not have contribution from doubly occupied sites, each site is associated with three possibilities, i.e., $|0\rangle$, $|\uparrow\rangle$ and $|\downarrow\rangle$. The effective Hamiltonian for the low energy spectrum at large U can be written as

$$H_{tJ} = -t \sum_{<i,j>,\sigma} \left[(1 - n_{i,-\sigma}) c^{\dagger}_{i,\sigma} c_{j,\sigma} (1 - n_{j,-\sigma}) + h.c. \right] + \frac{4t^2}{U} \sum_{i} \left[\vec{S}_i \cdot \vec{S}_j - \frac{n_i n_j}{4} \right]. \tag{1.5}$$

Here, fermionic operators bear the same meaning as in Eq. 1.4. $\vec{S}_i$ is the spin vectors at site i. This model is known as $t-J$ model [26]. The first term represents the hopping of electrons without creating the double occupancy. The third term is antiferromagnetic interaction between nearest neighbor spins with exchange strength $J = 4t^2/U$.

The Eq. 1.5 suggests that electron hopping sustains in a fermionic system away from half filling even at $U \to \infty$. However, at exactly half-filling and the large U limit, Eq. 1.5 reduces to Heisenberg antiferromagnet (HAF) where electrons are completely localised and sites are singly occupied. The Hamiltonian of HAF is shown below.

$$H = J \sum_{<i,j>} \vec{S}_i \cdot \vec{S}_j. \tag{1.6}$$

Here J can be written as $J = 4t^2/U$.

1.2 Significance of quantum many body models in condensed matter physics

In the last section we studied various models starting from original model where all the degrees of freedom ware taken into account and slowly remove various degrees of freedom which are less important. Therefore, it is important to convince ourself whether these models are relevant in modelling some real materials. We study the application of spin model system and thereafter we will see the fermionic systems.

1.2.1 Spin models

As already stated, a large number of materials are insulator but they exhibit interesting magnetic properties like $LiCuSbO_4$ [22], $LiCuVO_4$ [23] and $CuGeO_3$ [24], these are some of well known low dimensional cupric oxides materials where spin-1/2 Cu(II) ions effectively form frustrated quasi-1D spin chains with AFM next nearest neighbor spin interaction which give rise to frustration in the system for irrespective of the nature of nearest neighbor interaction. These systems can be represented by $J_1 - J_2$ model [23, 24]. The model has one spin-1/2 per unit cell and isotropic exchange J_1 and $J_2 > 0$ with nearest and next nearest neighbor neighbors, respectively. The Hamiltonian of $J_1 - J_2$ model for one dimensional system is shown in the equation below.

$$H = J_1 \sum_r \vec{S}_r \cdot \vec{S}_{r+1} + J_2 \sum_r \vec{S}_r \cdot \vec{S}_{r+2}. \tag{1.7}$$

Here $\vec{S}_r$ is the spin operator acting on spin on the site at position r along the 1D chain. The frustration can be visualized as the competition between exchange interaction J_1 and AFM J_2 which makes the spins in the system confused about which possible spin orientation to choose. AFM nearest exchange J_1 forces antiferromagnetic arrangement of spins therefore next nearest neighbor should be ferromagnetic (FM) but presence of AFM next nearest neighbor J_2 can lead to frustration. Similarly ferromagnetic J_1 forces all spins to be up but AFM J_2 prefers the next nearest neighbor spin to be anti-parallel. The frustration results in a rich phase diagram in the ground state (gs) of $J_1 - J_2$ model [21]. Various exotic phases in the system for either FM nearest neighbor exchange $J_1 < 0$ or AFM $J_1 > 0$ depends on the frustrated exchange interaction J_2. For $J_2 \to 0$, the gs is gapless FM chain if $J_1 < 0$, and for AFM J_1 it is gapless AFM with quasi-long range order(QLRO) (in Eq. 1.6). At very high J_2, the model behaves like two independent AFM

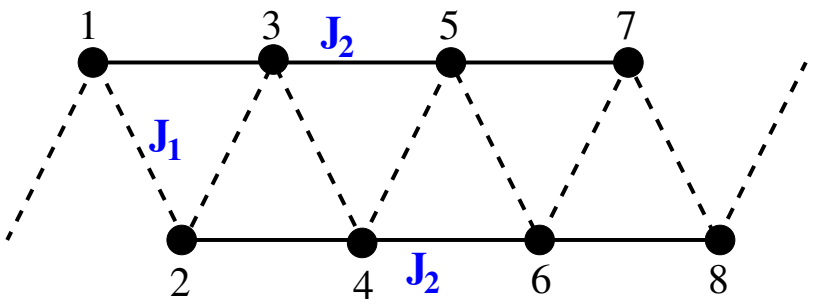

Figure 1.1: The frustrated $J_1 - J_2$ model on a zigzag ladder. The interaction between spins along each of the leg is J_2 and J_1 accounts for the interaction along the rung.

spin chain [21, 27]. The $J_1 - J_2$ model can be represented as a quasi-1D zigzag ladder as shown in Fig. 1.1. The interaction between spins along each of the leg, i.e., the interaction between odd-numbered sites and the interaction between even-numbered sites, is J_2 and J_1 accounts for the interaction along the rung. If J_1 is negligible compared to J_2, the frustrated zigzag ladder behaves as two independent HAF on the two legs which are the sublattice with odd- and even-numbered sites. This phase corresponds to the decoupled phase [21, 27] in $J_1 - J_2$ model. The pitch angle between neighboring spin orientations is zero and π in FM and AFM phase, respectively, whereas in the decoupled phase neighboring sites have spin orientation $\pi/2$ with respect to each other. For the FM J_1 and intermediate values of J_2, the gapped spiral phase persists where the pitch angle increases from 0 in the FM phase to $\pi/2$ in the decoupled limit. Within this limit, the critical point at $J_2 = |J_1|/4$ [28] separates the FM gs and the gapped incommensurate (IC) singlet gs [29].The AFM J_1 ($J_1 > 0$) with intermediate J_2 also suffices for pitch angle between $\pi/2$ and π. For AFM J_1 gs goes from a QLRO phase to dimer phase at [30] $J_2/J_1 = 0.2411$. In the dimerized phase, nearest neighbor spins form singlet pair and doubly degenerate gs. For ($J_2 = J_1/2$) this model is well known as Majumdar-Ghosh [31] (MG) model.

Charge transfer (CT) salts [32] are another interesting area for the application of the 1D and quasi-1D models. For example, the TCNQ (tetracyanoquinodimethane) salts are widely studied system in the literature and these salts are the charge transfer (CT) salts in presence of π-donors like TTF (tetrathiafulvalene). In CT materials donors and acceptors stack face to face to facilitate the charge transfer from donor to acceptor along the stack. The stacking and charge transfer along a particular direction in the system make it a possible candidate for application of 1D or quasi-1D models. The transition from neutral to ionic phase in these systems is well known in the literature. The gs is neutral in presence of weak donors. On the other hand, in presence of strong donors, the ionic gs is preferable due to transfer of electrons. The TTF-TCNQ

is well known in the literature to be modelled successfully with HAF at moderate T. Whereas, at low T it faces structural dimerization, i.e., spin-Peierls transition [2].

1.2.2 Fermionic models

Beside spin models, 1D and quasi-1D fermionic models with both active charge and spin degrees of freedom are more general models and also play an important role to explain various exotic properties in many condensed matter systems. They have also been applied successfully to explain the electronic and magnetic properties organic salts and polymers [33–35]. The simplest and most widely studied fermionic model is the Hubbard model Eq. 1.4. For a uniform site energy μ the second term is just a constant term for a given number of electrons, the Hamiltonian for a chain can be rewritten without site energy μ as

$$H = -t \sum_{r,\sigma} (c^{\dagger}_{r,\sigma} c_{r+1,\sigma} + h.c.) + U \sum_{r} c^{\dagger}_{r,\alpha} c^{\dagger}_{r,\beta} c_{r,\beta} c_{r,\alpha}. \tag{1.8}$$

Let's consider a system with half-filled electrons, i.e., the electron fraction is $n = N_e/N = 1$ where N is the number of sites and N_e is the total number of electrons present in the system. In absence of the onsite interaction U this model is called 'tight binding model' which can explain the metal to band insulator behavior in the system. We have discussed in section 1.2 that U tries to suppress double occupancy of electrons at a site and hopping of electrons can create double occupancy. In strong U limit electrons are localised and electrons can only exchange their spins. Therefore, these systems have well separated spin and charge excitations. Later we will show explicitly in Chapter 5 that the low energy spectrum at large U can be successfully described by spin Hamiltonians.

The extended Hubbard model (EHM) is another widely studied model where Coulomb interaction is extended to next nearest neighbor with strength V and this term is present in addition to the hopping t and onsite interaction U term. The Hamiltonian of EHM can be written as

$$H = -t \sum_{r,\sigma} (c^{\dagger}_{r,\sigma} c_{r+1,\sigma} + h.c.) + U \sum_{r} c^{\dagger}_{r,\alpha} c^{\dagger}_{r,\beta} c_{r,\beta} c_{r,\alpha} + V \sum_{r} n_r n_{r+1}. \tag{1.9}$$

In the half-filled and at large U, the gs is contributed by singly occupied sites, whereas the alternately unoccupied and doubly occupied sites are preferred at large V. The competition between U/t, and V/t leads to

an interesting phase diagram [36, 37]. Above a certain value of $U = U^*$, the transition from spin density wave (SDW) at low V to charge density wave (CDW) at large V is first order since the bond order across the transition changes discontinuously. Below U^* the change in the bond order is continuous and the transition from SDW to CDW is 2^{nd} order. In this region, the existence of a narrow bond-order wave (BOW) phase between SDW and CDW phase is supported in the literature [36, 37]. In the BOW phase the gs of the system is doubly degenerate and has a finite spin gap.

Let's return back to the discussion of the organic salts. While TCNQ ion with organic ligands forms CT salts with mixed stacking of donors and acceptors, it also forms isolated stack of acceptors or donors in presence of inorganic cations. These systems are modelled successfully in the literature with 1D fermionic models [25, 38]. At high T, Alkali M-TCNQ salts (M = Na, K, Rb or Cs) T have uniform stack of TCNQ ions and forms an effective 1D systems. Alkali-TCNQ salts can be modelled using 1D EHM with half-filled electron at higher T. This model suggests that alkali-TCNQ materials are at boundary of the (BOW) and the CDW and the existence of a finite value of V is necessary to model these systems. The properties of Na and K -TCNQ salts for $T > T_s$ are successfully explained with CDW phase and Rb(II) salt by BOW phase of EHM [25]. While the stackings are uniform at higher T and the inversion symmetry at each site is spontaneously broken. It undergoes a transition to dimerized stackings at lower $T (T < T_s)$ due to Peierl's instability [38].

Some organic salts, for example, TTF-CA (tetrathiafulvalene-chloranil), are associated simultaneously with Peierls transition and neutral to ionic transition [39]. The uniform stacking is associated with neutral phase, while the ionic phase accompanies the dimerized phase. These salts are also good candidates for the application of the fermionic models along with the incorporation of the Peierls instablility [39]. We have studied the Peierls transition in spin systems and will be discussed in detail in Chapter 4.

The fermionic models away from half filling are relatively less studied in the literature than the half-filled models. Many of the studies are performed using analytical solution of the model and the existing numerical methods are restricted with their own limitations. One of the example is quantum Monte Carlo method (QMC), which is very efficient at half filling, fail for the system with filling away from the half filling. The gs properties of 1D Hubbard model are studied by H. Shiba [16] for variable filling fraction of electrons. The properties of many condensed matter systems can be only understood by employing these models. Experiments have revealed charge ordered phase in the inorganic compound NaV_2O_5 [40]. All

the V ions in this compound are equivalent with valence $V^{4}.5+$ at moderate T. On cooling below a transition T, the valency changes allowing the coexistence of two inequivalent V ions as $V^{4}+$ and $V^{5}+$ [40]. This phase is also found in organic compounds $(TMTSF)_2X$ where X=PF_6, ClO_4 and $(TMTTF)_2Y$ with Y=PF_6, AsF_6 [41, 42]. The compounds allowing the charge ordered phase are explained in the literature using the quarter-filled fermionic models [43–46].

The correlated nature of the electrons in these materials makes it hard to model the electronic properties. Most of numerical techniques fail to solve model Hamiltonian required to model these systems. Some of the numerical technique like QMC can used to solve the system with half filling, but it fails to give accurate results for system away from half filling. The density matrix renormalization group (DMRG) method is one of state of art method to solve these models efficiently in 1D or quasi-1D systems. The gs properties like correlations functions and spin or charge density or spin gaps are accurately calculated for quarter-filled ionic Hubbard model using the DMRG method [47]. The explicit studies of quantum phase diagram at very low filling is still lacking in the literature. The study of the finite T properties requires full spectrum of the system and thus it is more difficult to calculate numerically. The insufficiency is more prominent in case of extended Hubbard model and the study of the thermodynamics of EHM away from half-filling is rare in the literature.

1.2.3 Modelling of the spin-Peierls transition

We have discussed a few 1D quantum models and their importance in modelling of various condensed matter systems in the previous sections. In order to comprehend various aspects of the condensed matter physics, theoretical modelling should go hand in hand with experimental findings. In condensed matter physics it is an ideal approach to observe the experimental results and connect the appropriate effective quantum models with those observations to understand the properties of the system. However, experiments mostly provide finite T properties instead of the gs, and therefore, the solution of the model Hamiltonian at finite T is inevitable. Most of the experimentally observed results are at finite temperature and phase transitions may be temperature driven, for example, the spin-Peierls (SP) transition. Most of the analysis or modelling of these observations are done in mean field limit and accurate study of these systems using quantum models with correlated states is still lacking. The SP systems are studied in this thesis work at finite T with correlated states in Chapter 4. So let's briefly discuss the SP transition.

The SP transition occurs in a few 1D or quasi-1D AFM spin systems if they are cooled below a transition $T < T_{SP}$, and a specific ordering of spin in the system occurs which is similar to the Peierls transition in quasi-1D metallic systems [3]. Rudolf Peierls proposed a theorem at 1930 which states that a one-dimensional half-filled metal with equally spaced ions is unstable [48]. A quasi-1D half-filled metal encounters Peierls transition in which two neighboring bonds have unequal length or doubling of unit cell occurs below a critical temperature T_p. At higher temperature $T > T_p$, all ions in the metallic chain are separated from their neighboring ions by an equal lattice spacing a. In this regular system band gap is zero and first Brillouin zone has boundary at $k = \pm\pi/a$. Each ion are donating one electron to the chain leading to half filling and bands are filled upto $k = \pm\pi/2a$.

In case of Peierls distortion atoms shift close to one of its nearest neighboring atom and moves away from the other nearest neighbor as a result of electron-phonon interaction. This structural change causes doubling of the lattice periodicity, i.e., the periodicity changes from a to $2a$, that leads to reduction of the Brillouin zone. The Brillouin zone boundary shifts from $k = \pm\pi/a$ to $k = \pm\pi/2a$ which is the location of the last filled state at the gs. As a result, a gap at the Fermi energy is introduced in the band. The distortion in lattice leads to Fermi energy being lower in energy compared to that of a regular lattice. In this system structural distortion costs elastic energy which competes with the gain in electronic energy. The Peierls instability occurs when elastic energy is lower than the electronic energy, and the opening of the gap at the Fermi energy leads to metal to insulator transition.

There are only a few 1D or quasi-1D AFM spin systems which have short range ordering at low T along with elastic distortion leading to a dimerized structure. This transition is known as spin-Peierls (SP) transition due to the similarity to a Peierls transition discussed above. In this case the there is opening of spin gap rather a band gap and these systems are insulator at all T. These systems have regular structure with uniform spacing between spin sites for $T > T_{SP}$ and form a dimerized structure for $T < T_{SP}$. Dimerization leads to increase of lattice free energy and the closer spins in the distorted lattice tend to form stronger singlet pairing and results in higher magnetic gap. If change in magnetic free energy becomes equal to or exceeds change in lattice free energy, the system dimerized spontaneously. The equilibrium dimerization $\delta_{SP}(T)$ in the system is T dependent quantity and $\delta_{SP}(T)$ is 0 at high T. Below $T > T_{SP}$ $\delta_{SP}(T)$ decreases with temperature and the magnetic gap is proportional to $\delta_{SP}(T)$, therefore, magnetic gap is also a function of T in a spin-Peierls system.

The SP transition was first found in the organic compound $TTFCuS_4C_4(CF_3)_4$ [2]. The TTF cations form effective 1D spin-1/2 chain via superexchange through $CuS_4C_4(CF_3)_4$ anions. The measured magnetic susceptibility χ shows sudden drop at $T_{SP} = 12$ K because of the increase in the magnetic gap. In inorganic crystal Hase et al. [4, 5] identified spin-Peierls transition in $CuGeO_3$ where spin-1/2 of Cu(II) ions form spin-1/2 AFM quasi-1D chain. A sudden drop in χ is observed for $T < T_{SP} = 14$ K . [4, 5]. The excitation gap was measured through inelastic neutron scattering (INS) in several studies [9–12] and all of them shows sharp increase of singlet to triplet (ST) gap near $T_{SP} = 14$ K supporting the criteria for SP transition. Soon after these findings, the SP transition became a subject of interest among scientists. Beside experimental observation, proper modelling of SP systems are inevitable to understand the SP transition.

The gs of some simple systems like uniform HAF spin-1/2 can be exactly solved through Bethe Ansatz, but for most of the correlated spin system calculations are intractable with analytical approaches. Therefore, most of reliable results for frustrated spin model systems can be obtained using numerical methods [21, 23, 27, 49–52]. Exact theoretical solution in presence of alternating exchange interaction along spin chains and spin-phonon coupling is almost impossible. There are several numerical approaches that can target the finite T properties for uniform spin systems, such as transfer matrix renormalization group (TMRG), QMC (only for non-frustrated systems). The literature mostly analyze the SP systems using correlated states for $T > T_{SP}$, but only as mean field for $T < T_{SP}$. The proper modelling of SP transition using correlated states is still lacking in the literature. Our development of hybrid ED/DMRG is one possible approach for the analysis of SP system for $T < T_{SP}$ which will be discussed in Chapter 3.

1.3 Obstacles in solving quantum many body models

The bottleneck in solving the quantum many body model Hamiltonian at finite T is one of motivation behind the development of the hybrid ED/DMRG. In a many body system, any state of the system is a linear combination of different basis or configurations, and the number of basis increases exponentially with system size. As a result, the dimension of the many body Hamiltonian matrix becomes gigantic, therefore, intractable for the exact solution even numerically. Several numerical techniques have been developed over time to calculate the gs of spin systems i.e., quantum Monte Carlo (QMC) [1], numerical renormalization (NRG) [53], density matrix renormalization group (DMRG) method [54], tensor net-

work [55] etc. Unfortunately only non-frustrated systems can be solved using the QMC [1] and NRG is only restricted to impurity problems. The numerical calculation of various properties at finite T is more difficult as it requires full spectrum. Although, several numerical methods have been developed until now to approach the finite T properties of quantum many body systems, but these techniques have their own limitations. Let us briefly discuss some of the existing methods to solve quantum many body models and their limitations.

1.3.1 Limitation of quantum Monte Carlo method (QMC)

The exact diagonalization (ED) has made possible the accurate calculation of the thermodynamic properties of quantum many body systems of small system size. Although different symmetry operations relevant to a particular quantum models enable us to explore slightly larger system size and the thermodynamic limit is reachable with ED at high T where correlation length becomes very small due to thermal fluctuations, the study of the thermodynamic limit in most of the models at low temperature(T) where quantum fluctuation is still dominant is beyond the reach of ED. The development of quantum Monte Carlo method (QMC) was the first efficient key to overcome this numerical limitation as it is capable of solving large enough system size for accurate extrapolation to the thermodynamic limit which is essential in condensed matter physics.

Today the QMC based on Stochastic Series Expansion (SSE) has become one of the most efficient and widely used tools among other variations of the QMC [1] to solve some of the quantum many body models (which do not encounter sign problem). The development of SSE approach is pioneered by Handscomb who introduced a method to solve FM Heisenberg chain using Taylor expansion of the partition function and exact calculation of the trace of the Hamiltonian analytically [56]. Later QMC related to path integral was proved to be more efficient numerical approach [57, 58]. In this method the quantum system of d-dimensions is represented as an equivalent classical system of $d+1$-dimensions. The SSE approach is an improved and more efficient version of the Handscomb approach where traces of the operators are sampled using Monte Carlo method [1]. The SSE approach has been applied successfully to models of variable spin size [59, 60], models with long-range interaction [61], cold atoms trapped in optical lattices [62]. Let us discuss briefly about the SSE QMC method and its limitation.

The thermal average of any operator can be expressed using the partition function Z which is the trace

of the Boltzmann operator.

$$Z = Tr\{e^{-\beta H}\}. \tag{1.10}$$

Here H is the Hamiltonian operator. The Boltzmann operator, i.e., the exponential in the partition function at finite inverse temperature β can be written using Taylor expansion as

$$e^{-\beta H} = \sum_{n=0}^{\infty} (-1)^n \frac{\beta^n}{n!} H^n. \tag{1.11}$$

The trace of the Boltzmann operator in Eq. 1.10 is the sum of the diagonal matrix elements in any basis $\{\theta_0\}$.

$$Z = \sum_{\theta_0} \left\langle \theta_0 \left| \sum_{n=0}^{\infty} (-1)^n \frac{\beta^n}{n!} H^n \right| \theta_0 \right\rangle \tag{1.12}$$

A complete set of states between each of the operator H of the n product is included and the partition function can be written as the sum over n states $\{\theta_i\}$ as

$$Z = \sum_{n=0}^{\infty} (-1)^n \frac{\beta^n}{n!} \sum_{\{\theta_i\}} \langle \theta_0 | H | \theta_1 \rangle \langle \theta_1 | H | \theta_2 \rangle ..... \langle \theta_{n-1} | H | \theta_n \rangle. \tag{1.13}$$

The partition function Z in the equation above is the sum of the matrix elements which is nonzero for $\theta_0 = \theta_n$.

The Hamiltonian H of the full system is a combination of diagonal and off-diagonal bond operators as shown below.

$$H = \sum_{d} \sum_{b} H_{d,b} \tag{1.14}$$

Here index d takes the value 1 or 2 that denotes diagonal and off-diagonal operators, respectively. b refers to different bonds in the system over which the operators act. Using Eq. 1.14, can express the partition function Z as

$$Z = \sum_{\{\theta_i\}} \sum_{n=0}^{\infty} \sum_{T_n} (-1)^n \frac{\beta^n}{n!} \prod_{i=1}^{n} \langle \theta_{i-1} | H_{d_i,b_i} | \theta_i \rangle. \tag{1.15}$$

Here T_n refers to the n diagonal and off-diagonal bond operators in the Hamiltonian with string of indices $\{d_i, b_i\}$ which requires to be sampled in QMC method.

The next step is to make the sampling of fixed size by restricting the Taylor series in Eq. 1.11 to a max-

imum power m. However, the truncation is reliable only if m is larger than the maximum n to occur. In order to satisfy this criteria, the powers with $n < m$ have to be increased by $m - n$ unit operators. The number of ways the $m - n$ unit operators can be located in the product of m operators in the expansion is $m!/(m-n)!n!$. Since these unit operators are absent in the partition function Z, in order to compensate their weights, the new partition function has to be divided by the number of those terms. The final expression of Z is

$$Z = \sum_{\{\theta_i\}} \sum_{T_m} (-1)^n \frac{\beta^n (m-n)!}{m!} \prod_{i=1}^{m} \langle \theta_{i-1} | H_{d_i,b_i} | \theta_i \rangle. \tag{1.16}$$

T_m is the modified string of m operators.

There are some efficient updating schemes are available to sample and update the basis configurations and operators. The local update method known for classical Monte Carlo to generate the Markov Chain are also used here for diagonal operators [63]. Some of the well known procedures for non-local updates are loop update [64, 65], cluster update [66]. Instead of discussing these methods, we would rather focus on the limitation of this method.

Although, the QMC works extremely well for various quantum many body systems, it fails to handle many systems (e.g., frustrated systems) because of the non-positive definiteness of the Taylor expansion in Eq. 1.13. It is obvious that the probability of a configuration to occur should always be positive. It can be noticed in the expression of the Z in Eq. 1.15 that the probability of a configuration to occur is related to the product of the matrix elements. All the matrix elements $\langle \theta_{i-1} | H | \theta_i \rangle$ takes the sign -1 in presence of FM interaction. It leads to cancellation of the minus sign and no sign problem occurs. However, in presence of AFM interactions, each individual matrix element has positive sign. In a AFM bipartite system, even n is needed in Eq. 1.15 to satisfy $\theta_0 = \theta_n$ and the Taylor expansion is positive definite. Also if a unitary transformation is carried out for the off-diagonal operators of one of the sublattice as $O_i \rightarrow -O_i$ (such as spin raising and lowering operators in HAF), the $(-1)^n$ in Eq. 1.13 and Eq. 1.15 gets cancelled which ensures positive definiteness. However, the frustrated systems suffer from sign problems as the Taylor expansion cannot get rid of the negative sign by a transformation.

1.3.2 Limitation of TMRG

DMRG is a numerical method for obtaining the gs properties of one-dimensional (1D) strongly correlated systems that characterize successfully quantum phases at temperature $T = 0$ [54, 67–69]. The efficiency of DMRG at $T = 0$ provides strong incentive for extension to finite T. TMRG was first introduced by T. Nishino [70] as a modification of the DMRG method [54] which is applicable to transfer matrix (TM). He applied this method to 2D classical system to calculate the partition function and other thermodynamic quantities at finite temperature (T). Soon after this development, a method was proposed to treat the 1D quantum systems in a similar way by mapping it to 2D classical system using Suzuki-Trotter decomposition of the partition function [71]. Since then TMRG has become one of the key tool that facilitates the study of thermal properties of 1D spin models [72] and fermionic models [15] with good accuracy.

In order to discuss this method briefly, let's consider a 1D HAF of spin-1/2 with periodic boundary condition (PBC) of N sites. The system Hamiltonian H can be expressed as the summation below.

$$H = \sum_{j=1}^{N} h_{j,j+1}. \tag{1.17}$$

The H is a combination of two parts H_o and H_e, each of them accounts for the interaction between only odd or even sites respectively.

$$\begin{aligned} H_o &= \sum_{odd\, j} h_{j,j+1}, \\ H_e &= \sum_{even\, j} h_{j,j+1}. \end{aligned} \tag{1.18}$$

As already noted, in order to map the 1D quantum system to 2D classical system, the Suzuki-Trotter decomposition of the partition function Z and it is represented as a trace of power of quantum transfer matrix T_M.

$$Z = Tr\left\{e^{-\beta H}\right\} = Tr\left\{\left[e^{-\varepsilon H_o} e^{-\varepsilon H_e}\right]^M\right\} = Tr\left\{T_M^{N/2}\right\}. \tag{1.19}$$

Here β is the inverse temperature. M is called the Trotter number. It is taken such that $\varepsilon = \beta/M$ is very small. T_M is asymmetric and can be written as the product of $2M$ local transfer matrix. If i_s is the spatial

coordinate and i_t is the coordinate in Trotter space, each of the local transfer matrix can be represented as

$$\tau\left(\sigma_{i_t}^{i_s+1}, \sigma_{i_t+1}^{i_s+1} | \sigma_{i_t}^{i_s}, \sigma_{i_t+1}^{i_s}\right) = \langle s_{i_t+1}^{i_s+1}, s_{i_t+1}^{i_s} | e^{-\varepsilon H_{o/e}} | s_{i_t}^{i_s}, s_{i_t}^{i_s+1} \rangle \tag{1.20}$$

Here $|s_{i_t}^{i_s}\rangle$ is the eigenstate of the operator $\hat{S}_{i_s}^{Z}$ and $\sigma_{i_t}^{i_s} = (-1)^{i_s+i_t} s_{i_t}^{i_s}$. These local transfer matrices can be represented as 2D plaquettes providing the classical 2D picture. Thus the T_M can be expressed as

$$\langle \sigma_1^3 ..... \sigma_{2M}^3 | T_M | \sigma_1^1 ..... \sigma_{2M}^1 \rangle = \sum_{\{\sigma_{i_t}\}^2} \prod_{i_t=1}^{M} \tau\left(\sigma_{2i_t-1}^3 \sigma_{2i_t}^3 | \sigma_{2i_t-1}^2 \sigma_{2i_t}^2\right) \times \tau\left(\sigma_{2i_t}^2 \sigma_{2i_t+1}^2 | \sigma_{2i_t}^1 \sigma_{2i_t+1}^2\right) \tag{1.21}$$

The total spin is conserved in T_M as $\sum_{i_t} \sigma_{i_t}^{i_s} = \sum_{i_t} \sigma_{i_t}^{i_s+1}$, which suggests that T_M is block diagonal for values of $\sum_{i_t} \sigma_{i_t}^{i_s}$. The thermal properties, correlations can be accessed at the thermodynamic limit from maximum eigenvalue λ and the left and right eigenvectors $|\varphi_L\rangle$ and $|\varphi_R\rangle$ of T_M, respectively. The two eigenvectors $|\varphi_L\rangle$ and $|\varphi_R\rangle$ of T_M appear because of the asymmetric nature of T_M. For example, the free energy F can be calculated using λ as

$$F = -\frac{1}{\beta} \ln \lambda. \tag{1.22}$$

The length $2M$ is increased keeping $\varepsilon = \beta/M$ fixed. The temperature is $T = 1/\varepsilon M$. λ, $|\varphi_L\rangle$ and $|\varphi_R\rangle$ can be derived from exact calculation for small M. When M is large, the concept of DMRG is used to accurately obtain λ, $|\varphi_L\rangle$ and $|\varphi_R\rangle$. The conventional DMRG algorithm will be discussed in detail in Chapter 2. The similar method applied here to transfer matrices which is not discussed here in detail. The key idea is that the M is increased using the truncated space of the density matrix which can be defined as

$$\rho = Tr_E |\varphi_R\rangle |\varphi_L\rangle. \tag{1.23}$$

Here the quantum transfer matrix is considered to have two parts, system block and environment block. E denotes the environmental degrees of freedom which is traced out. The main goal here is to perform iterative increase M using DMRG steps so that the thermodynamic quantities can be obtained at a lower $T = 1/\varepsilon M$.

Now let's discuss the limitations of TMRG method. One of the possible source of error is the finite ε [73, 74], but this error is very small in most of the cases. Also, since solving a non-symmetric matrix T_M

numerically is more difficult than a symmetric matrix, the density matrix might be compromised by the errors in $|\varphi_L\rangle$ and $|\varphi_R\rangle$ which can also facilitate the truncation error. The thermodynamic limit can be achieved with this method directly without requiring any extrapolation in system size. But different system sizes are required to access different T. The lower T is reached with progressively increasing system size (N) which increases the relative error in the calculation due to truncation in the Hilbert space using density matrix formalism [15]. Consequently, TMRG method fails to reach very low T without hampering the accuracy. The T accessible with TMRG with truncation error less than $< 10^{-3}$ or $< 10^{-4}$ is $T \sim 0.01 - 0.02$ [15, 74–77]. The results from TMRG become unreliable at lower T.

1.3.3 Finite T DMRG using enlarged Hilbert space

While TMRG is associated with the previously mentioned drawbacks, the conventional DMRG has already been proved to produce very accurate $T = 0$ properties. This is the main motivation behind generalizing the conventional DMRG for finite T. A. E. Feiguin and S. R. White [78] expanded the Hilbert space with auxiliary sites, named ancillas, and used a time-dependent DMRG method to study the thermal behavior of the 1D quantum many body spin systems. In this method, each real site is associated with an ancilla. The ancillas form a 1D chain which is parallel to the original chain. The full system consisting of real sites and ancillas is double of the original system of real site. It can be visualized as a quasi-1D ladder where each site is paired to its ancilla and form a supersite.

At infinite temperature (inverse temperature $\beta = 0$), the system is described by the maximally entangled state between the real and auxiliary systems. Let's consider that the set of states of the real system is $\{r_i\}$ and the set of states of the auxiliary system is $\{a_i\}$ where i denotes the position of sites along the leg of real sites and along the leg of auxiliary sites. The infinite temperature state can be expressed as

$$|\varphi(\beta = 0)\rangle = \prod_i \sum_{r_i} |r_i a_i\rangle. \tag{1.24}$$

Here $|\varphi(\beta = 0)\rangle$ is the maximally entangled state between real site and corresponding ancilla i denotes position or site index. Each state of the ancilla is assigned with quantum numbers opposite to the corresponding state of real site in order to conserve the quantum number. For example, the state of spin-1/2 system has total Z component of spin $S^Z = 0$. Each supersite has four basis states, i.e., $T_0 = (|\uparrow,\downarrow\rangle + |\downarrow,\uparrow\rangle)/\sqrt{2}$,

$T_1 = (|\uparrow,\downarrow\rangle - |\downarrow,\uparrow\rangle)/\sqrt{2}$, $T_2 = |\uparrow,\uparrow\rangle$ and $T_3 = |\downarrow,\downarrow\rangle$, where first and second spin in every ket representation denotes real site and ancilla, respectively. The infinite T state $\varphi(\beta = 0)$ is composed of the first triplet T_0 of all supersites. The rest of the three triplet basis has contribution at finite T.

The state at infinite T is evolved in imaginary time to reach finite T following DMRG steps. The Trotter time evolution method [79] and time-step targeted method [80] are used in this technique for the imaginary time evolution. At finite T, the state can be written as

$$|\varphi(\beta)\rangle = e^{-\beta H/2}|\varphi(0)\rangle. \tag{1.25}$$

The Hamiltonian H only acts on the real sites, not on ancillas. Ancillas evolve in imaginary time as they are entangled to the real site. The partition function Z can be written as

$$Z(\beta) = \langle\varphi|\varphi\rangle. \tag{1.26}$$

The expectation value of any operator A acting on the real system at a finite T is expressed as

$$\langle A\rangle = \frac{\langle\varphi|A|\varphi\rangle}{Z(\beta)}. \tag{1.27}$$

While forming the density matrix, ancillas in the system block are not traced out as H does not operate on ancillas. Whereas, ancillas in the environment block are traced out through their entanglement with the real sites in that block. Since A acts only on real sites, the expectation value in Eq. 1.27 traces out the auxiliary states.

At infinite T, only one state per block is required and the correlation between spins is suppressed by thermal fluctuation, i.e., the correlation length is zero. As T is decreased, thermal fluctuation becomes less dominant and correlation length increases. In consequence, the number of states required to keep for a desired accuracy increases. A. E. Feiguin and S. R. White calculated the specific heat and susceptibility using this method for a $S = 1$ Heisenberg chain of 64 spins and compared with the thermodynamic limit from TMRG method. Both the results agree with each other for $T \geq 0.05$ except at high T where slight deviation is observed due to the Trotter error. For spin-1/2 Heisenberg chain, the comparison of thermal properties of 64 spins with the thermodynamic limit from Bethe ansatz calculation also shows

good agreement for $T \geq 0.1$. However, the specific heat of spin-1/2 chain in presence of large frustration shows more prominent finite size effect and $N = 64$ gives the thermodynamic limit down to $T \sim 0.15$. Larger system size is required to access the thermodynamic limit at lower T.

1.4 Plan of the thesis

In this chapter we discussed a few relevant strongly correlated models and some real materials. We have also discussed the limitations of a few numerical methods for solving quantum many body systems at finite T. Accuracy of the TMRG method suffers at low T. The DMRG generalized with ancilla also has significant error at low T and also with long range exchange interaction. The QMC has sign problem in frustrated systems. Motivated by several limitations to access the finite T properties of 1D quantum models, we develop a hybrid approach to study the thermodynamics of quantum many body models. In this thesis, we have demonstrated the efficiency of this method in both spin chains [24, 81, 82] and fermionic systems [83]. Our aim is to establish this method as a general method to calculate the thermodynamic properties of quantum many body model model Hamiltonians. In this method, the high-T properties are calculated by the ED for small systems, whereas the DMRG is used to calculated the low-energy excitations of larger systems accurately, and extends the thermodynamics to lower T. Thus the properties in entire T regime can be calculated using the combination of the ED and the DMRG. However, the key aspect of this method is to utilize the low-laying spectrum rather the full spectrum of larger systems. The several aspects of this method will be discussed in detail in Chapter 3.

We will first concentrate on the efficiency of the hybrid method in calculating the thermodynamic properties of gapless and gapped 1D spin-1/2 systems at finite T. The availability of theoretical calculations of magnetic susceptibility, specific heat and per site energy of spin-1/2 HAF model provides a convenient bench marking tool for the hybrid ED/DMRG results. The spin-1/2 HAF model is a well studied model in literature with exact, field theoretical, and numerical results. We will start with comparing the solution for spin-1/2 HAF from this method with known results in Chapter 3. In order to benchmark this method, we show its efficiency to various system in Chapter 3. The method is also applied to model the spin-Peierls (SP) transition in 1D or quasi-1D AFM spin systems and the experimental observations of organic and inorganic SP systems are explained successfully using correlated states in Chapter 4. Chapter 5 presents its application to a long standing problem of the accurate calculations of thermodynamic properties of

half-filled and quarter-filled fermionic 1D models, and also analyse the accuracy of the results. We show that the hybrid ED/DMRG method is a general method for solving the 1D strongly correlated systems.

2
Numerical Methods

In the last Chapter 1 we have discussed various exotic phases in condensed matter systems and also tried to convince you that most of these phases can be understood using quantum many body models. We have also emphasized that the quantum many body interaction plays a vital role in understanding the condensed matter physics. However, solving a quantum many body Hamiltonian is a Herculean task because of exponential growth of the Hilbert space with the systems size for example for a spin-1/2 system of N sites goes as 2^N. For a spin-1/2 system there are two degrees of freedom (spin up or spin down) per site. Similarly, for a fermionic system where both spin and charge degrees of freedom are variable, each local site has four possible configurations, i.e., each site can be filled with either no electron, one up spin, one down spin or it can be doubly occupied. The total degrees of freedom for a system size N goes as 4^N and the Hilbert space dimension of finite system of fermionic models are discussed in detail in Chapter 5. Therefore, we are now convinced that we need to deal with large Hamiltonian matrix which grows exponentially with system size, and the numerical solutions become difficult for large system size.

The exact diagonalization (ED) numerical technique allows us to solve the many body models with small system size, i.e., with small Hilbert space dimension. The analytical solutions of most of the strongly interacting quantum many body models are either very difficult or nearly impossible. To overcome this limitation, several approximate numerical techniques have been developed, i.e., QMC [1], numerical renormalization (RG) [53], DMRG [54], tensor network [55] etc. In this thesis all the results shown in the next

chapters are mostly calculated using ED for small systems and DMRG for larger systems. In this chapter, we are going to discuss next the ED and conventional DMRG method.

2.1 Exact Diagonalization

The ED solution of a quantum many body model involves choosing a relevant local basis set with l degree of freedom per site and for system size N the dimension of Hilbert space is $m = l^N$. The basis set can be represented as $|\varphi_i\rangle$ where $i = 1, m$. The construction of the basis set is followed by formation of the Hamiltonian matrix for that system. If the Hamiltonian is H, then the matrix element H_{ij} is $\langle\varphi_i|H|\varphi_j\rangle$ and the dimension of the matrix is $m \times m$. i^{th} eigenvalue ε_i and eigenvectors $|\psi_i\rangle = \sum_i C_{i,j}|\varphi_j\rangle$ of the Hamiltonian matrix can be calculated by diagonalizing the matrix. Expectation value of operator O in i^{th} eigenstate can be calculated as $\langle\psi_i|O|\psi_i\rangle$ using the eigenvector. But application of this method is limited to only small systems due to exponential increase of Hilbert space dimension with system size.

In most of the quantum many body model systems the number of nonzero elements in the Hamiltonian matrix is small compared to the total dimension of the matrix, i.e., the matrix is highly sparse. The numerical cost for full diagonalization of a sparse matrix of dimension $m \times m$ is m^3, whereas cost of finding only low-lying energies of a sparse matrix goes as $m^{3/2}$. Main advantage of this numerical technique is the exact solution of the model Hamiltonian, but solution of these models are only restricted to small system size. In the most of quantum model systems with long range or quasi long range order can show large finite size effect and the ground state of finite systems size may not give realistic picture of the thermodynamic system and the finite size effect is expressed as finite size gap in spectrum. Therefore, a careful analysis is required to get the thermodynamic limit solution of spectrum.

Large dimension of the Hamiltonian matrix is one of the major problems in solving these models, and to reduce the dimension of the matrix we exploit various conserved quantities and symmetries of the model Hamiltonian. Symmetry operations have been proved to play an important role in reducing the computational cost of ED. If a symmetry operation leaves the Hamiltonian unchanged, then the operator commutes with the Hamiltonian. Using the symmetry operations, we can divide the Hamiltonian matrix into blocks of smaller sizes. Each block corresponds to some particular conserved quantum number. This requires a proper representation of the basis in which the symmetry operators are diagonal. Thus a symmetry operation takes the Hamiltonian to the block diagonal form, i.e., several blocks correspond to

different eigenvalues of the symmetry operators. A certain block associated with one of the eigenvalues of the symmetry operator can be selected to solve. The matrix elements of each block are independent of the other blocks, each block Hamiltonian can be diagonalized separately to get the eigenvalues and eigenvectors of the system. Thus the dimension of the matrix that we need to solve is largely reduced which in turn reduces the numerical effort. The reduced dimension enables ED to solve larger system sizes. There are some other benefit of applying symmetry operations to the Hamiltonian such as in some of the quantum many body systems have degenerate or closely spaced energy levels in the low-lying energy spectrum. As a result, the convergence of those energy levels are problematic leading to large errors. Most of the cases those degenerate or closely spaced energy levels belong to different symmetry sectors and applying the symmetry operation can separate these states into different symmetry spaces. Therefore, symmetry operations have been proved to be very effective in distributing those states to different symmetry blocks and help in getting rid of the large errors in energy convergence.

Let's consider a finite system of spin or fermionic model Hamiltonian H commutes with the z-component of the total spin S^Z.

$$[H, S^Z] = 0. \tag{2.1}$$

So the H and S^Z have the same set of eigenfunctions. The eigenvalues of H and S^Z (m_s) are good quantum numbers for the system. The Hamiltonian can be expressed in block diagonal form and each block corresponds to different S^Z sector or magnetization m_s. For a spin-1/2 system of N spins, m_s can take $N+1$ values as $0, (\pm 1, \pm 2, ..., \pm N/2)$, and thus the Hamiltonian matrix can have $N+1$ blocks. The Hilbert space dimension for blocks correspond to magnetization $m_s = 0, 1, 2, ..., N/2$ are ${}^NC_{N/2}$, ${}^NC_{N/2-1}$, ${}^NC_{N/2-2}$, ..., and 1 respectively. Thus each of this block has smaller matrix dimension than the full Hamiltonian matrix. All these smaller matrices can be diagonalized independently with significantly reduced numerical cost.

The edge effect is another problem in dealing with finite systems with open boundary condition, and it can be avoided by using periodic boundary condition (PBC). The PBC also helps in diminishing the effect of finite size scaling to some extent. Many symmetry operations, such as inversion symmetry, translational symmetry etc., can commute with the Hamiltonian only when the system is in PBC. The inversion symmetry operator rotates the system with an angle π about an axis passing through two opposite sites or mid

of the two opposite bonds at largest distance. The translational symmetry operator relocates each spin from its original site to the next site. The spin parity operator flips all the spin by π i.e all the down (up) spins are replaced by up (down) spins. The parity symmetry can only be spontaneously broken when total number of spin up and spin down in the system are equal. Unlike open boundary condition (OBC), the Hamiltonian under PBC stays uniform on applying these symmetry operators and they can transform the Hamiltonian into block diagonal form. The Hamiltonian H (the dimension of the full Hamiltonian matrix is $m \times m$) can be expressed in different symmetry sub-spaces by rotation of the Hilbert space using similarity transformation as, $H' = UHU^{\dagger}$ where U is the unitary transformation matrix related to the relevant symmetry operation with dimension $n \times m$, i.e., dimension of transformed Hamiltonian matrix H' is of order $n \times n$. Here, $n < m$. These symmetries are applied after the block diagonalization by S^Z so that they can further reduce the dimension of each block in a particular S^Z sector. Thus PBC empowers ED to solve larger system with small computational costs for diagonalizing each block.

Solving a many body model Hamiltonian using ED involves three steps. First step is associated with choosing a proper basis set and constructing the Hamiltonian matrix in that basis. The second step is to reduce the Hamiltonian matrix dimension into smaller independent blocks of smaller size associated with certain symmetry operations conserved in that system. The third step includes diagonalization of the matrix for the eigenvalues and eigenvectors and the calculation of the correlations and other observables relevant for the system. Even after incorporating various symmetry operations to reduce the matrix dimension, diagonalizing a Hamiltonian matrix for a moderate system size is still numerically expensive. As per our previous discussion, the numerical cost required for calculating all the eigenstates of a sparse matrix is m^3 when system has m dimensional Hilbert space. Focusing on only few low-lying states results in reduction of the cost to $m^3/2$. There are some efficient techniques exist in the literature that can solve the matrix eigenvalue problem up to few low-lying states accurately, such as Lanczos method [84, 85], Davidson algorithm [86–88]. The Davidson algorithm is first proposed by Ernest R. Davidson [86] for real symmetric matrix and later improved by Murray et al. [88]. Sten Rettrup in 1982 generalized the Davidson algorithm to solve the non-symmetric matrix [89]. In this thesis, for the purpose of calculating low energy states, we mainly use the Davidson algorithm for the symmetric matrix. We will provide a brief discussion about this algorithm below.

Let's start with a Hamiltonian H of a system with m dimensional Hilbert space, which has very small

number of non zero matrix elements, i.e., the Hamiltonian matrix is highly sparse. The eigenstates with lowest k eigenvalues of the Hamiltonian H can be expressed as

$$H\psi_l = \lambda_l \psi_l. \tag{2.2}$$

Here, $l = 1, ..., k$. The Hamiltonian matrix H is considered real and symmetric. The vectors ψ_l are the coefficients in series expansions of the wave functions in terms of the basis functions. The number of lowest eigenvalues k for a large matrix that can be obtained in this method is generally $k < 50$ [87].

A smaller subset of the vector space can be selected containing m dimensional orthonormal vectors $\{u_i\}$ with $i = 1, ..., n$. Here $n < m$. ψ_l can be expressed as a linear combination of n dimensional orthonormal vectors as

$$\psi_l = \sum_{i=1}^{n} a_l^{(n)}(i) u_i. \tag{2.3}$$

Let's assume a set of m dimensional orthonormal vectors w_l and consider the expansion of w_l in terms of the set of vectors $\{u_i\}$ as

$$w_l = \sum_{i=1}^{n} b_l^{(n)}(i) u_i. \tag{2.4}$$

The w_l considered here is an approximate guess of ψ_l. The goal here is to reach ψ_l from w_l iteratively. If the set of vectors $\{u_i\}$ are the columns of matrix U and the column vector consisting of the expansion coefficient $b_l^{(n)}(i)$ is B_l, then the matrix eigenvalue problem now reduced to

$$U^T H U B_l = \chi_l^n U^T U B_l. \tag{2.5}$$

Here, U^T is transpose of U and $l = 1, ..., n$. The eigenvalues follow

$$\psi_l \leq \chi_l^n, \tag{2.6}$$

where $l = 1, ..., n$. The eigenvalues are expected to gradually converge to the eigenvalues of the original problem with the increase of the size of basis. We consider a correction vector β_l to w_l which can be found

from

$$(H - \lambda_l I)w_l = a_k$$
$$(H - \lambda_l I)\beta_l = -a_k, \tag{2.7}$$

as the correction vector β_l follows $\beta_l = \psi_l - w_l$. I is the unit matrix of dimension m. In this method, the λ_l is substituted by $\eta_l = w_l^T H w_l / w_l^T w_l$ using the matrix H in the above expression as diagonalized matrix H_d. Thus the correction is obtained from $\beta_l \sim -(H_d - \eta_l I)^{-1} a_k$. The β_l is included with $\{u\}$ and then the process is iterated. The iteration is stopped when the eigenvalues are converged up to the desired accuracy.

In summary, ED gives very accurate results for finite systems of small number of sites. But in most of the cases, small system sizes are insufficient to extract the properties of the thermodynamic limit. To extrapolate the results to the thermodynamic limit, larger system sizes are crucial which can be calculated very accurately using the DMRG technique. The next part of this Chapter is devoted to the discussion of DMRG method.

2.2 Density Matrix Renormalization Group

Steven R. White introduced the density matrix renormalization group (DMRG) in 1992 and applied it to the ground state of quantum spin chains [54, 67]. DMRG has become a powerful general method for the ground state and low energy excitation gaps that characterize the quantum ($T = 0$) phases of one-dimensional (1D) models with spin or charge degrees of freedom [68, 69] and thus it opened as new door for understanding quantum many body condensed matter systems. It is a state of the art iterative numerical technique and each iteration involves the growth of the system in small steps which is followed by systematic truncation of irrelevant degrees of freedom in the Hilbert space [54, 90], i.e. keeping the most probable states.

Since the development of DMRG algorithm, it has been applied to solve several 1D quantum many body models, such as spin-1/2 and spin-1 Heisenberg model [52, 54, 67, 91–94], frustrated J_1–J_2 model [21, 23, 95, 96], fermionic models [97–101], Bose-Hubbard models [102, 103] and also 2D systems [104] and the method is successful in predicting the ground state and, correlations and exotic phases at temperature $T = 0$ with remarkable accuracy. The conventional DMRG method is further improved for zigzag

chains [105], Bethe lattice [106]. Although DMRG was known to be efficient for the systems with open boundary condition in early stages, the conventional DMRG algorithm has been modified recently to apply it successfully to the systems with periodic boundary condition (PBC) [107].

2.2.1 Numerical RG and Motivation behind DMRG

The concept of DMRG was developed in the context regarding the problem of applying RG [53] to 1D lattice [54]. The RG [53] was developed by K. G. Wilson to solve the Kondo problem. The method is not appropriate for strongly correlated system since the chosen state for each block creates problem at the boundary of the block since each block is completely separated from the other blocks. The idea behind getting rid of this problem, i.e., the blocks need to be embedded in some environment mimicking the complete system so that the retained states for the block are the projections from the states of the whole system and environment (i.e., superblock), became the key ingredient of the DMRG method. The DMRG is different from RG in a way that the system blocks are not completely excluded from the rest of the system. Before discussing the DMRG method in detail, let's first briefly mention the concept of RG method.

In order to state the RG procedure for 1D system, let's consider a block X and another block Y, both of length L with a m dimensional Hilbert space. The next step is to construct the Hamiltonian of the superblock H_{XY} which consists of the Hamiltonian of block X, Y and the interaction between X and Y. The basis of the superblock is the product state of the basis from each block. The length of the superblock is $2L$ and the Hilbert space dimension is m^2. From the diagonalization of H_{XY}, m eigenstates with lowest eigenvalues can be found. The next step is to truncate the m^2 dimensional Hilbert space to m dimension. m^2 basis sets of H_{XY} is changed to the truncated basis set by projecting H_{XY} on the m dimensional Hilbert space using $H'_{XY} = OH_{XY}O^\dagger$. The transformation matrix O is $m \times m^2$ dimensional matrix and dimension of the transformed Hamiltonian matrix H'_{XY} is now reduced to $m \times m$. Now one iteration of RG method is completed and next iteration starts by considering H'_{XY} as new system block of length $2L$ with m dimensional Hilbert space. Next, the process goes on by doubling the system size as mentioned earlier and truncating the Hilbert space size until the aimed system size is reached.

The idea behind the method lies on the concept that the ground state of the superblock can consist of low energy states of smaller subblocks. Since the blocks are completely disconnected from each other, the

selected states of the renormalized block H'_{XY} from the states of the subblock create significant error at the boundary of the block which is the main source of problem in this method [54, 90]. Let's assume the lowest eigenstate of neighboring blocks X and Y have nodes at the boundary of each of the blocks and maxima at the mid of the blocks. The product state of X and Y also should have nodes at the boundary of X or Y. But the common boundary of them is the mid of the superblock XY where a maximum should occur. Due to this discrepancy at the boundary, the concept of RG is not appropriate for strongly correlated systems and produces inaccurate results.

S. R. White et. al. [108] approached this problem by considering several fixed and free boundary conditions for particle in a box. Combining different boundary conditions, the authors showed the choice of appropriate state to keep for the block. This method improves the results for single particle models, whereas the desired accuracy of interacting systems was still out of reach. S. R. White encountered this problem [54] by bringing the idea of density matrix into the conventional RG procedure. To minimize the error at the boundary, he strategically formed the density matrix for the system block and project the Hilbert space in the truncated space of the density matrix so that block stayed embedded in an environment rather than being completely isolated. This method gained striking success in improving the accuracy of the low dimensional interacting quantum models.

2.2.2 Density Matrix Formulation

The algorithm of DMRG is based on iterative growth of the system along with systematic truncation of irrelevant degrees of freedom at every iteration. To solve many body models, infinite and then finite DMRG procedure are performed sequentially. In the infinite DMRG, the system is grown and the Hilbert space is truncated in an iterative fashion until the desired system size is achieved. The infinite DMRG is followed by the finite algorithm where system block and environment block are alternatively increased (decreased) and decreased (increased) keeping the total length of the system fixed in order to improve the accuracy and to achieve the optimised wave function. In RG algorithm, the system size is increased exponentially fast, i.e., the block doubles at each step. Whereas, the block size grows linearly in DMRG, thus the growth is slower compared to RG method. This is a small price to pay for its excellent accuracy.

Before explaining the infinite and finite DMRG algorithm, let's first briefly discuss the concept of the density matrix in DMRG. Let's consider a system block A of length L with a m dimensional Hilbert space.

The environment block B mimics the system block and thus has same length and same Hilbert space dimension. Considering the linear growth of blocks of $N = 1$ or 2 site (new site block), the N new sites will be added to both system and environment block. The superblock consists of old system block with the new site block and their reflections, i.e., environment block with new site block, therefore, total length of the superblock will be $2L + 2N$. Considering $\{|a_i\rangle\}$ is a basis set of block A, $\{|b_i\rangle\}$ is a basis set of environment block B, both with Hilbert space dimension m and $\{|\sigma_i\rangle\}$ is a basis set of new site block with N local new sites with Hilbert space dimension m_σ, the basis set of the new system block (new environment block) formed with old block A (B) and new site block is the product state $\{|a'_j\rangle\} \equiv \{|a_i\rangle|\sigma_i\rangle\}$ ($\{|b'_j\rangle\} \equiv \{|b_i\rangle|\sigma_i\rangle\}$) with Hilbert space dimension $m_s = mm_\sigma$. The superblock dimension is (o)$m^2m_\sigma^2$ and diagonalization of the superblock Hamiltonian matrix gives the target state (generally a ground state $|\psi\rangle$) whose accuracy is the aim of this method. $|\psi\rangle$ can be expressed as

$$|\psi\rangle = \sum_{ij} c_{ij}|a'_i\rangle|b'_j\rangle. \tag{2.8}$$

Before adding the new site block to grow the block size again, truncation of the Hilbert space of the new system and environment block is necessary. The blocks are represented in the eigenspace of the density matrix to avoid the effect of the disconnected blocks from the lattice in RG method. The truncation is done in the diagonal vector space of the density matrix of the block.

The density matrix ρ of the system block can be found from the state of the superblock $|\psi\rangle$ by tracing out the environmental degrees of freedom.

$$\rho = Tr_E|\psi\rangle\langle\psi| = \sum_{ii'j} c_{ij}c^*_{i'j}|a'_i\rangle\langle a'_{i'}|. \tag{2.9}$$

Here E refers the environmental degrees of freedom. The expectation value of any operator Z of system block can be written using the density matrix.

$$\begin{aligned}\langle\psi|Z|\psi\rangle &= \sum_{ii'j} c^*_{ij}c_{i'j}\langle a'_i|Z|a'_{i'}\rangle \\ &= \sum_{ii'} \langle a'_{i'}|\rho|a'_i\rangle\langle a'_i|Z|a'_{i'}\rangle\end{aligned}$$

$$
\begin{aligned}
&= \sum_i \langle a'_{i'} | \rho Z | a'_{i'} \rangle \\
&= Tr\rho Z. \qquad (2.10)
\end{aligned}
$$

The density matrix ρ can be diagonalized to have m_s eigenstates $|\alpha_i\rangle$ with real and positive eigenvalues α_i.

$$\rho = \sum_{i=1}^{m_s} \alpha_i |\alpha_i\rangle\langle\alpha_i|, \qquad (2.11)$$

where $\sum_{i=1}^{m_s} \alpha_i = 1$. The expectation value in Eq. 2.10 can be written as a summation of all m_s eigenstates of ρ.

$$\langle\psi|Z|\psi\rangle = Tr\rho Z = \sum_{i=1}^{m_s} \alpha_i \langle\alpha_i|Z|\alpha_i\rangle. \qquad (2.12)$$

If we keep n_s most probable eigenvectors with largest eigenvalues out of total m_s eigenvectors, then the truncated expectation value can be expressed as a sum over only those n_s states as

$$\langle\psi|Z|\psi\rangle_{trunc} = \sum_{i=1}^{n_s} \alpha_i \langle\alpha_i|Z|\alpha_i\rangle. \qquad (2.13)$$

The error for this approximation is $\sum_{i=n_s+1}^{m_s} \alpha_i \langle\alpha_i|Z|\alpha_i\rangle$. This error is minimum when the eigenvalues of the density matrix decay exponentially fast such that the neglected states in Eq. 2.13 have negligible contribution to the expectation value $\langle\psi|Z|\psi\rangle$ in Eq. 2.10. This truncation is done after each step of the systematic growth of the system block.

2.2.3 Infinite DMRG Algorithm

Let's consider a 1D system with open boundary condition (OBC). The steps of the infinite DMRG algorithm are systematically discussed below.

1. The method starts with a small system of four sites that consists of left block (system block) A, right block (environment block) B and two new site blocks (left new block and right new block), each of them containing one site. The total system is called superblock. The initial step (a) in Fig. 2.1 depicts the initial superblock of four sites by the squares made of black dashed line and the initial system block and environment block are shown by the squares made of solid blue line at the left and the right end of the 1D chain. The left new and right new blocks are shown by the red cross.

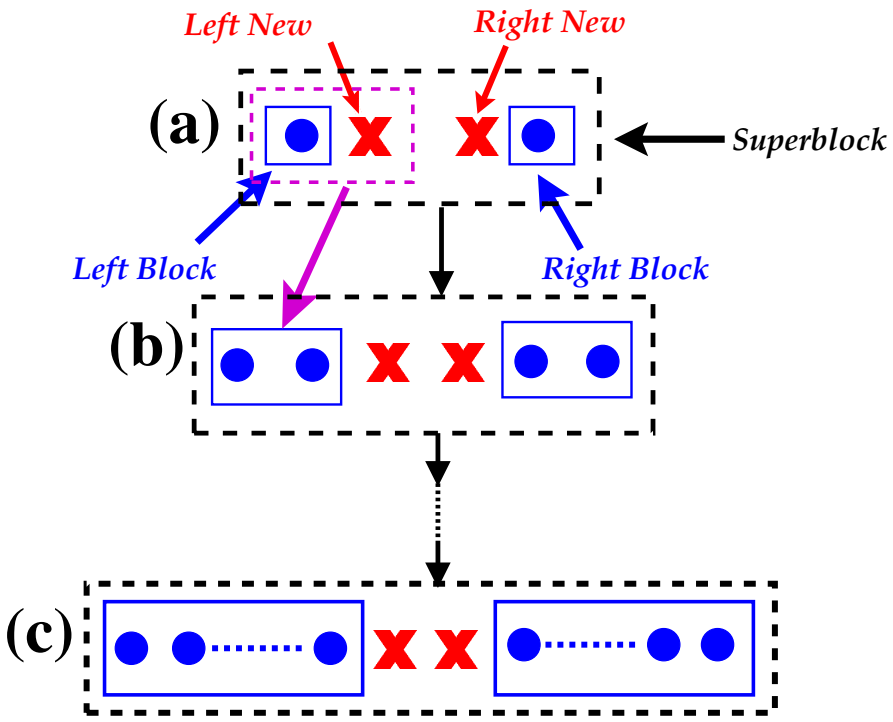

Figure 2.1: Infinite DMRG steps. It starts with superblock of four sites as shown in (a). The renormalized system (left or right) block of one site are shown inside the square in solid blue line and the magenta square made of dashed line containing left block and new site represents the new left block for the next step (b) as shown by the magenta arrow. At each step, the superblock size grows. In (c) the targeted system size is shown.

2. The Hamiltonian of the superblock is formed using the block Hamiltonians and the interblock interactions. The superblock matrix is diagonalized to get the target state $|\psi\rangle$.

3. The new left block A′ for the next step can be formed from left block A and the left new block of one site. As discussed in the previous subsection, A′ has $m_s = mm_\sigma$ dimensional Hilbert space, where m_σ is the Hilbert space size of new site block. The new right block B' is constructed the same way as A′. This is shown in (a) of Fig. 2.1.

4. The density matrix ρ of the system block is calculated from the target states of the superblock using Eq. 2.9. The diagonalization of the density matrix gives m_s eigenstates. We keep n_s ($\leq m_s$) dominant eigenstates with largest eigenvalues and discard the other eigenstates. We project the system block space and other operators to the truncated space of the density matrix using a transformation matrix O as $G' = OGO^\dagger$. The rows of O are the eigenvectors of the density matrix and there are n_s rows that correspond to the n_s eigenvectors with largest eigenvalues. Thus the dimension of O is $n_s \times m_s$. G can be the Hamiltonian matrix $H(m_s \times m_s)$ for the blocks A′ or B′ or operators acting

on the blocks. H' is the renormalized matrix with a truncated dimension $n_s \times n_s$.

5. Next we consider A′ and B′ with the renormalized Hamiltonian matrix as the left and right block respectively (A≡ A′ and B≡ B′) as shown in (b) in Fig. 2.1 by the square made of solid blue line. The new superblock is depicted by the black dashed line. Then we go back to the 2nd step. We repeat the iteration until the targeted system size is reached.

The infinite DMRG algorithm, where both the left and right block grow, is performed up to some desired superblock length. In some cases, this algorithm does not yield accurate results since the blocks at the intermediate steps are not embedded in the total system of targeted system size. The goal of the finite DMRG algorithm is to optimize the wave function by zipping the left and right block back and forth while keeping the total length of the superblock constant.

2.2.4 Finite DMRG Algorithm

At the end of the infinite DMRG, superblock achieves a length $2L + 2$ and the left and right blocks are of equal size L. In the finite DMRG method, the total superblock length remains fixed at $2L + 2$. Instead of growing both the left and right block, one of the block grows at the cost of other block, i.e., the other block shrinks. The projection to the truncated space of the density matrix is carried out for the increasing block. The Hamiltonian matrix or the operators for the shrinking block were stored during the infinite DMRG iterations or previous steps of finite DMRG algorithm which are reused in the finite DMRG. In this procedure, both the left and right block are embedded in the total system of desired length which is required to overcome the errors appeared in case of RG technique. Let's focus on different steps of the finite DMRG procedure.

1. The finite DMRG starts with the growth of one of the block, let's say the left block and shrinkage of the right block without changing the total length of the superblock $2L + 2$. This is depicted in (a)-(c) in Fig. 2.2.

2. One of block, let's consider the left block, is allowed to increase in size by adding one new site at each step. The size of the right block is decreased by reducing one site. The superblock is formed in each step with left block, right block and two new site block as shown in Fig. 2.2. The diagonalization of the superblock matrix gives the target state $|\psi\rangle$.

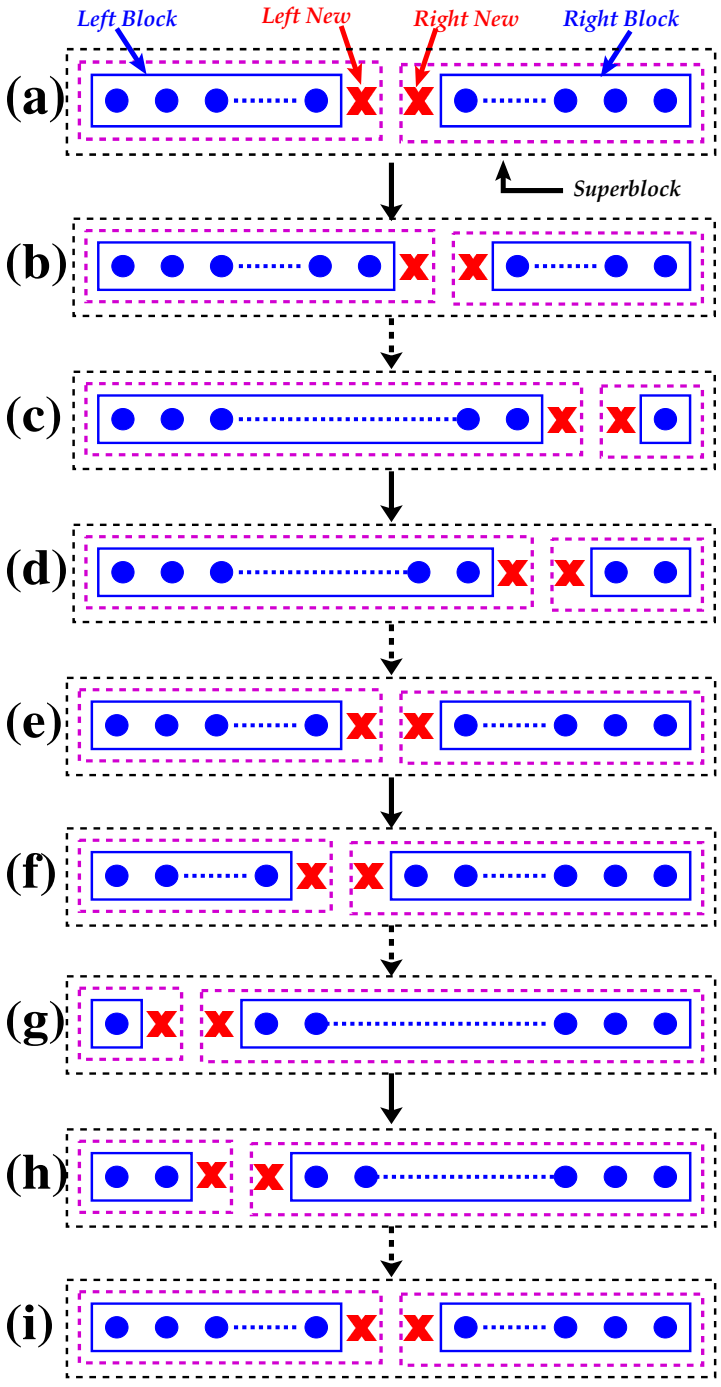

Figure 2.2: Finite DMRG steps. It starts with left and right block of equal size and two new site block of N sites as shown in (a). Here, $N = 1$ is considered. The renormalized system block is shown inside the blue square made of solid line whereas the magenta square with dotted line represents the new left block for the next step (b). The left/right block increases/decreases back and forth. At the end of the sweep, left and right block are of equal size again as shown in (i). Several steps of a finite dmrg sweeps are shown in (a) - (i).

3. The density matrix ρ is found from $|\psi\rangle$ using Eq. 2.9. We diagonalize the density matrix and keep the most probable eigenstates with largest eigenvalues. Similar to the infinite DMRG, the left block and operators are renormalized with the truncated set of density matrix eigenstates. The right block Hamiltonian and operators are found from saved data built during infinite DMRG procedure.

4. Let's consider that the minimum length each block can have is N. By repeating the process, the left block is allowed to increase in size until it achieves the maximum length $2L - N$ and the right block acquired the minimum length N. This way we eventually reach an open end of the system as shown in (c)in Fig. 2.2.

5. Once, the right block size is N, the growth and reduction is reversed for the left and right block, i.e., right block grows at the expense of the left block by adding N sites at each step. This can be observed in (d)-(g) in Fig. 2.2.

6. When the right block size becomes the largest (size $2L - N$) and left block becomes the shortest (size N) ((g) in Fig. 2.2.), the direction of growth is reversed one more time, i.e., again the left block grows at the cost of the right block as shown in (h) in Fig. 2.2.

7. The process is now continued until the left and right blocks achieve equal size L again ((i)in Fig. 2.2.). This completes one sweep of the finite DMRG. The sweeps are repeated until accuracy up to a desired precision is reached.

2.2.5 DMRG Algorithm for PBC

Although the accuracy of conventional DMRG applied to OBC is excellent, acquiring good accuracy with PBC is strongly desired in quantum many body problems. The reason lies in the fact that the system with OBC has strong finite size effect at the edge, which can be reduced by applying the PBC. Also, unlike OBC, various symmetry operators commute with the Hamiltonian of the system if PBC is applied to the system and in turn the Hamiltonian matrix can be expressed in block diagonal form as discussed in Section 2.1. Thus it is possible to work with smaller matrix size which reduces the numerical effort.

If the conventional DMRG method for the 1D system with OBC needs n_s most probable eigenvectors of the density matrix to form the truncated space to achieve accuracy with required precision, the same

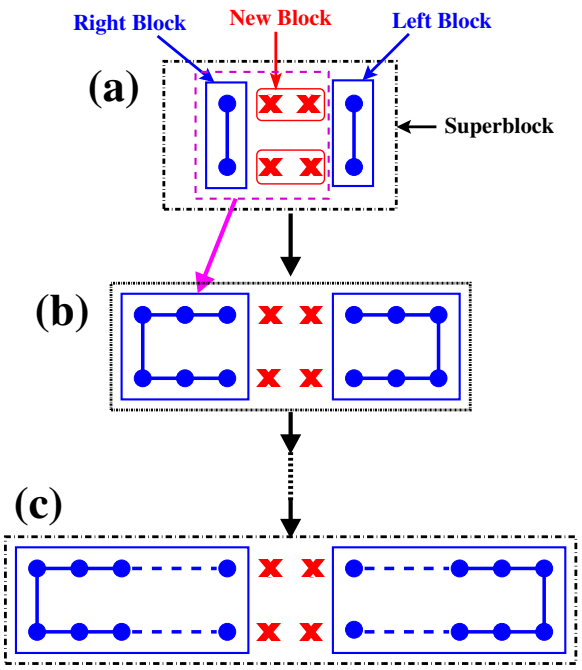

Figure 2.3: DMRG steps for PBC. At every step, two new block of $N = 2$ sites are added as shown in (a). The renormalized left and right block are shown inside the squares in solid blue line. The red squares of solid line are new site block. The magenta square of dashed line is the new left block composed of old left block and two new blocks. The new right block is the reflection of new left block. They are the left and right block of next step (b) as shown by the magenta arrow. The black squares of solid line represents the superblock at every step. In (c) the targeted system size is shown.

with PBC needs $O(n_s^2)$ [55]. As a result, the computational cost for sparse matrix diagonalization in case of OBC is $O(n_s^3)$, while, for the periodic boundary condition (PBC), the cost goes as $O(n_s^6)$ [109]. This is one of the reason behind the large error in the conventional DMRG with PBC.

Also, we cannot overlook that 1D system with PBC connects the left and right ends with a long bond. The error in the operators that give off-diagonal elements (spin raising and lowering operators in spin models and annihilation and creation operators in fermionic models) increases with higher number of renormalization. The interaction between long distant sites compromises the sparsity of the matrix and the numerical cost of the dense matrix diagonalization is high ($O(n_s^4)$).

For efficient application of DMRG to the system with PBC, we apply a modified DMRG algorithm [107] that steers clear of the renormalization of operators multiple times and provides results without compromising the accuracy. The algorithm is discussed below.

1. The algorithm starts with a superblock of small size, i.e., one left block, one right block and two new site blocks as shown in (a) of Fig. 2.3.

2. The target state $|\psi\rangle$ is achieved from diagonalization of the superblock. The new system (environment) block is the combination of left (right) block and two new site block. The density matrix ρ of the new system block is found from Eq. 2.9.

3. The block Hamiltonian and operators are projected to the truncated basis formed by the n_s dominant states of ρ with largest eigenvalues.

4. Next, the two new site blocks are added again to the renormalized system and environment block as shown in (b) of Fig. 2.3 and the superblock Hamiltonian is formed. Then the process is repeated again from second step until the required superblock size is obtained.

Thus it is clear that the strategy of adding new site block in this modified algorithm avoids the long bond that occurs in the conventional DMRG method with PBC. The blocks and operators in this method are renormalized once which diminish the error in the calculation.

As it is already stated in Chapter 1 that we have recently developed hybrid ED/DMRG method for finite T properties of quantum many body models, its application to spin models along with its efficiency and accuracy will be discussed in Chapter 3.

3

Hybrid Exact Diagonalization and Density Matrix Renormalization Group Approach to the Thermodynamics of 1D Spin Models

3.1 Introduction

We discuss in this Chapter [1] the development of the hybrid approach and its efficiency to the thermodynamics of spin chains and quantum cell models. The high-T regime is treated conventionally by exact diagonalization (ED) of small systems. DMRG then gives the low-energy excitations of increasingly large systems. Partition functions based on a few thousand states yield the low-T thermodynamics. The combination of ED and DMRG covers the entire range, down to T set by the accuracy of DMRG excitations, without ever invoking the full spectrum of large systems. The hybrid ED/DMRG approach is general, with DMRG tuned to the low-energy spectrum instead of the ground state.

There are broadly two contexts, mathematical and physical, for discussing spin chains or 1D quantum cell models. The spin-1/2 linear HAF is the oldest and best characterized many-spin system [110–112]. The spin-1 HAF or other spin-1/2 models have been intensively studied for decades using field theory [113, 114] and numerical methods [1]. Correlated many-spin or many-electron models are intrin-

[1] The work reported here is based on "*Hybrid exact diagonalization and density matrix renormalization group approach to the thermodynamics of one-dimensional quantum models*", Sudip Kumar Saha, Dayasindhu Dey, Manoranjan Kumar, and Zoltán G. Soos, Phys. Rev. B, vol. 99, p. 195144, May 2019.

sically interesting. The characterization of quasi-1D compounds with linear chains of transition metal ions or organic radical ions has an equally long history [33, 115]. Isotropic exchange is the dominant interaction, but not the only one. Thermodynamics to a factor of two or three lower T than possible by ED would significantly aid the analysis of magnetic data. The $T \to 0$ limit is interesting mathematically. The spin-1/2 $J_1 - J_2$ model, Eq. 1.7, illustrates both contexts.

The $J_1 - J_2$ model with $J_1 < 0$ in Eq. 1.7 is the starting point for the magnetic properties of cupric oxides that contain chains of spin-1/2 Cu(II) ions and have singlet ground states [22, 116–120]. An applied magnetic field of 10 Tesla is sufficient to induce the FM ground state in some cases. The T and field dependencies of the magnetization and magnetic specific heat can be followed in systems with competing FM and AFM interactions. Present estimates of J_1 and J_2 in specific materials are rather approximate. At issue are the low-T thermodynamics of the model, corrections due to spin-orbit coupling and additional (dipolar, hyperfine, interchain) weak interactions. We discuss the zero-field thermodynamics and focus on the magnetic susceptibility and specific heat.

The hybrid ED/DMRG approach is applicable to quantum cell models with a large but finite basis that increases exponentially with system size. There are $(2S+1)^N$ states in a system of N spins-S, and similar expressions hold for models with charge as well as spin degrees of freedom. Here we consider N spins-1/2 in models indexed by α. The energy spectrum $\{E(\alpha, N)\}$ has 2^N states for any α. The thermodynamics is governed by the canonical partitions function

$$Q(T, \alpha, N) = \sum_j \exp\left(-\beta E_j(\alpha, N)\right), \tag{3.1}$$

where T is the absolute temperature, $\beta = 1/k_B T$, k_B is the Boltzmann constant, the sum is over all states, and $E_j(\alpha, N)$ is relative to the ground state energy. The per spin result of the infinite chain is

$$N^{-1} \ln Q(T, \alpha, N) \to \ln Q(T, \alpha). \tag{3.2}$$

The problem is to obtain or approximate the thermodynamic limit.

Our basic premise is that the full spectrum $\{E(\alpha, N)\}$ of large systems is never needed. The most demanding cases are gapless chains with quasi-long-range order in the ground state or chains with exponentially small gaps. Even then, thermal fluctuations suppress correlations between distant spins and the

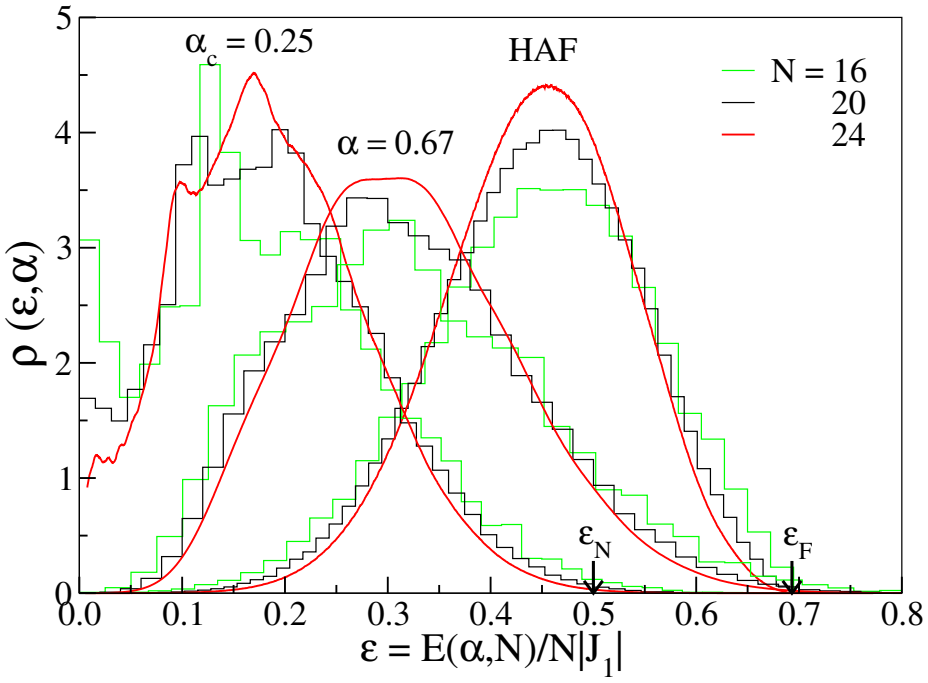

Figure 3.1: Normalized density of excitations, $\rho(\varepsilon, \alpha)$ with $\varepsilon = E(\alpha, N)/N|J_1|$, for three models of N spins. The ground state is a singlet $(S = 0)$ at $\varepsilon = 0$. The Néel state $(\ldots \alpha\beta\alpha\beta \ldots)$ has excitation energy $\varepsilon_N = 1/2$ for the α_c model while the FM state $(\ldots \alpha\alpha\alpha\alpha \ldots)$ has $\varepsilon_F = \ln 2$ for the HAF.

system size becomes irrelevant when N is several times the correlation length. ED yields the full spectrum $\{E(\alpha, N)\}$ up to N, here to $N = 24$ for spin-1/2 chains. We can always find $T_n(\alpha, N)$ such that the thermodynamic limit is satisfied at $T > T_n(\alpha, 24)$ for the quantity of interest. The low energy part of $\{E(\alpha, N)\}$ for larger N is required at lower T, and DMRG is well suited for low-energy excitations. In principle, the problems are to obtain the low-energy excitations and to combine them with ED results.

The same conclusion follows from the increasing density of states with system size and the passage from a sum in $Q(T, \alpha, N)$ to an integral over excitations. The Boltzmann factor varies smoothly at high T but is strongly peaked at low T. We expect and find lower $T_n(\alpha, N)$ in models with a high density of low-energy excitations. The normalized density of excitations, $\rho(\varepsilon, \alpha)$ with $\varepsilon = E(\alpha, N)/N|J_1|$, is shown in Fig. 3.1 for $N = 16$, 20 and 24 spins in the HAF and $J_1 - J_2$ models with $J_1 < 0$ and $\alpha = J_2/|J_1|$. We obtained $\rho(\varepsilon, \alpha)$ for $N = 16$ and 20 as the number of states in $40 - 50$ bins of equal width. We took narrower bins for $N = 24$ and averaged over several adjacent bins to get relatively smooth curves.

A triplet at $E_T(\alpha, N)$ is typically the lowest excitation of spin chains with a singlet ground state. The size dependence of $E_T(\alpha, N)$ has been extensively discussed for the HAF and half-filled Hubbard or extended Hubbard models. The spin chains we consider have frustrated exchange interactions that shift the density

of excitations to lower energy in Fig. 3.1. We shall be comparing systems with similar finite-size gaps but different thermodynamics that reflects the excitation spectrum $\rho(\varepsilon, \alpha)$.

The chapter is organized as follows. Section 3.2 presents the hybrid ED/DMRG procedure, starting with the DMRG calculation of excitation energies, moving on to truncation and ending with comparison with HAF thermodynamics. We turn in Section 3.3 to the $J_1 - J_2$ model with FM exchange $J_1 < 0$ and AF exchange $J_2 > 0$. We compare results on the $J_1 < 0$ side with field theory and TMRG. ED to $N = 24$ accounts well for the spin susceptibility $\chi(T)$ and specific heat $C(T)$ per site at the critical point, $\alpha_c = 1/4$. DMRG extends the thermodynamics of FM/AFM chains to $T \sim 0.01$ in units of $|J_1|$, the largest exchange. Section 3.4 is a brief discussion of the method and its scope.

3.2 Thermodynamics, Truncation and Extrapolation

We develop in this Section the thermodynamics of spin chains without invoking the full energy spectrum $\{E(\alpha, N)\}$. In 3.2.1 we obtain the low-energy states $E_j(\alpha, N)$ of models α with N spins. In 3.2.2 we truncate the partition function $Q(T, \alpha, N)$ in Eq. 3.1 at $E_j(\alpha, N) \leq W_C(\alpha, N)$ and discuss the choice of the energy cutoff. Extrapolation to the thermodynamic limit is demonstrated in 3.2.3 against exact HAF results. The applications in Section 3.3 are to $J_1 - J_2$ models for which numerical analysis is more difficult and exact results are limited to $T = 0$.

The frustrated $J_1 - J_2$ model with isotropic exchange J_1, J_2 is already discussed in Eq. 1.7. We consider the ratio of the exchange interactions as α ($J_2 = \alpha |J_1|$). We also consider $J_1 < 0$ and set $|J_1| = 1$ as the unit of energy. in chains of $N = 4n$ spins-1/2 with periodic boundary conditions. The model Hamiltonian in Eq. 1.7 can be rewritten as

$$H(\alpha) = -\sum_r \vec{S}_r \cdot \vec{S}_{r+1} + \alpha \sum_r \vec{S}_r \cdot \vec{S}_{r+2}. \tag{3.3}$$

The ground state of this model is a singlet, total $S = 0$, for $\alpha > \alpha_c = 1/4$. The singlet and FM states are degenerate at the exact quantum critical point α_c [28]. The degeneracy at α_c is also exact for finite $N = 4n$ [121]. The HAF has AF exchange $J_1 = 1$ and $\alpha = 0$ in Eq. 3.3. Exact, field theoretical and numerical results for its thermodynamics in zero field are summarized in detail in Ref. 112. Although there are open questions, especially in finite field, nowadays the HAF provides convenient tests of numerical methods.

3.2.1 DMRG

We use the efficient DMRG algorithm for periodic boundary conditions in Ref. 107, where it was applied to the ground state energy and lowest excitation of HAFs with spin-1/2 and 1. The superblock in this method has two new sites in addition to the left and right blocks. Since Eq. 3.3 has second neighbor interactions, we take new blocks of two sites in order to avoid interaction terms between old blocks. Four sites are added in each block at every step of infinite DMRG. The accuracy and computational costs are similar to matrix product state calculations [107].

Infinite DMRG is used to generate the desired system of $N = 4n$ spins. Some 5-10 sweeps of finite DMRG are then performed. In most calculations we kept $m = 400$ eigenvectors that correspond to highest eigenvalues of the system block density matrix. The superblock Hamiltonian has dimension $m^2 2^4$. The ground state $E_1(N)$ is taken as zero. The states $j > 1$ have excitation energies $E_j(N) > 0$. The DMRG partition function with l states of the superblock Hamiltonian is

$$Q_l(T, N) = \sum_{j=1}^{l} \exp\left(-\beta E_j(N)\right). \tag{3.4}$$

We later consider truncated partition functions $Q_C(T, N)$ with $E_j(N) \leq W_C(N)$ at energy cutoff $W_C(N)$.

We introduce in this chapter several modifications that are tailored for finite systems. The focus is on excitations rather than the ground state. To improve the accuracy of the spectrum, we construct the system block density matrices $\rho_j(N)$ for the l levels at system size N and define an effective density matrix $\rho'(\beta', l)$

$$\rho'(\beta', l, N) = \sum_{j=1}^{l} \rho_j(N) \exp\left(-\beta' E_j(N)\right) / Q_l(T, N). \tag{3.5}$$

The $l = 1$ case is simply $\rho'(\beta', 1) = \rho_1$ when the ground state is sought. Contributions for $l > 1$ are governed by β', an effective inverse T. We set $\beta' = 10$ (in units of $1/|J_1|$) since $T \sim 0.1$ is the range of interest. Variations of β' by 10 to 20% hardly change the accuracy of the spectrum. The effective density matrix becomes important when the lowest excitations are closely spaced. The system block Hamiltonian and all operators are renormalized by $\rho'(\beta', l, N)$ to obtain the energy spectrum the model Hamiltonian at system size N. We perform two calculations. We first take $l = 5$ or 10 in order to obtain the lowest

Table 3.1: Exact (ED) and DMRG excitations in units of $|J_1|$ of chains with $N = 24$ and 32 at $\alpha = 2/3$ in Eq. 3.3. The ground state is at zero energy.

$\alpha = 2/3$	$N = 24$		$N = 32$	
Level no.	E (ED)	E (DMRG)	E (ED)	E (DMRG)
2	0.1936	0.1936	0.1273	0.1283
3	0.1936	0.1936	0.1397	0.1403
4	0.2168	0.2169	0.1397	0.1405
5	0.2299	0.2301	0.1541	0.1553
6	0.2417	0.2418	0.1643	0.1659
7	0.2701	0.2703	0.1866	0.1879
8	0.2701	0.2703	0.1866	0.1883
9	0.2817	0.2818	0.1883	0.1903
10	0.2817	0.2821	0.1883	0.1907

Table 3.2: Exact (ED) and DMRG excitation energies for $N = 24$ and 32 at $\alpha = 1/2$ in Eq. 3.3. The starred excitation is the lowest singlet, $S = 0$.

$\alpha = 1/2$	$N = 24$		$N = 32$	
Level no.	E (ED)	E (DMRG)	E (ED)	E (DMRG)
2	0.0114*	0.0114*	0.0247*	0.0251*
3	0.0522	0.0522	0.0385	0.0391
4	0.0623	0.0624	0.0413	0.0418
5	0.0623	0.0624	0.0413	0.0419
6	0.0948	0.0949	0.0864	0.0876
7	0.1144	0.1145	0.0947	0.0959
8	0.1144	0.1145	0.0947	0.0961
9	0.1256	0.1256	0.1027	0.1039
10	0.1256	0.1258	0.1027	0.1054

excitations very accurately. The second calculation has $l > 100$. The entire spectrum is red shifted by an approximately constant amount because the density matrix now has projections from many excited states. Accordingly, we shift the spectrum by a constant and use the first calculation for the lowest excitations.

To illustrate the accuracy, we compare DMRG excitation energies for $l = 400$ and $\beta' = 10$ with exact results. The lowest 10 levels are listed in Table 3.1 for $N = 24$ and 32 at $\alpha = 2/3$, and in Table 3.2 at $\alpha = 1/2$. The $\alpha = 1/2$ levels are clearly denser than the $\alpha = 2/3$ levels that in turn are denser than the corresponding HAF levels (not listed). Translational symmetry for periodic boundary conditions makes possible the ED results in the Tables. The accuracy of the lowest 5 excitations is about 1 and 1.5%, respectively, for $\alpha = 2/3$ and $1/2$. The HAF accuracy is better than 1%. The accuracy up to level 100

is better than 5% and better than 10% for levels far higher than 100. Truncated partition functions are limited to $T \sim T'(N)$ that depends on system size as discussed below. Since the cutoff $W_C(N)$ is more than $10T'(N)$, the Boltzmann factors are very small. Accurate excitation energies are essential at low T.

To summarize, DMRG yields the excitations $E_j(\alpha, N) \leq W_C(\alpha, N)$ in models α with N spins in Eq. 3.3. Calculations are performed in sectors with Zeeman component $S^z = M$. The absolute ground state is in the $M = 0$ sector for $\alpha > \alpha_c$ and the $E_j(M, \alpha, N)$ are relative to $E_1(\alpha, N) = 0$.

3.2.2 Thermodynamics

The evolution of any thermodynamic quantity can be followed as the cutoff $W_C(N)$ is increased. The truncated partition function $Q_C(T, N)$ with $E_j(N) \leq W_C(N)$ in Eq. 3.4 is accurate at low T and merges with ED at $T > T_n(N)$ when the full spectrum is retained. However, computational resources limit $W_C(N)$ and thermodynamics to $T < T_n(N)$, as seen explicitly for ED at $N = 24$. We need a criterion for choosing the cutoff. $W_C(N)$ leads to $R_C(M, N)$ states in sectors with $S^z = M$. Since S is conserved, the total number of states is

$$R_C(N) = R_C(0, N) + \sum_{M=1}^{N/2} 2R_C(M, N). \tag{3.6}$$

The number of states in the $M = 0$ sector is more convenient and intuitive than $W_C(N)$ for discussing thermodynamics. We retain $10^3 - 10^4$ states at low T out of 2^N states.

We chose $W_C(N)$ based on the maxima of $S_C(T, N)/T$ and $\chi_C(T, N)$, where $S_C(T, N)$ is the entropy per spin and $\chi_C(T, N)$ is the magnetic susceptibility per spin. Both are reduced at low T by finite size gaps and at high T by truncation.

Fig. 3.2 illustrates the convergence of $S_C(T, N)/T$ and $\chi_C(T, N)$ for $N = 48$ and 64 at $\alpha = 2/3$ in Eq. 3.3. The logarithmic scale is to emphasize low T. The cutoff governs the number of states in the $M = 0$ sector. $R_C(0, N) = 400$ ensures adequate convergence with respect to finite size gaps. The truncated partition function has $R_C(N) = 1563$ and 1818 states, respectively, at $N = 48$ and 64.

Fig. 3.3 shows the same functions for $\alpha = 1/2$ in Eq. 3.3. The maxima of $S_C(T, N)/T$ and $\chi_C(T, N)$ are about twice as high and are shifted to lower T compared to $\alpha = 2/3$. However, the maxima are again converged with $R_C(0, N) = 400$ states. Now the truncated partition function has $R_C(N) = 1832$ and 2200 states, respectively, at $N = 48$ and 64. As implied by the $S(T)/T$ panel, there are many states with

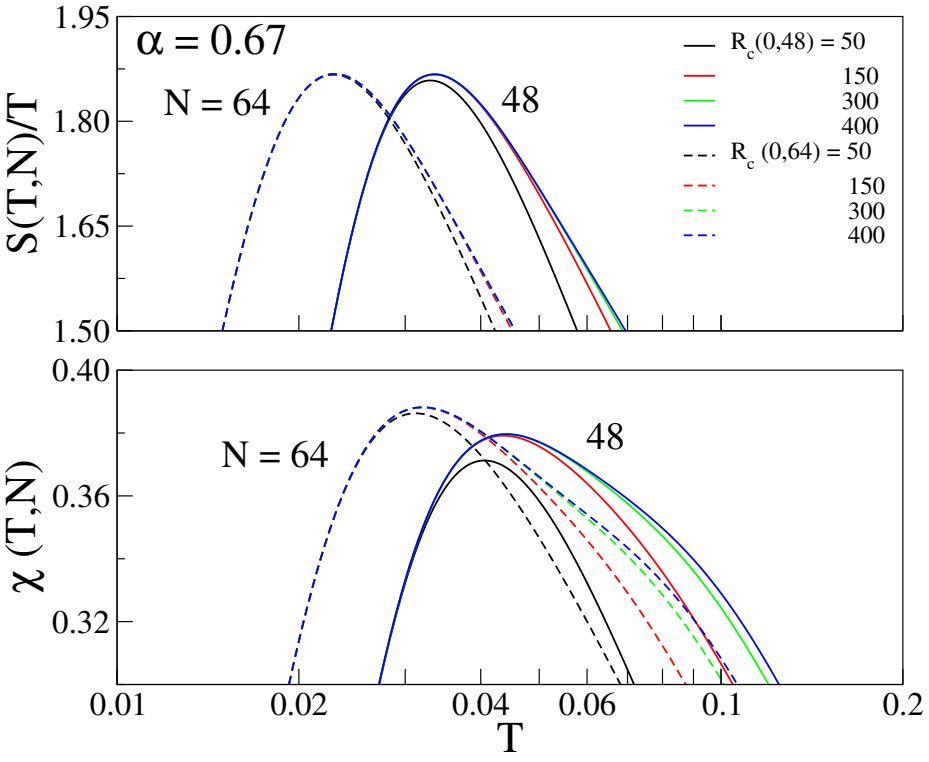

Figure 3.2: Convergence of the truncated $S_C(T,N)/T$ and $\chi_C(T,N)$ with increasing number of states in the $M = 0$ sector for $N = 48$ and 64 spins at $\alpha = 2/3$ in Eq. 3.3. The maxima are converged when the cutoff $W_C(N)$ leads to $R_C(0,N) = 400$ states.

$E_j(64) < 0.01$ where the numerical accuracy has to be considered. The $\alpha = 1/3$ spectrum has even smaller and denser excitations.

The full and truncated partition functions are given in Eq. 3.1 and Eq. 3.4. Truncation always reduces $Q(T,N)$. It also reduces the internal energy $E(T,N)$ as shown by taking the difference and noting that the sum below is over $E_j(N) > W_C(N) > E_C(T,N)$,

$$E(T,N) - E_C(T,N) = \frac{1}{Q(T,N)} \times \sum_j \left(E_j(N) - E_C(T,N)\right) \exp\left(-\beta E_j(N)\right). \tag{3.7}$$

It follows that truncation also reduces the entropy $S(T,N) = k_B \ln Q(T,N)/N + E(T,N)/NT$. Truncation is arbitrarily accurate for $\beta W_C(N) \gg 1$ and inevitably fails at high T.

We will necessarily be working with $S_C(T,N)$ in large systems. The function $S_C(T,N)/T$ has a maximum at $T'(N)$ where

$$S_C(T',N) = T'(N) S'_C(T',N). \tag{3.8}$$

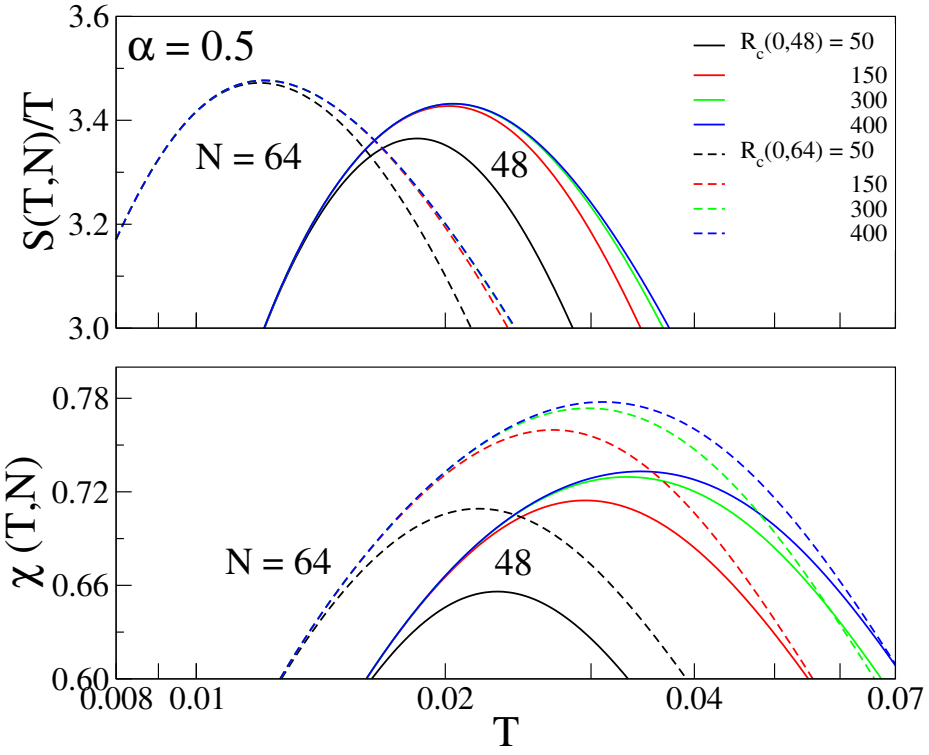

Figure 3.3: Convergence of the truncated $S_C(T,N)/T$ and $\chi_C(T,N)$ with increasing number of states in the $S^z = 0$ sector for $N = 48$ and 64 spins at $\alpha = 1/2$ in Eq. 3.3. The maxima are converged for cutoff $W_C(N)$ leads to $R_C(0,N) = 400$ states.

The same relation holds for the maximum of $S(T,N)/T$ or of $S(T)/T$. The maxima at $S_C(T',N)/T'$ in Fig. 3.2 and Fig. 3.3 are lower bounds on $S(T)/T$ in the thermodynamic limit. They are the most accurate approximation at truncation $W_C(N)$. Accordingly, the cutoff criterion is convergence at the maximum.

Truncation reduces the entropy but not necessarily the susceptibility. The difference between the full and truncated magnetic susceptibility per site is

$$\chi(T,N) - \chi_C(T,N) = \frac{1}{NTQ(T,N)} \times \sum_j \left(M_j^2(N) - M_C^2(T,N) \right) \exp\left(-\beta E_j(N)\right). \qquad (3.9)$$

The sum is over states $E_j(N) > W_C(N)$ with Zeeman components $S^z = M_k$, and $M_C^2(T,N)$ is the average value of M^2 over $E_j(N) \leq W_C(N)$. There is no guarantee that the sum is positive. However, we are always using a tiny fraction of states close to the singlet ground state and find that $\chi_C(T,N)$ converges from below with increasing $W_C(N)$. A satisfactory cutoff converges $\chi_C(T,N)$ to its peak. The $\chi_C(T,N)$ maxima in Fig. 3.2 and Fig. 3.3 are less converged than the $S_C(T,N)/T$ maxima.

The spectrum in the $M = 0$ sector is the densest since it includes a Zeeman component of all states with $S > 0$, and it has the largest truncation error. The following results are mostly based on cutoffs $W_C(\alpha, N)$ that retain 10 states with $M = 5$ and none with $M > 5$. The $M = 0$ and 1 sectors contain more than 400 states,nearly 1000 states, when the Zeeman components include the projection from sectors with higher M within cutoff $W_C(\alpha, N)$. The total number of states is $R_C = 4532$ and 2705 for $N = 48$ and 64, respectively at $\alpha = 2/3$, and 3647 and 2239 at 48 and 64 at $\alpha = 1/2$. The results are not sensitive to $W_C(N)$ provided the cutoff is high enough to enforce convergence at the maxima in Fig. 3.2 and Fig. 3.3.

3.2.3 Extrapolation

Fig. 3.4 shows the absolute spin susceptibility $\chi(T)$ and specific heat $C(T)$ of the HAF. N_A is Avogadro's number, μ_B is the Bohr magneton and g is the electronic g factor. We use reduced units from here on and label the axes of subsequent graphs as $\chi(T)$ or $S'(T) = C(T)/T$ vs. T.

ED (solid lines) clearly indicates converged $\chi(T)$ at $T > T_n = 0.20$. The peak at $T_m = 0.641$ and $\chi(T_m) = 0.147$ in the upper panel are quantitative [112]. DMRG (dashed lines) extends $\chi(T)$ to lower T and illustrates once again that finite-size gaps decrease with increasing system size. The squares on the DMRG curves are $\chi(T', N)$ evaluated at $T'(N)$, the maximum of $S_C(T, N)/T$. Open symbols are quantum Monte Carlo (QCM) calculations following Ref. 1 at $N = 48$, 100 and 256. The arrow marks the exact $\chi(0) = 1/\pi^2$. There are logarithmic corrections [112] at $k_B T/J_1 < 0.005$.

The lower panel of Fig. 3.4 shows the entropy derivative, $S'(T) = C(T)/T$, over the same range. The area under ED (solid) lines is $\ln 2$ and ED again converges for $T > 0.20$. The peak at $T^* = 0.307$ and $S'(T^*) = 0.897$ are quantitative [112]. The arrow marks the exact $S'(0) = 2/3$. DMRG (dashed lines) terminate at $T'(N)$, now shown as open circles. The $S'(T, N)$ maxima are at $T_m(N) < T'(N)$. We return later to the squares. DMRG and truncation is almost quantitative up to $T'(N)$, as seen from ED at $N = 24$. That is also the case for $\chi(T)$ at $T'(N)$ in the upper panel.

There are far fewer published $C(T, N)$ than $\chi(T, N)$ curves. Moreover, $C(T, N)$ plots completely obscure the behavior at low T where finite size effects are responsible for *deviations* from linearity. QMC works beautifully for $\chi(T)$ but produces scatter plots for $C(T, N)/T$ at low T; it is ill suited for narrow features such as the $T_m(N)$ peaks. Finite size effects are readily understood. Since $S(T_n)$ is in the thermodynamic limit and finite systems have $S'(0, N) = 0$, reduced $S'(T, N)$ at low T must be compensated by

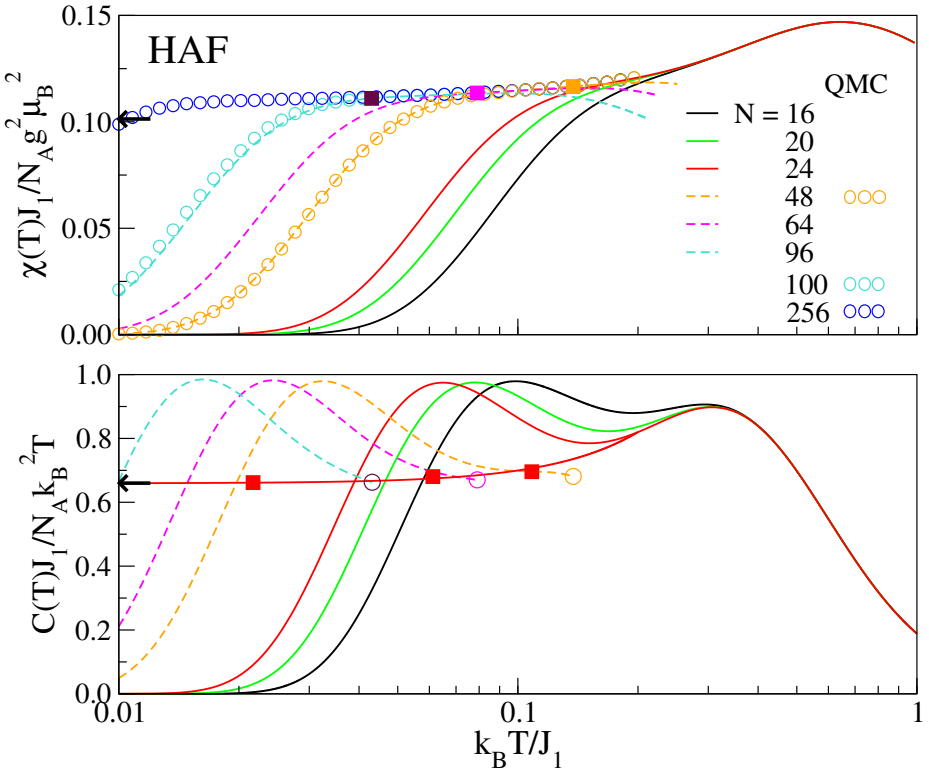

Figure 3.4: HAF results for $\chi(T)$ (upper panel) and $C(T)/T = S'(T)$ (lower panel). Solid and dashes lines are ED and truncated DMRG, respectively, at the indicated system size N. The QMC calculations of $\chi(T)$ follow Ref. 1. The arrows are exact at $T = 0$. The high T peak is fully converged in both panels. The DMRG lines for $C(T,N)/T$ terminate at $T'(N)$, the maximum of $S_C(T,N)/T$, shown as open circles (lower panel) and solid squares (upper panel). The squares and extrapolation in the lower panel are discussed in the text.

increased $S'(T,N)$ at $T < T_n$. The truncated $S'(T,N)$ have maxima at $T_m(N)$ where

$$S'_C(T_m,N) = \frac{C_C(T_m,N)}{T_m} > S'(T_m) \tag{3.10}$$

Convergence of $S'_C(T,N)$ to the thermodynamic limit is from above while $S_C(T,N)$ converges from below.

In order to extract the thermodynamic limit of $S'(T)$, we note that its maximum T^* is above T_n. The $S'(T,N)$ peaks are superimposed on a smooth background that we take as $S'(T) = a(1+bT+c^2T^2)$ for $T \leq T_n$. There are three parameters, a, b and c. Two are fixed by $S(T_n)$ and $S'(T_n)$. The third is fixed by the scaling $x(N) = S'(T_m)/S'(T_m,N) < 1$ for each truncated spectrum. We sought parameters for which $x(N)$ is size independent. The best choice had x between 68.5 and 69.4% for the $T_m(N)$ peaks from $N = 24$ to 96. The resulting $S'(T) = C(T)/T$ is the $T < T_n$ line in Fig. 3.4. We find $S'(0) = 0.659$ and

very small $b = 10^{-5}$. The exact result is $S'(0) = 2/3$ and $S'(T)$ is quadratic at low T [112] aside from logarithmic corrections below $T = 0.005$.

We conclude that hybrid ED/DMRG works well for the HAF's spin susceptibility and specific heat. The HAF is especially simple: spin-1/2, one spin per unit cell, one exchange and hence no frustration. We did not appreciate that improved extrapolation is needed for the frustrated $J_1 - J_2$ model in Eq. 3.3. The $S'(T,\alpha)/T$ peak at $T^*(\alpha)$ shifts to $T < T_n(\alpha)$ and reaches $T = 0$ near the critical point α_c. Agreement with the HAF is necessary but not sufficient.

3.3 Thermodynamics of $J_1 - J_2$ models

In this section we study the $J_1 - J_2$ model with $\alpha \geq \alpha_c = 1/4$ in Eq. 3.3. Its quantum phases have already been mentioned. The general TMRG study of Lu et al. [74] has results for J_1, J_2 of either sign and discusses the thermodynamics of both singlet and FM phases. Sirker [72] later applied TMRG to the singlet phases of FM/AFM chains with α ranging from α_c to 2. QMC is not applicable to frustrated interactions. The ground state is a singlet ($S = 0$) and is doubly degenerate in the IC phase.

ED up to 24 spins converges to the thermodynamic limit for $T > T_n(\alpha)$ as seen in Fig. 3.4 for the HAF. The $T_n(\alpha)$ in Table 3.3 are in units of $|J_1|/k_B$. They are based on $S'(T,N) = C(T,N)/T$, whose size dependence is usually stronger than that of $\chi(T,N)$. The increasing density of states in Fig. 3.1 with decreasing α accounts for an order of magnitude variation of $T_n(\alpha)$. The area per spin under $S'(T,\alpha,N)$ curves is respectively ln 2 for ED and $(\ln R_C(\alpha,N))/N$ for DMRG, where $R_C(\alpha,N)$ is the truncated number of states in Eq. 3.6.

The singlet quantum phases of spin-1/2 chains are either gapless with a nondegenerate ground state

Table 3.3: Reduced temperature $T_n(\alpha)$ at which the thermodynamic limit of $S'(T,\alpha) = C(T,\alpha)/T$ is reached for $N = 24$ spins in $J_1 - J_2$ models with frustration α in Eq. 3.3.

Model, α	$T_n(\alpha)$	$S(T_n,\alpha)$	$S'(T_n,\alpha)$
$\alpha_c = 1/4$	0.02	0.413	2.665
1/3	0.06	0.481	1.838
1/2	0.14	0.399	1.656
2/3	0.17	0.293	1.533
HAF	0.20	0.143	0.820

or gapped with a doubly degenerate ground state [122]. The HAF is gapless while the $J_1 - J_2$ model has both gapped and gapless singlet phases. The HAF has logarithmic contributions to $\chi(T)$ and $C(T)$ at $T < 5 \times 10^{-3}$ that are followed to several decades lower T in Ref. 112. The gapped incommensurate (IC) phase runs from the exact quantum critical point [28] $\alpha_c = 1/4$ to another critical point [21, 27] around $\alpha = 0.806$. The IC gap $\Delta(\alpha)$ is exponentially small [123], however, and has yet to be evaluated. The ground state degeneracy is followed numerically using DMRG with periodic boundary to compute the static structure factor $F(q, \alpha)$ at wave vector q [21, 27]. The $F(q, \alpha)$ peaks at $\pm q(\alpha)$ shift in the IC phase from $q(1/4) = 0$ to $q(0.806) = \pi/2$. The decoupled phase [21, 27] for $\alpha > 0.806$ is gapless and commensurate. Its singlet ground state is nondegenerate and has quasi-long-range order with $q = \pi/2$.

Neither logarithmic corrections nor an IC gap matters for the thermodynamics at $T > 0.01$. Returning to Table 3.3, we note that the average value of $S'(T_n, \alpha)$ up to $T_n(\alpha)$ is $S(T_n, \alpha)/T_n$ and does not depend on the actual form of $S'(T_n, \alpha)$ in the interval. Since the average at $\alpha = 1/3$ is more than four times $S'(T_n, 1/3)$, we infer that $S'(T, 1/3)$ decreases with T. Although not as strongly, $S'(T, 1/2)$ and $S'(T, 2/3)$ also decrease with T while the HAF has increasing $S'(T)$ to $T^* > T_n$.

3.3.1 Critical point, $\alpha_c = 1/4$

Thermodynamics at the critical point is remarkably different from larger α. ED results in Fig. 3.5 for $S'(T, \alpha_c)$ and $\chi(T, \alpha_c)$ in reduced units are almost power laws over several decades in T. The approximate exponents are $\gamma = -1.18$ and -0.97, respectively. ED to $N = 24$ at the critical point indicates that $T_n(\alpha_c) \sim 0.02$ and shows the stronger size dependence of $S'(T, N)$. $S'(T)$ is a measure of thermal fluctuations while $\chi(T)$ measures fluctuations of M^2, where $-S \leq M \leq S$ are the Zeeman levels of spin-S states.

Sirker et al. [29] studied the $J_1 - J_2$ model in zero field on the FM side, $0 \leq \alpha \leq \alpha_c = 1/4$, using field theory and numerical methods. To leading order in T, the exact $\chi(T, \alpha_c)$ is $AT^{-4/3}$ with $A \sim 0.1685$ according to field theory and scaling for the classical model. Modified spin wave theory for the quantum model returns the same exponent with $A' \sim 0.0992$. The reported susceptibility at $T = 10^{-3}$ is $\chi(10^{-3}) = A$ or $A' \times 10^4$ while ED for for the quantum chain of $N = 24$ gives 0.0882×10^4. Such excellent agreement speaks to the accuracy of field theory and of ED at $N = 24$ for the thermodynamic limit at the critical point. On the other hand, the $\chi(T, \alpha_c)$ exponent in Fig. 3.5 deviates considerably from

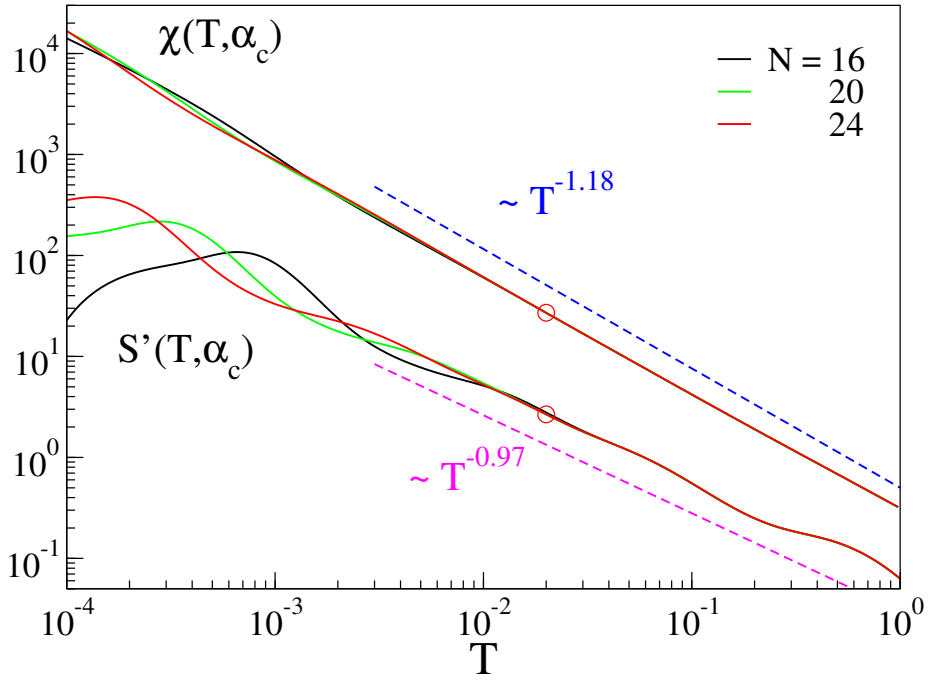

Figure 3.5: $\chi(T,\alpha_c)$ and $S'(T,\alpha_c)$ in reduced units at the critical point, $\alpha_c = 1/4$. Open circles are at $T_n(\alpha_c) = 0.02$ where the thermodynamic limit is reached for ED up to 24 spins.

$-4/3$. TMRG [29] between $T = 0.003$ and 1 gives slightly different exponents clustered around $T^{-1.2}$, consistent with Fig. 3.5. Several reasons for the discrepancy were discussed [29], including the possibility that TMRG could not reach sufficiently low T. The leading term of field theory is limited to $T < 10^{-3}$ and in this case ED to $N = 24$ reaches lower T.

To leading order in T, the field theory [29] free energy $A(\alpha_c)$ goes as $-T^{5/4}$. The entropy $S(T)$ and $S'(T)$ go as $T^{1/4}$ and $T^{-3/4}$, respectively. The calculated exponent of $S'(T,\alpha_c)$ is $\gamma \sim -0.97$ rather than -0.75 for $T > 0.01$. The $S'(T,\alpha_c)$ exponent in this range is more negative than that of field theory while the $\chi(T,\alpha_c)$ exponent is less negative. Hence $C(T,\alpha_c)$ goes as $T^{0.03}$ and is almost constant.

Field theory [29] indicates spectacular singularities at α_c: $S'(T,\alpha_c)$ and $\chi(T,\alpha_c)$ diverge at $T = 0$ while an IC gap $\Delta(\alpha)$ implies $S'(0,\alpha) = \chi(0,\alpha) = 0$ for $\alpha > \alpha_c$. This is a mathematical result. In the present context, it is instructive to contrast α_c in Fig. 3.5 with the HAF in Fig. 3.4. Increasing AFM exchange J_2 over the range $\alpha_c < \alpha < \infty$ reduces both $\chi(T)$ and $C(T)/T$ by orders of magnitude at $T \sim 10^{-3}$ and by much less at $T \sim 0.1$, where thermal fluctuations are much stronger. The steep power-law T decrease of both at α_c evolves into the weak T dependence with a maxima at $T > 0$ in the HAF. Entropy conservation ensures the crossing of $S'(T,\alpha)$ curves with different α while AFM exchange accounts for

$\chi(T,\alpha') < \chi(T,\alpha)$ when $\alpha' > \alpha$. The qualitative changes from α_c to the HAF provide a framework for the thermodynamics at intermediate α.

3.3.2 Coupled sublattices, $\alpha = 2/3$

The $\alpha \to \infty (J_1 = 0)$ limit of Eq. 3.3 corresponds to HAFs on sublattices of odd and even numbered sites. Finite $J_1 < 0$ couples the HAFs and, as shown in Fig. 3.6 at $\alpha = 2/3$, increases both $\chi(T,\alpha)$ and $C(T,\alpha)/T$ compared to Fig. 3.4. Finite size effects are more prominent and the HAF extrapolations no longer suffice. The reason is that $S(T,\alpha)/T$ either decreases monotonically or has a maximum at $T^* < T_n(\alpha, N)$. We consider an alternative analysis before discussing the $\alpha = 2/3$ results.

We suppress the model index α and recall that the truncated entropy $S_C(T,N)$ converges to $S(T,N)$ from below. The approximation that relates finite N to the thermodynamic limit is

$$\frac{S_C(T',N)}{T'} \leq \frac{S(T',N)}{T'} \leq \frac{S(T')}{T'} \equiv \langle S'(T) \rangle_{T'} \tag{3.11}$$

where $T'(N)$ is the maximum defined in Eq. 3.8. It follows that $T'(N)$ is less than $T_n(N)$ but greater than $T_m(N)$, the maximum of $S'(T,N)$ in Eq. 3.10, where $S'(T_m,N) > S'(T_m)$. We note that $S_C(T',N)$ is a lower bound for $S(T')$ and use $T'(N)$ to approximate the thermodynamic average $\langle S'(T) \rangle$ between $T = 0$ and $T'(N)$. Each system size generates a point at $T'(N)$. It is convenient to define $T_1 = T'(N_1)$ for the largest system, $T_2 = T'(N_2)$ for the second largest, and so on.

The mean value theorem can be applied to successive intervals to estimate

$$S'(T_1/2) \approx \frac{S(T_1)}{T_1}, \qquad 0 \leq T \leq T_1 S'((T_1+T_2)/2) \approx \frac{S(T_2)-S(T_1)}{T_2-T_1}, \quad T_1 \leq T \leq T_2 \tag{3.12}$$

and similarly at $T = (T_2+T_3)/2$. This simple approximation is accurate when the size dependence of $S(T',N)/T'$ is weak. The final point at $S(T_n)/T_n$ is in the thermodynamic limit, where $S'(T_n)$ is also known. There is one input at each $T'(N)$ and two at T_n for estimating $S'(T)$ up to T_n. The mean-value estimate could be replaced by linear, quadratic or other fits. That is premature, however, because Eq. 3.11 returns an approximate $S(T')/T'$ and experience with other models is needed first.

ED and DMRG results for $\chi(T,N)$ are shown in the upper panel of Fig. 3.6 for $H(2/3)$ in Eq. 3.3. The thermodynamic limit holds for $T > T_n(2/3) = 0.17$. The $\chi(T)$ maximum at $T_m = 0.281$ is lower

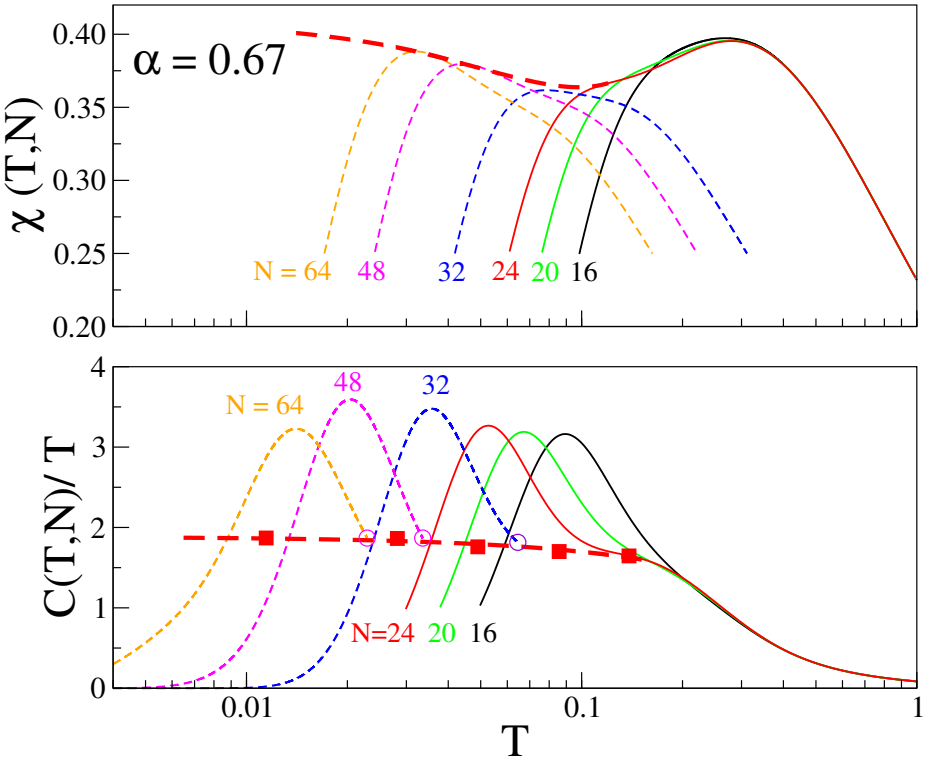

Figure 3.6: Upper panel: $\chi(T, N)$ for $\alpha = 2/3$ and N spins in Eq. 3.3. Solid and dashed lines are ED and DMRG. The bold dashed line is the estimated $\chi(T)$ in the thermodynamic limit. Lower panel: $C(T, N)/T$ for the same systems. Open circles are $T'(N)$, the maxima in Eq. 3.8. Squares are Eq. 3.12, the mean value in successive $T'(N)$ intervals; the dashed line connecting them is to guide the eye.

than 0.6413 for the HAF and $\chi(T_m) = 0.395$ is almost three times higher due to FM exchange J_1. The bold dashed line that approximates the thermodynamic limit is linear extrapolation of the $N = 48$ and 64 maxima. The upturn of $\chi(T)$ at low T is consistent with TMRG at $\alpha = 0.6$ in Fig. 1 of Ref. 72. So are the magnitude at the peak and the lowest accessible T.

The lower panel of Fig. 3.6 shows $S'(T) = C(T)/T$ and large finite-size peaks. The DMRG curves stop at $T'(N)$, the maximum of $S_C(T, 2/3, N)/T$, which are shown as open circles. The squares are the mean value approximation, Eq. 3.12, which returns the squares in Fig. 3.4 (lower panel) when be applied to $S'(T)$ for the HAF. We find $S'(0) \sim 1.88$ at $\alpha = 2/3$, again about three times the HAF value. $S'(T)$ gently decreases with T at $\alpha = 2/3$ instead of gently increasing in the HAF.

3.3.3 Incommensurate phase

The $J_1 - J_2$ model at $\alpha \geq 2/3$ can be viewed as HAFs on sublattices with FM exchange $J_1 < 0$ reaching $-3J_2/2$ at $\alpha = 2/3$. The singlet ground state persists for more negative J_1 down to $\alpha_c = 1/4$ where as

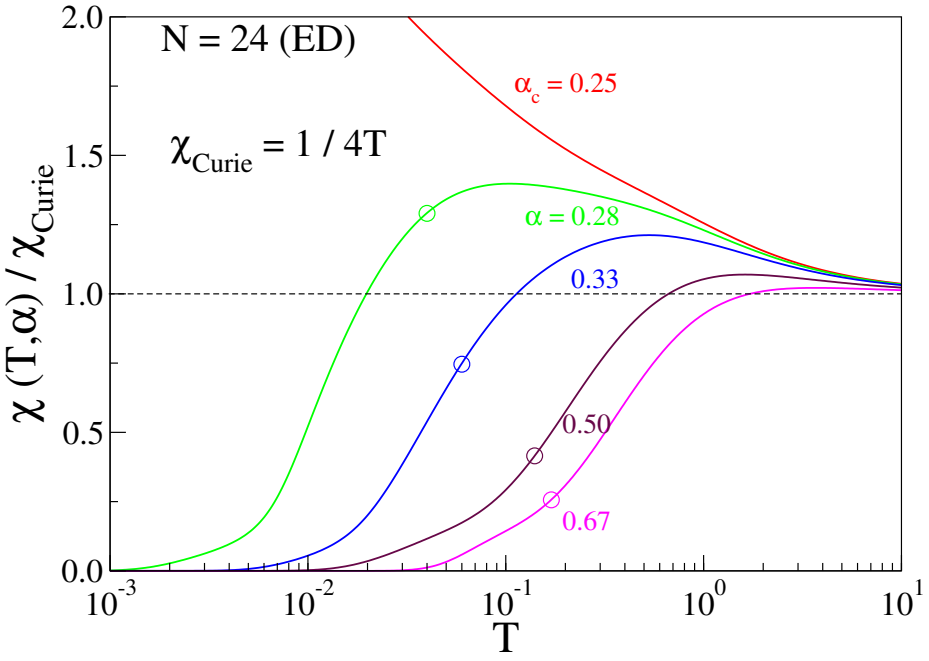

Figure 3.7: $4T\chi(T,\alpha)$ for 24 spins in Eq. 3.3. Open circles mark $T_n(\alpha)$ where the thermodynamic limit is reached. The dashed line corresponds to free spins. Deviations above or below indicate that the net interaction is FM or AFM.

seen in Fig. 3.5 both $C(T)/T$ and $\chi(T)$ decrease sharply with increasing T. The $\alpha_c < \alpha < 2/3$ regime is particularly challenging. The thermodynamics is governed by weak AFM exchange $J_2 < |J_1|$ at low T and strong FM exchange J_1 at high T.

The Curie law for free spins is $\chi_C = 1/4T$ in reduced units. The $\chi(T,\alpha,24)/\chi_C$ curves in Fig. 3.7 deviate from free spins due to competing FM and AFM exchanges. The "Curie temperatures" $T_C(\alpha)$ at which $\chi(T,\alpha)/\chi_C = 1$ are in the thermodynamic limit, above the $T_n(\alpha)$ in Table 3.3. Offsetting FM and AFM exchanges lead to free-spin behavior at $T_C(\alpha)$, much as attractive and repulsive interactions in gases cancel at the Boyle temperature. The exact [29] $T^{-1/3}$ divergence at α_c is completely suppressed for $\alpha > \alpha_c$. The $T = 0$ limit of $\chi(T,\alpha)/\chi_C$ is zero for either gapless or gapped chains with singlet ground states.

Finite size gaps typically decrease roughly as $1/N$, but this expectation can fail in frustrated systems. The first (starred) excitation $E_2(N)$ in Table 3.2 for $\alpha = 1/2$ is twice as large at $N = 32$ than at $N = 24$. This singlet becomes degenerate with the ground state in the IC phase. The degeneracy for $N = 4n$ spins is limited to n points $\alpha_j(N)$. The first is always $\alpha_c = 1/4$ while the last point $\alpha_n(N)$ increases with N. The $\alpha_j(N)$ are not distributed uniformly but are densest near the critical point [121]. The gap $E_2(N,\alpha)$ at constant α varies randomly in large systems when $\alpha_n(N) > \alpha$. It vanishes when $\alpha = \alpha_j(N)$, is finite elsewhere, and decreases slowly with N as the number of degenerate points increases. ED indicates [121]

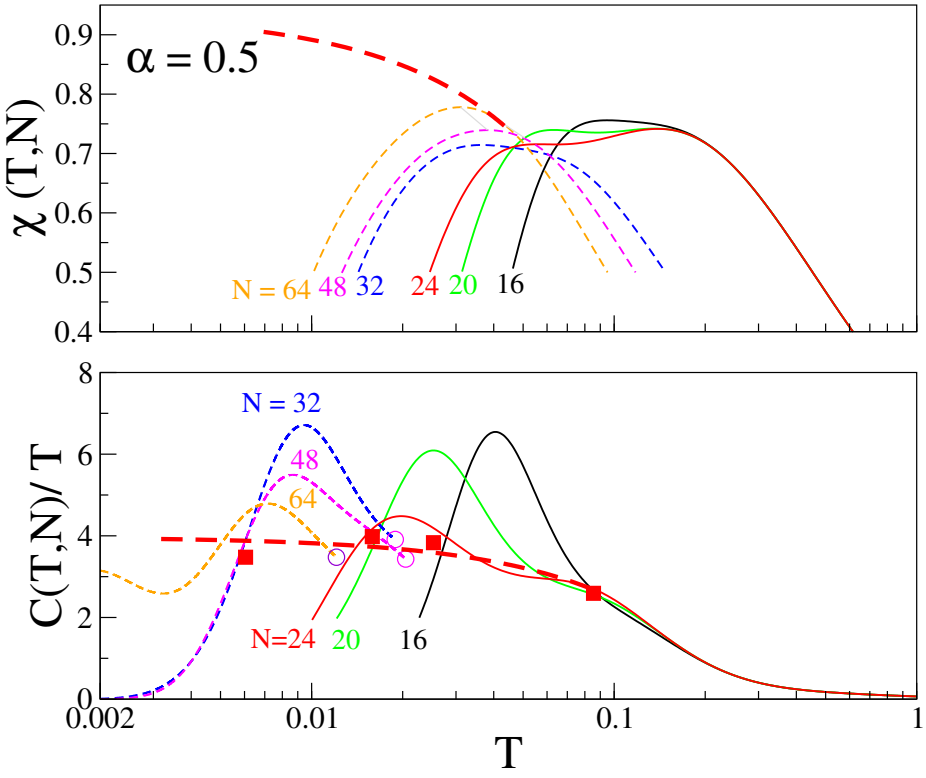

Figure 3.8: Upper panel: $\chi(T,N)$ for $\alpha = 1/2$ and N spins in Eq. 3.3. Solid and dashed lines are ED and DMRG. The bold dashed line is the estimated $\chi(T)$ in the thermodynamic limit. Lower panel: $C(T,N)/T$ for the same systems. Open circles are $T'(N)$, the maxima in Eq. 3.8. Squares are Eq. 3.12, the mean value in successive $T'(N)$ intervals; the bold dashed line is to guide the eye.

that $\alpha_6(24) < 1/2 < \alpha_7(28)$ while DMRG shows [21, 27] that $\alpha_{48}(192) = 0.66$. Hence $E_2(N)$ is already important at $N = 24$ for $\alpha = 1/2$ but not until much larger N for $\alpha = 2/3$.

Fig. 3.8 shows $\chi(T)$ and $C(T)/T$ curves at $\alpha = 1/2$. As expected, stronger FM exchange compared to $\alpha = 2/3$ increases both and shifts them to lower T. The $\chi(T,N)$ peak increases with N and shifts to lower T at large N, but $\chi(T,N)$ decreases with N at $T \sim 0.1$. The bold dashed line is linear extrapolation of the N = 48 and 64 peaks, shifted up slightly since since the thermodynamic limit is reached from below. It is quite approximate: $\chi(T,1/2) \sim 0.9$ at $T \sim 0$ and decreases to ~ 0.7 at $T \sim 0.06$. The weak maximum of 0.74 at $T = 0.14$ is in the thermodynamic limit.

The $C(T)/T$ curves in the lower panel have similar $T'(32) \sim T'(48)$ that reflect the approximate nature of Eq. 3.11. We averaged both $T'(32)$, $T'(48)$ and $S(T',32), S(T',48)$ to obtain the squares using Eq. 3.12 for the mean values in the thermodynamic limit. The dashed line indicates linear $C(T) \sim 4T$ from $T =$ 0.01 to 0.03 with downward deviation at 0.04 for $\alpha = 0.5$ in the thermodynamic limit. TMRG [72, 74] for $C(T)$ at $\alpha = 0.4$ was extended [124] down to $T = 0.01$. As seen Fig.5 of Ref. 124, $C(T) \sim 0.05$ at

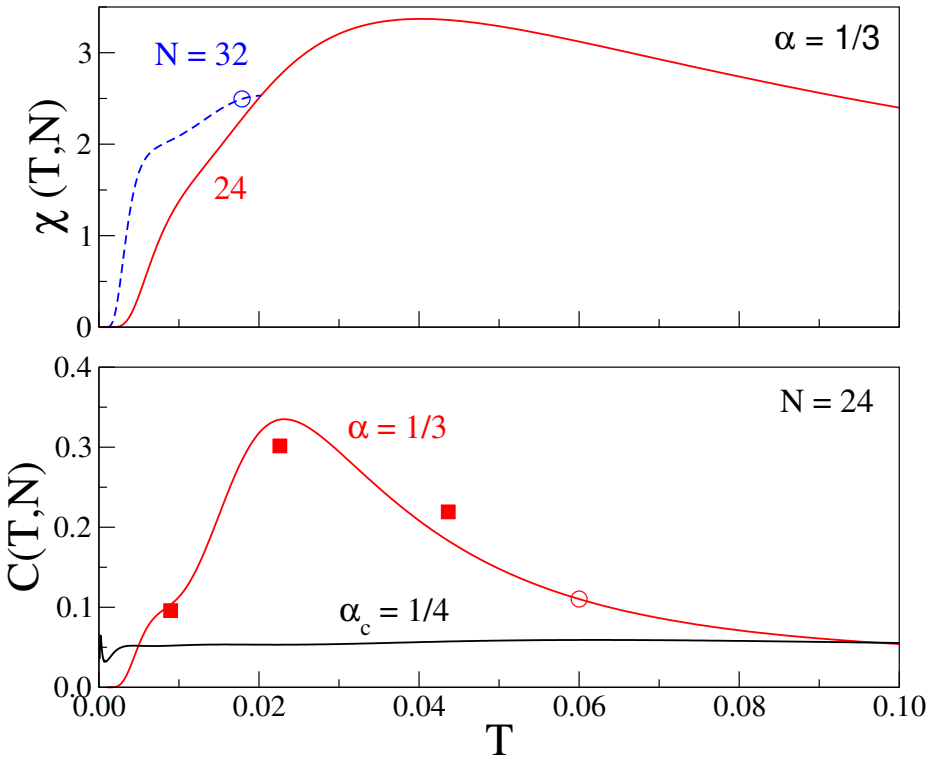

Figure 3.9: Upper panel: $\chi(T,N)$ for $\alpha = 1/3$ in Eq. 3.3 and ED for $N = 24$ spins and DMRG for 32 spins up to the open circle at $T'(32)$. Lower panel: $C(T,N)$ for $\alpha = 1/3$ and 1/4 for $N = 24$. The solid squares are based on DMRG for $N = 32$ and Eq. 3.12 for three intervals based on $T'(32)$,$T'(24)$ and the open circle at $T_n(24) = 0.06$.

$T = 0.01$. It is almost linear in T up to $T = 0.03$ and deviates downward at 0.04. The T dependence is similar and $C(T)$ is known to increase at low T with decreasing α in the singlet phase.

The degeneracies $\alpha_j(N)$ are closely spaced at $\alpha = 1/3$ and the excitations $E_j(N)$ are both small and dense. Numerical considerations discussed in Section 3.2 limit us to $N = 32$. On the other hand, the thermodynamic limit is already reached at $T_n(1/3) = 0.06$.

We switch in Fig. 3.9 to a linear T scale for $\chi(T)$ and $C(T)$ up to $T = 0.10$, the Curie T for free spins. AFM correlations at lower T lead to slower than $1/T$ increase of $\chi(T)$ and a maximum at $T \sim 0.04$. The truncated $\chi(T,32)$ peak confirms that $\chi(T)$ decreases in the thermodynamic limit at least to $T = 0.02$. The estimated $T \sim 0$ value of ~ 1.7 is more than 10 times that of the HAF. TMRG [72] at $\alpha = 0.3$ indicates a $\chi(T)$ maximum at $T \sim 0.02$. This is consistent with Fig. 3.9 since the peak shifts to $T = 0$ just above $\alpha_c = 1/4$.

We have three intervals for $C(T,N)/T$ based on $T'(32) = 0.0179$, $T'(24) = 0.0273$ and $T_n = 0.06$. The mean values using Eq. 3.12 lead to the squares in the lower panel. The exact $C(T,1/3,24)$ calculation

was first reported in Ref. 125. Our results for $T < T_n$ suggest that the peak in the thermodynamic limit is slightly lower and shifted to higher T. Also shown is the specific heat $C(T, 1/4) \sim T^{0.03}$ at the critical point. It is almost constant in this interval since the $C(T)/T$ exponent in Fig. 3.5 is close to -1.

Spinless fermions [126] can be used to represent spin-1/2 chains; the $S^z = 0$ ground state corresponds to a half-filled band. The HAF has two-fermion interactions while the $J_1 - J_2$ model, Eq. 3.3, has up to four-fermion interactions. Both $C(T)/T = S'(T)$ and $\chi(T)$ are proportional to the density of states at the Fermi energy as $T \to 0$. The Wilson-Sommerfeld ratio in reduced units is

$$R_W(T) = \frac{4\pi^2 \chi(T)}{3S'(T)} \tag{3.13}$$

$R_W(T) = 1$ for free fermions, independent of T. The HAF result is $R_W(0) = 2$ with 10% variations up to $T = 0.4$ [112]. The $J_1 - J_2$ model has increased $R_W(0.01) \sim 2.6$ at $\alpha = 2/3$ and > 2.8 at $\alpha = 1/2$. Much larger $R_W(0.01) \sim 150$ is found at $\alpha_c = 1/4$. $R_W(\sim 0)$ increases when low-energy excitations have large S because $C(T)/T$ contributions go as the $(2S + 1)$, the Zeeman degeneracy, while $\chi(T)$ contributions go as $S(S + 1)(2S + 1)/3$, the sum over M^2.

3.4 Discussion

We have presented a hybrid ED/DMRG approach to the thermodynamics of 1D models that never requires the full energy spectrum $\{E(N)\}$ of large systems and tested it in Section 3.2 against the spin-1/2 HAF. The 2^N states of spin-1/2 chains are found exactly in small systems and suffice for the thermodynamics at high T. DMRG for larger systems is used to obtain the lowest few thousand excitations $E_j(N)$. Thermodynamics at low T is based on the truncated spectrum $E_j(N) \leq W_C(N)$. The cutoff criterion is convergence to the maximum of $S_C(T, N)/T$ and $\chi_C(T, N)$ with T, where $S_C(T, N)$ and $\chi_C(T, N)$ are respectively the truncated zero-field entropy and susceptibility per site. The thermodynamic limit at T is approximated by maximum of $S_C(T, N)/T$ or of $\chi_C(T, N)$ at system size N.

Exact diagonalization (ED) of the HAF with $N = 24$ spins becomes quantitative for $T \geq 0.20J/k_B$ as shown in Fig. 3.4. DMRG up to $N = 96$ extends the thermodynamic limit for $\chi(T)$ and $S'(T) = C(T)/T$ to an order of magnitude lower T, in excellent agreement with exact and numerical results. We are studying the performance of DMRG and truncation in 1D systems such as half-filled Hubbard, extended Hubbard

and related models with charge as well as spin degrees of freedom. These models reduce to the HAF in the atomic limit. Charge degrees of freedom limit ED to smaller $N < 20$ with larger finite size gaps. There is greater scope for DMRG and truncation before running into the accuracy issues discussed in Section 3.2.1.

The motivation for this work was the thermodynamics of the frustrated $J_1 - J_2$ model, Eq. 3.3,which is the starting point for the magnetic properties of several compounds with CuO_2 chains. F exchange $-J_1 > J_2$ is inferred [22, 116–120] at high T from Curie-Weiss fits of $\chi(T)$ over a limited interval in which deviations from free spins in Fig. 3.7 are positive, but different J_1, α combinations return [50, 74] similar $\chi(T)$. The net interaction is AFM at low T where an applied field can induce the FM state in some system. The $J_1 - J_2$ model specifies the entire range of magnetization and magnetic specific heat. The data set [22] for $LiCuSbO_4$ were successfully modeled [50] by $|J_1| = 28.7$ K and $\alpha = 2/3$ down to $T \sim 5$ K ($T/|J_1| \sim 0.17$) where finite-size gaps limit $N = 24$ results. Data below 5 K require improved thermodynamics as well as taking into account corrections to isotropic exchange and other magnetic interactions.

In an applied magnetic field, the $J_1 - J_2$ model with anisotropic exchange supports a number of exotic quantum phases: IC, multipolar, vector chiral, among others [23, 114, 127]. The nature of the ground states, spin correlations and hidden symmetries are active areas of research, primarily of $T \to 0$ properties. That limit is beyond our approach. We alluded in the Introduction to mathematical and physical motivations. The CuO_2 chains have $-J_1 \sim 10^2$ K and anisotropic g-tensors that indicate $5 - 10\%$ deviations from isotropic exchange. Direct comparisons of the $J_1 - J_2$ model, Eq. 3.3, are limited to $T > 1$ K ($T > 0.01$ in reduced units), below which spin-orbit coupling and other magnetic interactions must be included. Considerably lower T is relevant to exact field theory results at α_c, for the gap $\Delta(\alpha)$ in the IC phase, or for logarithmic corrections. Quantitative analysis of magnetic data in the $1 - 10$ K range will be needed extract model parameters.

The hybrid ED/DMRG approach exploits the fact that the thermodynamic limit is reached at high T in small systems that can be treated exactly. DMRG generates the excitations and truncated partition functions of increasingly large systems. We have focused on the spin susceptibility and specific heat of spin-1/2 chains. Other thermodynamic quantities are equally accessible, as indeed are applications to any 1D quantum cell model.

4

Modeling the spin-Peierls transition of spin-1/2 chains with correlated states

4.1 Introduction

The spin-Peierls (SP) transition is a characteristics that occurs in a limited number of AFM 1D or quasi-1D spin systems [3]. At high T, the SP systems has equally spaced atoms. Below a transition T, called spin-Peierls transition T (T_{SP}), an elastic distortion occurs and each atom shifts from their relaxed position close to one of its neighbor and moves away from the other neighbor. This distortion in SP system is a low T property which results in opening of magnetic gap due to singlet pairing of closer spins. Thus lattice distortion induces dimerization in SP systems below T_{SP} which decreases magnetic free energy. However, the lattice free energy is increased due to elastic distortion. When the decrease of electronic free energy exceeds the increase of lattice free energy, the distortion is spontaneous. The distortion and the induced magnetic gap below T_{SP} is T dependent quantities. This situation resembles Peierls transition. Peierls' theorem states that a 1D half-filled metal with equally spaced ion is unstable. At low T, the 1D chain distorts spontaneously which increases the lattice periodicity, decreases the Brillouin zone and introduces a gap at the Fermi level. This is a transition from metal to insulator. However, SP transition is not a metal to insulator transition and SP systems are insulator at all T.

We model in this Chapter [1] the first organic and first inorganic compound where SP transition was found.. It was first discovered in the organic crystal TTF-$CuS_4C_4(CF_3)_4$ at $T_{SP} = 12$ K by Jacobs et al. [2]. The spin-1/2 chain at $T > T_{SP}$ has equally spaced cation radicals TTF^+ and is dimerized at lower T as discussed in Chapter 1. They analyzed the magnetic susceptibility $\chi(T)$ using the linear HAF with equal exchange J_1 to both neighbors for $T > T_{SP}$ and alternating exchange $J_1(1 \pm \delta(T))$ in the dimerized phase. The T dependence of $\delta(T)$ followed the BCS gap equation of superconductors. Subsequently, Hase et al. [4, 5] identified the inorganic spin-Peierls crystal $CuGeO_3$ with $T_{SP} = 14$ K based on spin-1/2 chains of Cu(II) ions. The magnetic susceptibility at $T > T_{SP}$ indicated [128] exchange $J_2 = \alpha J_1$ with $\alpha = 0.35$ between second neighbors in addition to J_1. However, $\delta(T)$ did not follow BCS and extensive $CuGeO_3$ studies have been inconclusive [129] with respect to frustration α. These prototypical spin-Peierls (SP) crystals have been analyzed with correlated states for $T > T_{SP}$ but only as uncorrelated or mean field for $T < T_{SP}$.

Spin-1/2 chains have been long studied theoretically as simple 1D systems with two states, α and β, per site. The linear HAF is the $\alpha = 0$ limit of the $J_1 - J_2$ model, Eq. 4.4 below. The HAF may well be the best characterized many-body system, and the $J_1 - J_2$ model also has an extensive literature.

The electronic problem for SP transitions is to obtain the thermodynamic limit of the free energy per site $A(T, \delta)$ at temperature T and dimerization δ. In reduced ($J_1 = 1$) units, we have

$$A(T, \delta) = -T \ln Q(T, \delta). \tag{4.1}$$

The thermodynamic limit is known for free fermions but not for correlated systems such as the HAF or the $J_1 - J_2$ model. SP modeling has consequently been approximate and subject to revision due to computational advances. In particular, we show below that $\delta(T)$ for the HAF does *not* follow BCS.

We model both transitions with a recent method that combines exact diagonalization (ED) of short chains with density matrix renormalization group (DMRG) calculations of progressively longer chains [81]. The premise is that the full spectrum $\{E(\delta, N)\}$ of large systems is never needed. Since T limits the range

[1] The work reported here is based on "*Modeling the spin-Peierls transition of spin-1/2 chains with correlated states: $J_1 - J_2$ model, $CuGeO_3$, and TTF-$CuS_4C_4(CF_3)_4$* ", Sudip Kumar Saha, Monalisa Singh Roy, Manoranjan Kumar, and Zoltán G. Soos, Phys. Rev. B, vol. 101, p. 054411, 2020 and "*Bond-bond correlations, gap relations and thermodynamics of spin-1/2 chains with spin-Peierls transitions and bond-order-wave phases*", Sudip Kumar Saha, Manoranjan Kumar, and Zoltán G. Soos, Journal of Magnetism and Magnetic Materials vol. 519, p. 167472, 2021.

of spin correlations, ED is sufficient once the system size exceeds the correlation length. Bonner-Fisher results [130] to $N = 12$ were used [2] for $\chi(T)$ of TTF^+ chains at $T > T_{SP}$. ED to $N = 24$ is now accessible. DMRG for larger N yields the spectrum $\{E(\delta, N)\}$ up to some cutoff $E_C(\delta, N)$, thereby extending thermodynamics to lower T. The hybrid approach is particularly well suited for SP systems because dimerization opens a gap that limits spin correlations at $T = 0$.

The driving force for dimerization is the partial derivative $\partial A(T, \delta)/\partial\delta$ that is opposed by the lattice. The simplest lattice model is used in conventional approaches [131–133] to the Peierls or SP instability: the coupling is linear, the potential energy $\delta^2/2\varepsilon_d$ per site is harmonic, and the stiffness $1/\varepsilon_d$ is independent of T. The equilibrium dimerization is

$$\frac{\delta(T)}{\varepsilon_d} = -\left(\frac{\partial A(T,\delta)}{\partial\delta}\right)_{\delta(T)}. \tag{4.2}$$

At $T = 0$, $A(0, \delta) = E_0(\delta)$ is the ground state energy per site. DMRG returns the derivative $E_0'(\delta, N)$ of large systems and the extrapolated limit $E_0'(\delta)$. Dimerization decreases and vanishes at T_{SP}, where $1/\varepsilon_d = -A''(T_{SP}, 0)$. In principle, the observed T_{SP} is the model parameter that specifies both the stiffness and $\delta(T)$. To emphasize the point, we refer to the equilibrium susceptibility as $\chi(T, T_{SP})$ over the entire range. Moreover, the driving force is a property of the electronic system that is balanced by whatever model is adopted for the lattice.

The equilibrium dimerization is explicitly known for free fermions; $\delta(T)$ for a half-filled tight-binding band is given by

$$\frac{1}{\varepsilon_d} = \frac{8}{\pi}\int_0^{\pi/2} dk \frac{\sin^2 k}{\varepsilon\,(k, \delta(T))} \tanh\frac{\varepsilon(k, \delta(T))}{2T}, \qquad \varepsilon(k, \delta) = 2\sqrt{\cos^2 k + \delta^2 \sin^2 k}. \tag{4.3}$$

The stiffness is half as large for spinless fermions, which corresponds to the XY spin-1/2 chain. The band gap opens as $2\varepsilon(\pi/2, \delta) = 4\delta$ and $\delta(0)$ goes as $\exp(-1/\varepsilon_d)$ in the weak coupling limit. The spinless fermion representation of the HAF has interactions between first neighbors. The HAF is correlated. Although not exact, the HAF gap opens [134] as $\delta^{3/4}$ based on diverse numerical studies collected in Ref. 112. The DMRG exponent in the range $0.001 \le \delta \le 0.10$ is [93] 0.7475 ± 0.0075.

To illustrate correlations and frustration, we show in Fig. 4.1 the dimerization of spin chains with $T_{SP} = 0.09$ (or $0.09J_1$). The fermion curve is Eq. 4.3 with $4/\pi$ instead of $8/\pi$; the band gap $4\delta(0) = 3.55T_{SP}$ is

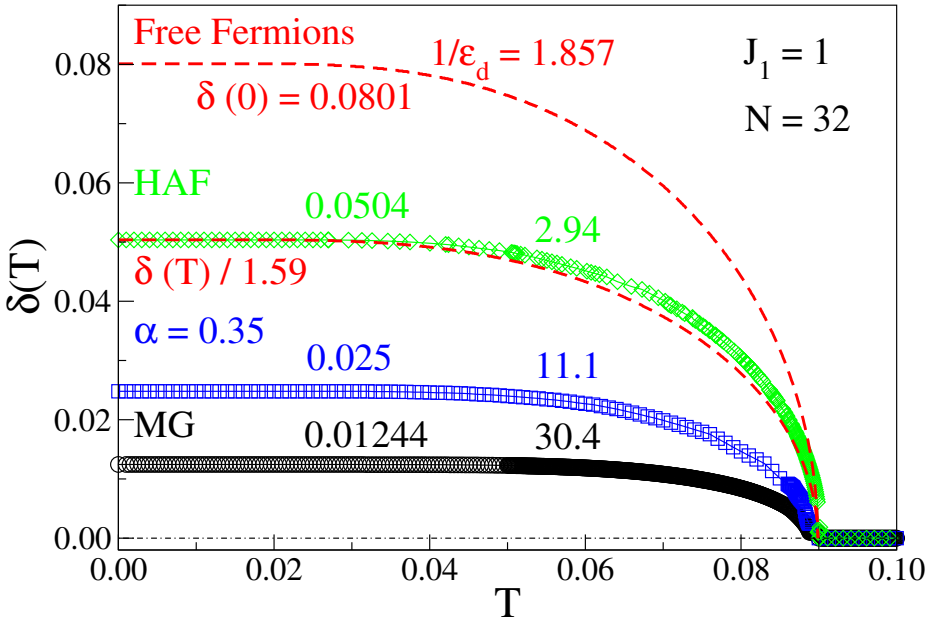

Figure 4.1: Equilibrium dimerization $\delta(T)$ of spin chains with $T_{SP} = 0.09$ leading to stiffness $1/\varepsilon_d$ and $\delta(0)$ in Eq. 4.2. The exact free fermion curve is Eq. 4.3 with $4/\pi$ instead of $8/\pi$. The HAF ($\alpha = 0$), $\alpha = 0.35$ and MG ($\alpha = 0.50$) curves are based on Eq. 4.4 with $N = 32$ spins. The HAF dimerization is close to the fermion $\delta(T)/1.59$. Note the large variation of $1/\varepsilon_d$ and $\delta(0)$ in chains with equal T_{SP}.

within 1% of the BCS gap relation. The other curves are $A'(T, \delta, N)$ for $J_1 - J_2$ models with $N = 32$ in Eq. 4.4, periodic boundary conditions and $\alpha = 0$ (HAF), 0.35 and 0.50 (MG). The fermion $\delta(T)$ scaled by $1/1.59$ is the dashed line through the HAF points; the scaled T dependence is nearly BCS. The stiffness increases by an order of magnitude from the HAF to MG while $\delta(0)$ decreases by a factor of four and $\delta(T)$ clearly deviates from free fermions.

We analyze SP transitions of the $J_1 - J_2$ model with frustration $0 \leq \alpha \leq 0.50$. Under some conditions, numerical advances have made accessible the thermodynamic limit of correlated states of 1D systems. The influential but approximate HAF analysis [2, 3] of TTF-$CuS_4C_4(CF_3)_4$ was widely thought to apply to the larger data set made possible by sizeable $CuGeO_3$ crystals. But $CuGeO_3$ turned out to be different and has largely resisted modeling. Correlated states provide a consistent description of both SP transitions.

The Chapter is organized as follows. Section 4.2 presents the calculation of $A'(T, \delta)$ in $J_1 - J_2$ models with frustration α and the criterion for the thermodynamic limit. We model in Section 4.3 the magnetic susceptibility $\chi(T, T_{SP})$ of TTF-$CuS_4C_4(CF_3)_4$ with two parameters, $J_1 = 79$ K and $T_{SP} = 12$ K. The $CuGeO_3$ parameters $J_1 = 160$ K, $\alpha = 0.35$ and $T_{SP} = 14$ K account for both $\chi(T, T_{SP})$ and the specific heat anomaly, $C(T, T_{SP})$. In Section 4.4 we discuss the $CuGeO_3$ excitations probed by inelastic

neutron scattering, not modeled previously, that give an independent determination of J_1. We also study the Majumdar-Ghosh (MG) point [31], $\alpha = 0.50$, where the exact ground state is known. Bond-bond correlation functions are used in Section 4.5 to discuss electronic dimerization $\delta_e(T, \alpha)$ in rigid regular chains with BOW ground states. The magnetic susceptibility $\chi(T, \alpha, T_{SP})$ is modeled in chains with variable frustration α. The possible realization of BOW systems is discussed qualitatively using the different T dependencies of $\delta(T, \alpha)$ and $\delta_e(T, \alpha)$.

4.2 Dimerized $J_1 - J_2$ model

The $J_1 - J_2$ model is discussed in Eq. 1.7. It has isotropic exchange interactions $J_1, J_2 = \alpha J_1$ between first and second neighbors of a regular ($\delta = 0$) spin-1/2 chain. The dimerized model has alternating $J_1(1 \pm \delta)$ along the chain. We consider finite chains with $N = 4n$ spins, periodic boundary conditions and $J_1 = 1$ as the unit of energy. The electronic Hamiltonian is

$$H(\delta, \alpha) = \sum_r (1 + \delta(-1)^r)\, \vec{S}_r \cdot \vec{S}_{r+1} + \alpha \sum_r \vec{S}_r \cdot \vec{S}_{r+2}. \tag{4.4}$$

Finite δ breaks inversion symmetry at sites and increases the singlet-triplet gap $\Delta(\delta, \alpha)$ but does not change the length in systems with periodic boundary conditions. The analysis does not depend on the index α which is suppressed below.

We consider the equilibrium Eq. 4.2 with increasing system size to obtain the thermodynamic limit at finite T and then evaluate $\delta(T)$ in models with $T_{SP} > T$. The free energy per spin of finite chains is

$$A(T, \delta, N) = -TN^{-1} \ln Q(T, \delta, N). \tag{4.5}$$

The Boltzmann sum in $Q(T, \delta, N)$ is over the 2^N spin states with energies $E_r(\delta, N)$. Exact diagonalization (ED) yields the full spectrum of short chains. The equilibrium dimerization requires the partial derivative that we approximate as

$$A'(T, \delta, N) \approx \frac{A(T, \delta + \varepsilon, N) - A(T, \delta - \varepsilon, N)}{2\varepsilon}. \tag{4.6}$$

The numerator is accurate to three decimal places for $\varepsilon = 0.001$. We find that the size dependence of A'

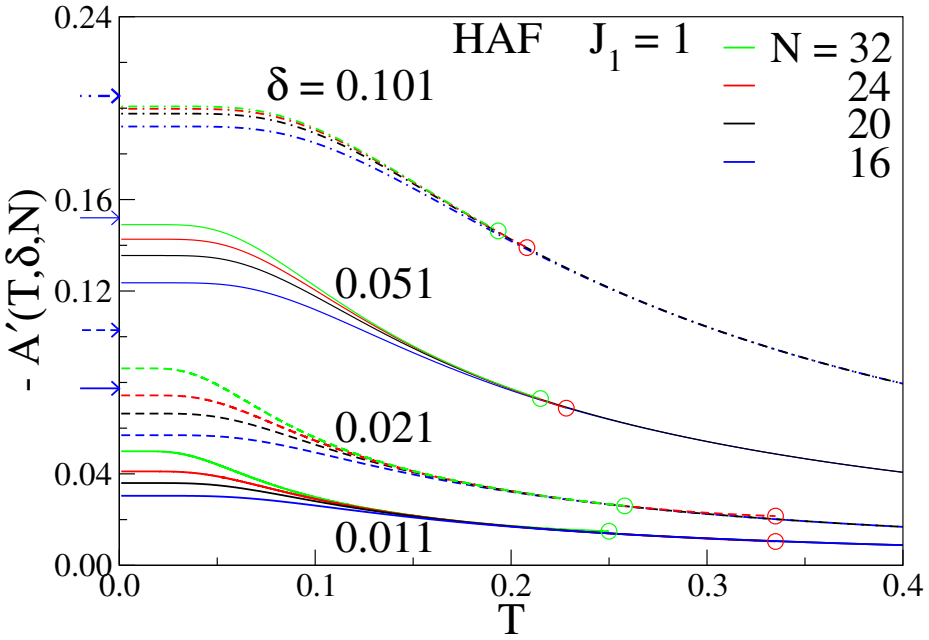

Figure 4.2: Driving force for dimerization, $-A'(T, \delta, N)$, of HAF chains with N spins and $\alpha = 0$ in Eq. 4.4. $N = 16$ and 20 are exact. DMRG for $N = 24$ and 32 is shown up to $T'(\delta, N)$, shown as open circles, the maximum of $S_C(T, \delta, N)/T$ discussed in the text. Arrows at $T = 0$ are thermodynamic limits that increase with δ.

is considerably weaker than that of A, presumably due to cancellations in the numerator.

The hybrid ED/DMRG method [81] follows the size dependence of the quantity of interest, here the driving force $-A'(T, \delta, N)$. Since T reduces the range of spin correlations, ED up to $N = 24$ for $\delta = 0$ or $N = 20$ for $\delta > 0$ returns the thermodynamic limit at high T. DMRG with periodic boundary conditions [107] is then used to obtain the lowest few thousand states of larger systems. The spectrum $E_r(\delta, N) \leq E_C(\delta, N)$ up to a cutoff defines a truncated partition function $Q_C(T, \delta, N)$ and hence a truncated entropy per site, $S_C(T, \delta, N)$. Finite size gaps reduce $S_C(T, \delta, N)$ compared to the actual entropy at low T while truncation reduces it at high T. Since $S_C(T, \delta, N)/T$ converges from below with increasing N, its maximum at $T'(\delta, N)$ is the best choice for a given cutoff $E_C(\delta, N)$. The cutoff is increased until $T'(\delta, N)$ is independent or almost independent of E_C. The thermodynamic limit of $A'(T', \delta)$ at $T'(\delta, N)$ is approximated by DMRG at system size N.

Fig. 4.2 illustrates the T dependence of $-A'(T, \delta, N)$ of the HAF. As expected for any α, $-A'$ decreases with T and increases N to the thermodynamic limit. The $N = 16$ and 20 lines are exact. DMRG results for $N > 20$ extend to the points $T'(\delta, N)$, the maxima of $S_C(T, \delta, N)/T$ that are shown as open circles. Finite size gaps are evident around $T \sim \delta \sim 0$ where $-A'(T, \delta, N)$ is constant. Arrows indicate the

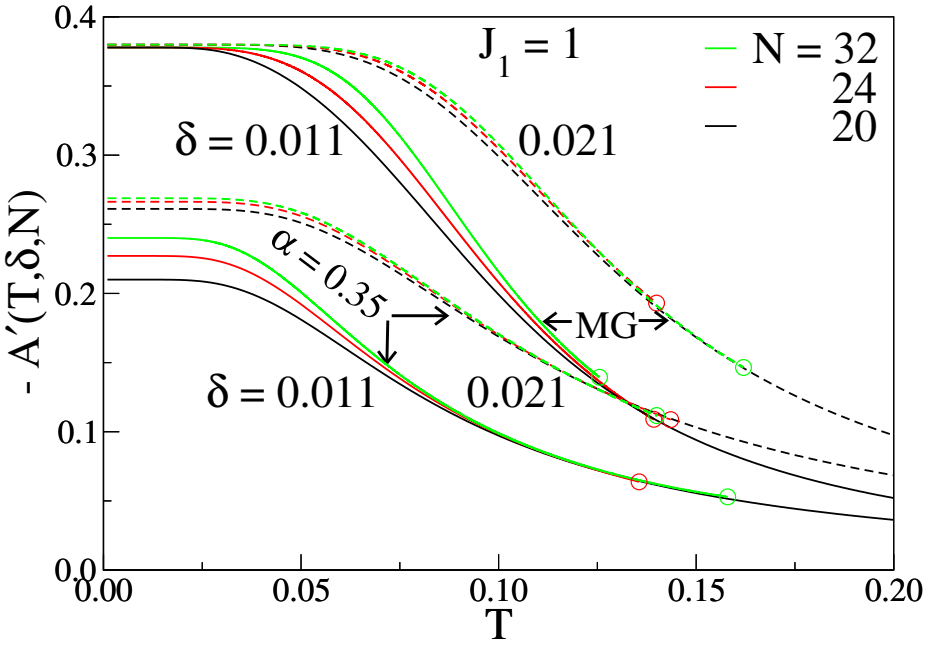

Figure 4.3: Same as Fig. 4.2 for frustration $\alpha = 0.35$ and MG ($\alpha = 0.50$) in Eq. 4.4.

$T = 0$ intercepts, $-E_0'(\delta, N)$, that are obtained by extrapolation of ground-state DMRG calculations [93] at constant δ. Since δ opens a magnetic gap in the infinite chain, the size dependence decreases as seen at $\delta = 0.101$. Convergence to the thermodynamic limit is found by $T \sim 0.15$, The general criterion based on $T'(\delta, N)$ is evidently conservative for $A'(T, \delta, N)$, which is seen to converge at lower T.

The size dependence of $A'(T, \delta, N)$ in the dimer phase is shown in Fig. 4.3 for $\alpha = 0.35$ and 0.50 in Eq. 4.4. The MG ground states are the two Kekulé VB diagrams with singlet pairing either between all sites $2r, 2r-1$ or all sites $2r, 2r+1$. The energy per site is $-3/8$ for even N in Eq. 4.4 and $A'(0, \delta, N) = -3/8$ is exact [135] to order δ. The thermodynamic limit is reached by $T \sim 0.13$ for $\alpha = 0.50$. The size dependence at $\alpha = 0.35$ is intermediate. The ground state is degenerate in the thermodynamic limit but not for finite N. The $-A'(0, 0, N)$ intercept decreases with N to $B(0.35) = 0.078$ in the thermodynamic limit, where $B(\alpha)$ is the amplitude of the bond order wave [52]. The size dependence again decreases with δ.

Fig. 4.2 and Fig. 4.3 indicate how $A'(T, \delta, N)$ approaches the thermodynamic limit. The convergence depends on the model and the largest system N_m,

$$A'(T, \delta, N_m) \to A'(T, \delta), \qquad T > T'(\delta, N_m). \tag{4.7}$$

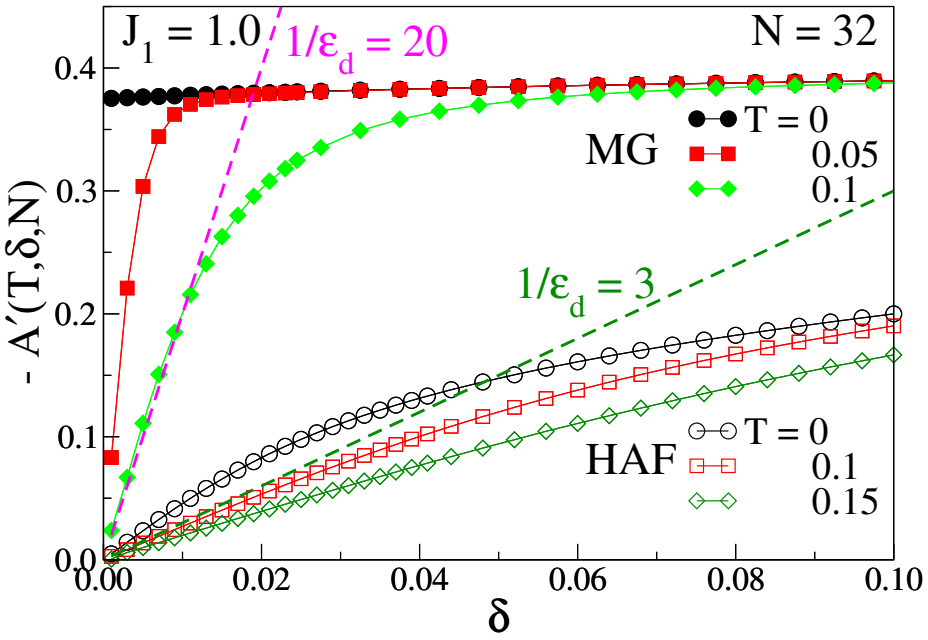

Figure 4.4: The driving force $-A'(T, \delta, N)$ at reduced T of MG and HAF chains with $N = 32$ and $\alpha = 0.50$ and 0 in Eq. 4.4. The dashed lines are δ/ε_d and crossing points are solutions $\delta(T)$ to Eq. 4.2. The HAF and MG curves are lower and upper bounds for frustration $0 \leq \alpha \leq 0.50$.

$T'(\delta, N_m)$ is the maximum of $S_C(\delta, T, N_m)/T$ of the largest system considered. We have performed DMRG calculations up to $N \sim 100$, but smaller N may be sufficient and convergence at $\delta = 0$ typically also holds for $\delta > 0$. The system size is eventually limited [81] by the numerical accuracy of the dense energy spectrum, which is of course model dependent. Although the mathematically interesting $A'(T, 0)$ at $T \sim 0$ is out of reach, modeling SP transitions merely requires $T_{SP} > T'(0, N_m)$. The equilibrium Eq. 4.2 then gives $\delta(T)$ in the thermodynamic limit.

Fig. 4.4 shows $A'(T, \delta, N)$ vs. δ for models with $N = 32$ and $\alpha = 0$ (HAF) or 0.50 (MG). These curves lower and upper bounds of $-A'(T, \delta, N)$ for $J_1 - J_2$ models with $0 \leq \alpha \leq 0.50$. The $\delta = 0$ intercept at $T = 0$ decreases from 3/8 at $\alpha = 0.50$ to zero at $\alpha_c = 0.2411$ where [93, 136] $E_0'(\delta) = -0.62\delta^{0.33}$. The HAF result [93] is $E_0'(\delta) = 0.56\delta^{0.44}$. The graphical solutions $\delta(T, \alpha)$ of Eq. 4.2 are the intersections in Fig. 4.4 of $A'(T, \delta, N)$ with dashed lines δ/ε_d at the indicated stiffness. The chains are unconditionally unstable for finite ε_d since $E_0'(\delta)$ is finite at $\delta = 0$ for $\alpha > \alpha_c$ while $E_0''(\delta)$ diverges at $\delta = 0$ for $\alpha < \alpha_c$. The $E_0'(\delta)$ cusp at $\delta = 0$ in the dimer phase leads to the flatter two $\delta(T)$ curves [135] in Fig. 4.1.

We conclude that the thermodynamic limit $A'(T, \delta)$ can be reached in finite chains at $T = 0$ when $\delta > 0$ or at $\delta = 0$ when $T > 0$. The $T > T_{SP}$ range is more accessible numerically for large T_{SP}/J_1 that

in turn generates large $\delta(0)$. The relation between T_{SP} and $\delta(0)$ is strongly model dependent as seen in Fig.4.1.

4.3 Magnetic susceptibility and specific heat

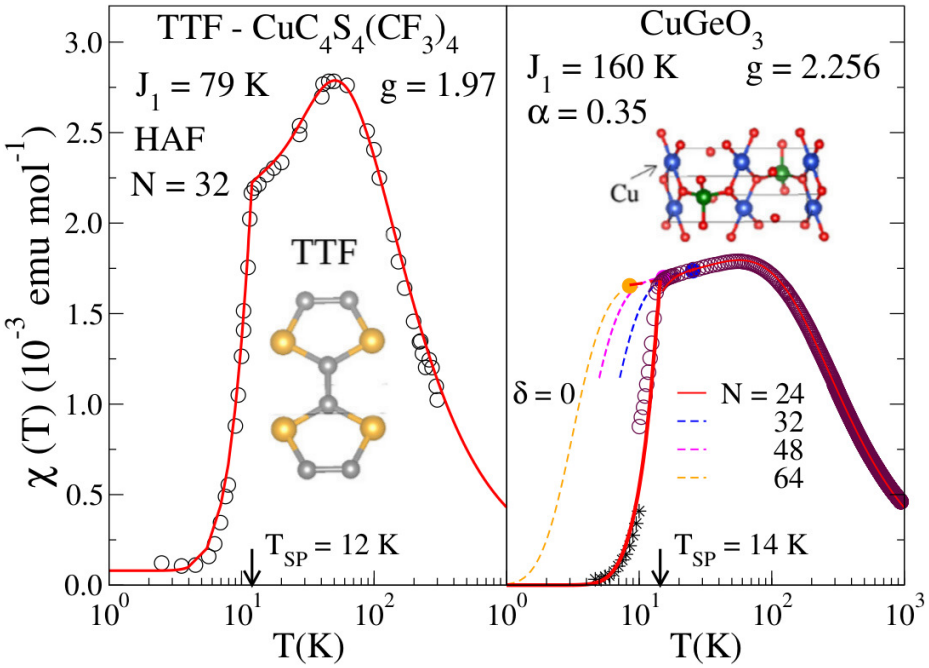

Figure 4.5: Absolute molar magnetic susceptibility: TTF-$CuS_4C_4(CF_3)_4$ data from Fig. 5 of Ref. 2 or Fig. 10 of Ref. 3; $CuGeO_3$ data from Ref. 4, 5 to 10 K and Ref. 6 for $T > 10$ K. Fits are discussed in the text. The $\delta = 0$ lines are DMRG up to $T'(0, N)$ shown as filled circles.

A sudden decrease of the molar magnetic susceptibility $\chi(T)$ at $T < T_{SP}$ is a direct manifestation of an SP transition. Fig. 4.5 shows published data for [2] TTF-$CuS_4C_4(CF_3)_4$ and [4, 6] $CuGeO_3$ on a log scale that emphasizes low T. The excellent TTF^+ fit shown in Fig. 4.5 of Ref. 2 or Fig. 10 of Ref. 3 is based on the HAF with $J_1 = 77$ K and $g = 1.97$ for $T > T_{SP} = 12$ K. The g value is within the range given by electron spin resonance (esr) with the applied magnetic field along the c axis. The $T \sim 0$ limit is shown as slightly positive ($\sim 0.08 \times 10^{-3}$ emu/mol).

We included this T-independent contribution in the correlated fit shown with $J_1 = 79$ K, $T_{SP} = 12$ K and $g = 1.97$. The $\delta = 0$ curve above T_{SP} is ED for $N = 24$ and DMRG for $N = 32$ with $\alpha = 0$ in Eq. 4.4. In the dimerized phase, we calculated $\chi(T, T_{SP})$ for $N = 32$ at the equilibrium $\delta(T)$ given by Eq. 4.2. The correlated fit is equally quantitative. It has one fewer parameter and is internally consistent: T_{SP} and J_1 determine both the stiffness $1/\varepsilon_d = 1.96$ and $\delta(0) = 0.103$. The previous $\chi(T, \delta(T))$ was

based [2] on a mean field $\delta(T)$ for the T dependence and required an adjustable $\delta(0) = 0.126$ that, as noted, [2] leads to $T_{SP} = 9$ rather than 12 K.

The range of spin correlations is reduced at low T by substantial dimerization $\delta(0) = 0.10$. The thermodynamic limit is reached in relatively short chains that are now amenable to quantitative analysis. Correlated states clarify the SP transition of TTF-$CuS_4C_4(CF_3)_4$. Contrary to long held expectations, the HAF dimerization $\delta(T)$ does *not* follow free fermions or BCS.

The $\chi(T)$ data for $CuGeO_3$ are from Ref. 4, 5 up to 10 K ($T_{SP} = 14$ K) and from Ref. 6 from 10 to 950 K ($T_{SP} = 14.3$ K), kindly provided in digital form by Professor Lorenz. There is a mismatch at 10 K. The range (~ 0.5 K) of reported T_{SP} reflect variations of growth conditions that are discussed in Ref. 137. We retained the previous parameters [6] based on ED for $N = 18$ and the $\chi(T)$ maximum at $T = 56$ K: $J_1 = 160$ K, frustration $\alpha = 0.35$ in Eq. 4.4, $g = 2.256$ from esr. The $\delta = 0$ fit is quantitative for $T > T_{SP} = 14$ K ($0.09J_1$). The points $T'(N)$ on the $\delta = 0$ curve are the $S_C(T, 0, N)/T$ maxima of truncated calculations at system size N. The resulting $\chi(T, T_{SP})$ for $T < T_{SP}$ is consistent with the available data and corresponds to $\delta(0) = 0.025$. We extend [6] or improve [138, 139] previous $T > T_{SP}$ fits.

Sizeable single crystals of $CuGeO_3$ made possible other measurements. The specific heat $C(T)$ to 20 K is shown in Fig. 4.6 as the entropy derivative $S' = C/T$ in Refs. 7, 8. The dashed line is the reported lattice (Debye) contribution [8], AT^2, with $A = 0.32$ mJ/mol K^4. The specific heat has not been modeled aside from the initial exponential increase with T. The anomaly is sharper and better resolved than in small TTF-$CuS_4C_4(CF_3)_4$ crystals [140].

The equilibrium $C(T, T_{SP})$ has two contributions [135] below T_{SP},

$$C(T, T_{SP}) = C(T, \delta(T)) + \frac{\partial \delta}{\partial T}\left[\left(\frac{\partial E(T, \delta)}{\partial \delta}\right)_T + \frac{\delta(T)}{\varepsilon_d}\right]. \tag{4.8}$$

$E(T, \delta)$ is the internal energy per site, $-(\partial \ln Q(\beta, \delta)/\partial\beta)$ with $\beta = 1/k_B T$. The first term is evaluated at $\delta(T)$ along the equilibrium $\alpha = 0.35$ line in Fig. 1, which can be fit quantitatively as

$$\frac{\delta(T)}{\delta(0)} = \left(1 - \left(\frac{T}{T_{SP}}\right)^a\right)^b, \qquad T \le T_{SP} \tag{4.9}$$

with $a = 5.29$ and $b = 0.689$. We used Eq. 4.9 to evaluate $\partial\delta/\partial T$. The calculated $C(T, T_{SP})/T$ is the

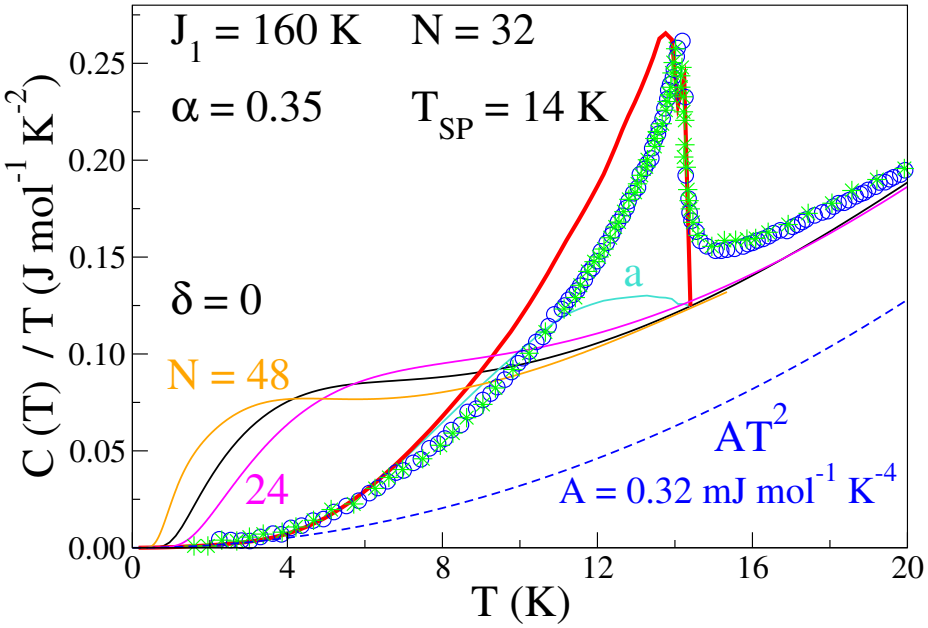

Figure 4.6: Molar specific heat $C(T)$ of $CuGeO_3$ shown as the entropy derivative $S' = C/T$: blue circles from Ref. 7, green stars and A from Ref. 8. The calculated $C(T,0)/T$ curves are ED for $N = 24$, DMRG for $N = 32$ and 48. The equilibrium $C(T, T_{SP})/T$ is the bold red line, Eq. 4.8, whose first term is labeled (a).

bold red line shown in Fig. 4.6. The low-T behavior of $\delta = 0$ chains is a finite size effect. Since gaps initially decrease $C(T,N)/T$, entropy conservation requires increased $C(T,N)/T$ before converging from above to the thermodynamic limit. The $N = 48$ and 24 gaps are smaller and larger, respectively, than $N = 32$, which is in the thermodynamic limit for $T > 12$ K.

The $C(T, \delta(T))/T$ part of Eq. 4.8 is the curve labeled (a) in Fig. 4.6. The $\partial\delta(T)/\delta T$ derivative is mainly responsible for the sharp anomaly. The area under $C(T, T_{SP})/T$ up to T_{SP} is within 5% of the accurately known $\delta = 0$ area. The adiabatic and mean field approximations for the lattice enforce $\delta = 0$ for $T > T_{SP}$; this general problem for any transition has long been recognized. The agreement between theory and experiment by 20 K implies equal area under the measured, dimerized and $\delta = 0$ curves in Fig. 4.6. Lattice fluctuations observed above T_{SP} must be offset by reduced C/T below T_{SP}. Overall, the anomaly is fit rather well considering these approximations.

4.4 Inelastic neutron scattering

Dimerization opens a gap $\Delta(\delta, \alpha)$ in gapless spin chains or increases the gap in gapped chains. The gap is from the singlet ($S = 0$) ground state to the lowest energy triplet ($S = 1$). The opening of the HAF

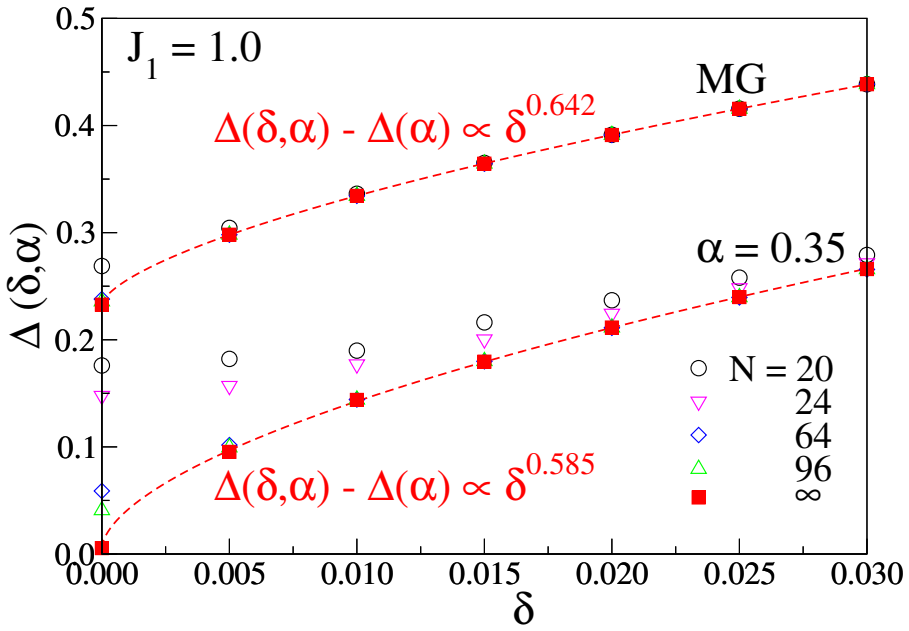

Figure 4.7: Scaled singlet-triplet gap $\Delta(T, \delta, N)$ at $T = 0$ of N-spin chains in Eq. 4.4 with dimerization δ and frustration $\alpha = 0.35$ and 0.50. The lines are $1/N$ extrapolations of DMRG to $N = 96$. Note the rapid convergence at the MG point.

gap [112, 134] $\Delta(\delta, 0)$ or of $\Delta(\delta, \alpha_c)$ at the critical point [93, 136] has been extensively discussed using field theory and numerical methods; $\Delta(0, \alpha)$ is finite in the dimer phase, exponentially small just above α_c and substantial at $\alpha = 0.50$. We obtained the thermodynamic limit of $T = 0$ gaps in Fig. 4.7 by extrapolation of DMRG calculations up to $N = 96$. As expected, size convergence is rapid for $\delta > 0.01$. The gap opens as

$$\Delta(\delta, \alpha) = \Delta(\alpha) + D\delta^{\gamma}, \tag{4.10}$$

with $\Delta = 0.0053$, $D = 2.03$ and $\gamma = 0.585$ for $\alpha = 0.35$. The T dependence is given by $\delta(T)$. The large MG gap is $\Delta(0, 0.5) = 0.233$.

Inelastic neutron scattering (INS) at $T = 0$ is exclusively to triplets in models with isotropic exchange. Fig. 4.8 shows the scaled gap $\Delta(T)/\Delta(0)$ vs. T/T_{SP}. The solid line is the calculated $\Delta(\delta(T), 0.35)$ in Eq. 4.10 with $\delta(T)$ in Eq. 4.9 or the $\alpha = 0.35$ curve in Fig. 4.1. The gap $\Delta J_1 = 0.85$ K is almost an order of magnitude below INS resolution and scales to 0.022 for $T > T_{SP}$ and $\delta(0) = 0.025$. The dashed line is the gap ratio $\delta(T)/\delta(0)$ for free fermions in Fig. 4.1. INS studies of $CuGeO_3$ crystals in Refs. [9–12] have reported the T dependence of the singlet-triplet gap $\Delta(T)$. (The organic crystals are unsuitably small [12].) Large deviations from the free fermions or BCS were unexpected and unexplained. Correlated states are

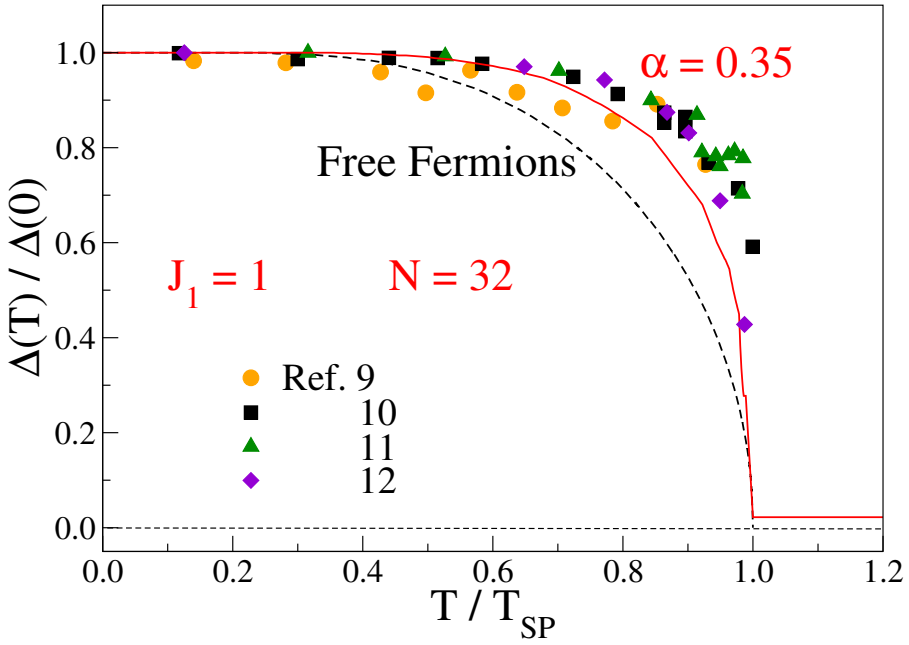

Figure 4.8: Scaled singlet-triplet gap $\Delta(T)/\Delta(0)$ vs. T/T_{SP}. The solid line is $\Delta(\delta(T),\alpha)/\Delta(\delta(0),\alpha)$ with $\alpha = 0.35$ in Eq. 4.10; the dashed line is $\delta(T)/\delta(0)$ for free fermions in Fig 4.1. The symbols are inelastic neutron data from Refs. 9–12.

consistent with these data, and how quantitatively remains to be seen.

The calculation of the INS spectrum is straightforward in finite systems with periodic boundary conditions. Triplets $|T_n(q)\rangle$ at $E_n(q)$ relative to the singlet ground state $|G\rangle$ are required. At $T = 0$, the INS intensity $M_n(q)$ for energy transfer $\omega = E_n(q)$ and momentum transfer q is [141]

$$\begin{aligned} M_n(q) &= 2\pi|\langle T_n(q)|S^x_q|G\rangle|^2, \\ S^x_q &= (4n)^{-\frac{1}{2}}\sum_r e^{iqr}S^x_r. \end{aligned} \tag{4.11}$$

The x or y components of S_q also yield $M_n(q)$. The lowest triplet of $H(\delta,\alpha)$ is $E_1(\pi) = \Delta(\delta,\alpha)$ The INS intensity at finite T is the thermal average [141] of Eq. 4.11 over excited states as well as $|G\rangle$. The static structure factor at $T = 0$ is given by ground-state spin correlation functions

$$S(q) = \langle G|S^x_{-q}S^x_q|G\rangle. \tag{4.12}$$

The total INS intensity per spin is $\pi/2$ for chains with a singlet ground state. The thermal average of $S(T,q)$ in Eq. 4.12 is far less tedious since it only requires the T dependence of $N/2$ correlation functions.

The Bethe ansatz [110, 111] has provided the exact ground state of the HAF and the so-called Class C states with $S > 0$ that can be solved exactly. Faddeev and Takhtajan [142] obtained the double spinon continuum in the thermodynamic limits. The lower and upper boundaries at wave vector q are

$$\begin{aligned} \varepsilon_1(q) &= \frac{\pi}{2}\sin q; \\ \varepsilon_2(q) &= \pi \sin\frac{q}{2}. \qquad 0 \le q \le \pi \end{aligned} \tag{4.13}$$

Each state is four-fold degenerate, two $S = 1/2$ spinons forming a triplet or a singlet. The boundaries up to $q = \pi$ are the dashed lines in the HAF panel of Fig. 4.9. The spectrum is symmetric about $q = \pi$. The singlet-triplet gap $\varepsilon_1(q)$ was found earlier by des Cloizeaux and Pearson [143].

The almost quantitative calculation of intensities $M_n(q)$ in the thermodynamic limit has recently been achieved [144]. Mourigal et al. [145] have confirmed theory in detail on a Cu(II) spin chain with $J_1 = 2.93$ K; the INS analysis in Fig. 1 of Ref. 145 was carried out at finite T using both two and four-spinon calculations. $S(q,\omega)$ is continuous in the thermodynamic limit. Fig. 1 is color coded according to intensity and impressive agreement between theory and experiment is shown, as in Fig. 4.9, side by side with $0 \le q \le \pi$ and $\pi \le q \le 2\pi$.

When total spin is conserved, a system of $N = 4n$ spins has $3(4n)!/[(2n-1)!(2n+2)!]$ triplets out of which only $n(2n+1)$ are in Class C [110, 111] and have excitation energy between $\varepsilon_2(q)$ and $\varepsilon_1(q)$ in the thermodynamic limit. The $S(q,\omega)$ spectra in the HAF panel of Fig. 4.9 are $\alpha = \delta = 0$ and $N = 24$. The color coding is according to the intensity $M_n(q) > 0.001$. There are a few triplets not in Class C, but 99.4% of the total intensity is between the dashed lines. The discrete $S(q,\omega)$ spectra are close to the thermodynamic limit for both excitations and intensities.

The $S(q,\omega)$ spectra in the $\alpha = 0.35$ panel of Fig. 4.9 are for $\delta = 0, N = 24$ and color coded according to $M_n(q) > 0.001$. ED returns the full spectrum. The special feature of the triplets shown is greater intensity than over 500,000 other triplets. The triplets account for 99.5% of the total intensity and, again with a few outliers, resemble the spinons in the left panel.

Frustration decreases the dispersion $E_1(q)$ of the lowest triplet, as shown by open circles in the MG ($\alpha = 0.50$) curve. The HAF triplets $E_1(q,N)$ are slightly above $\varepsilon_1(q)$, which at $q = \pi$ is entirely due to finite size. The $q = \pi, \alpha = 0.35$ gap is mainly due to finite size while the $\alpha = 0.50$ gap is close

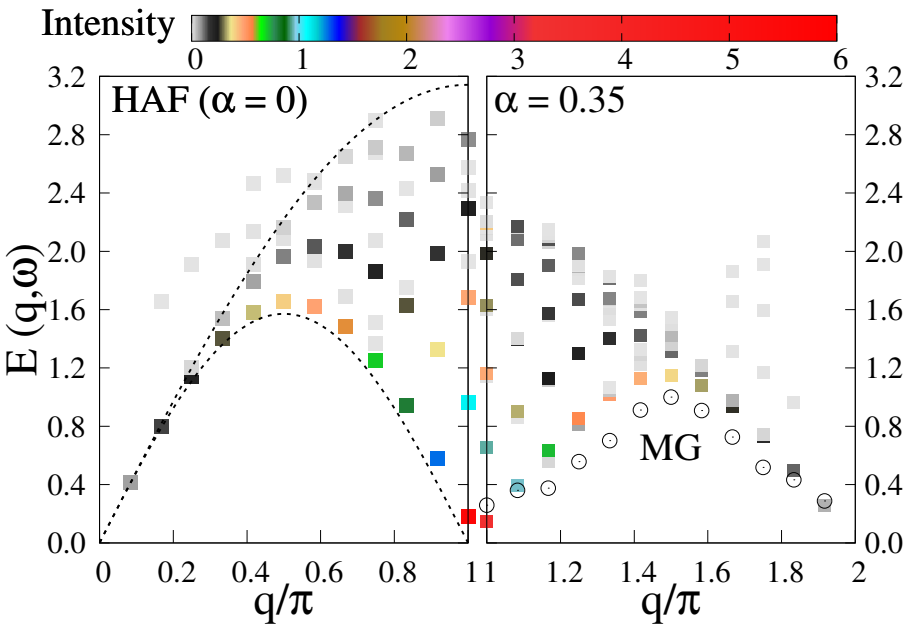

Figure 4.9: Exact triplet excitations $E_n(q)$ at wave vector q in 24-spin chains: left panel, $\alpha = 0$ (HAF); right panel, $\alpha = 0.35$. The color coding is the intensity $M_n(q) > 0.001$ in Eq. 4.11. The lowest triplets $E_1(q)$ for $\alpha = 0.50$ (MG) are the open circles on the right. The dashed lines are the spinon boundaries, Eq. 4.13.

the thermodynamic limit of 0.233 in Fig. 4.7. The HAF dispersion has previously been used to infer $J_1 = 2E_1/\pi$ from the measured $E_1(\pi/2)$.

Arai et al. [13] reported the $S(q,\omega)$ spectrum of $CuGeO_3$ and interpreted it using the HAF while also pointing out differences. At 10 K, the observed $S(q,\omega)$ intensity peaks at $\pi/2$ and $3\pi/2$ are at 16 meV (186 K). The peaks for $\alpha = 0.35$, $N = 24$ in Fig. 4.9 are at reduced energy $E_1(\pi/2) = 1.14$, or $E_1 = 182$ K for $J_1 = 160$ K. The agreement is well within the combined accuracy. The $N = 16$, 20 and 24 gaps extrapolated as $1/N$ return $E_1 = 1.1$ in the thermodynamic limit. The weak size dependence is typical of large gaps. The upper limit of the INS spectrum extends [13] to 32 meV at $q = \pi$ at both 10 and 50 K. The calculated $T = 0$ spectrum with appreciable $M_n(\pi)$ also extends to $\omega \sim 2E_1(\pi/2) = 2.28$.

The calculations in Fig. 4.9 approximate the unknown $S(q,\omega)$ at $\alpha = 0.35$ in the same sense that $N = 24$ approximates the HAF spectrum. $S(q,\omega)$ at $q = \pi/2$ or $3\pi/2$ of $CuGeO_3$ has a noticeably narrower [13] energy spread than the spinon spread $\varepsilon_2(\pi/2) - \varepsilon_1(\pi/2)$. The correlated states in Fig. 4.9 capture this narrowing at $\alpha = 0.35$ compared to $\alpha = 0$. Indeed, the width is entirely suppressed at $\alpha = 0.50$ where INS at $q = \pi/2$ or $3\pi/2$ is a δ-function at $E = J_1$. This exact result for a triplet, not reported previously, is derived in the Appendix.

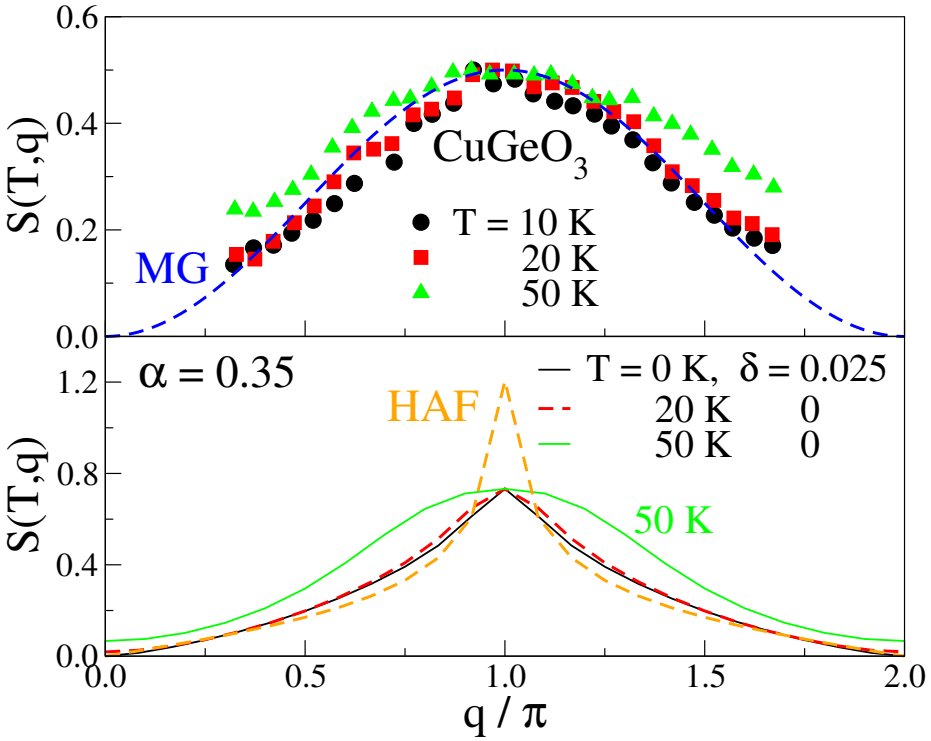

Figure 4.10: Upper panel: Static structure factor $S(T,q)$ rescaled from Fig. 2 of Ref. 13. The exact $S(q)$ at the MG point is $(1-\cos q)/4$ at $T=0$. Lower panel: Calculated $S(T,q)$ for $N=24$ spins at $\alpha=0.35$ and 0.0. The area under $T=0$ curves is $\pi/2$ in both panels. The HAF peak at $q=\pi$ diverges in the thermodynamic limit.

The INS data in Fig. 4.10, upper panel, for the static structure factor $S(T,q)$ of $CuGeO_3$ is rescaled Fig. 2 of Ref. 13. Large differences from HAF were noted [13]. The dashed line is the exact $S(q) = (1-\cos q)/4$ at $T=\delta=0, \alpha=0.50$, where finite size simply leads to discrete q. Although $S(q)$ depends on α and δ the area $\pi/2$ under $S(q)$ does not. The 10 K data are almost as broad as the MG curve before considering the resolution in q.

The calculated $S(T,q)$ in the lower panel of Fig. 4.10 are for the HAF and for $CuGeO_3$ parameters: $J_1 = 160$ K, $\alpha = 0.35$ and $T_{SP} = 14$ K. The HAF structure factor for $N=24$, $\delta=0$ is strongly peaked at $q=\pi$ and diverges in the thermodynamic limit, but the size dependence elsewhere is small since the area is conserved [49]. The $\alpha=0.35$ curves at $T=0$ and 20 K (0.125) are for $N=24$ and $\delta=0.025$ and 0, respectively. We obtained explicitly the T dependence of the spin correlation functions in $S(q)$. The $T=0$ and 20 K curves illustrate similar spin correlations at $\delta>0$, $T=0$ and $T>0$, $\delta=0$, as seen in experiment. Convolution with a broadening function in q will be needed to match the observed peaks that depend on resolution in q. The $T=50$ K (0.313) line is based on $\delta=0, N=20$ since the thermodynamic limit is reached at lower T. We understand the modest broadening at 50 K by noting that

$J_1 = 160$ K is large. We conclude that a 1D model with correlated states accounts reasonably well for these INS data.

4.5 Bond-bond correlation functions

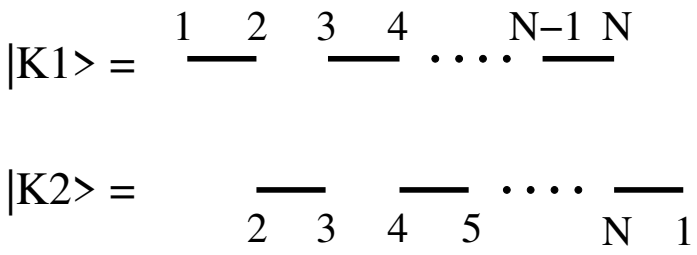

Figure 4.11: Kekulé valence bond diagrams. Lines indicate singlet-paired spins in Eq. 4.14.

We have modeled the best characterized SP systems, the organic crystal [2] TTF-$CuS_4C_4(CF_3)_4$ with $\alpha = 0$ and the inorganic crystal $CuGeO_3$ with $\alpha = 0.35$. Next We focus on the $J_1 - J_2$ model in Eq. 4.4 with variable frustration $0 \leq \alpha \leq 3/4$ that includes both gapped and gapless phases. We distinguish between phase transitions with structural dimerization $\delta(T, \alpha)$ at $T < T_{SP}(\alpha)$ and quantum transitions with electronic dimerization $\delta_e(0, \alpha)$ for $\alpha > \alpha_c$ in a rigid lattice, and we obtain the T dependence of $\delta_e(T, \alpha)$ using bond-bond correlation functions.

The following special case contrasts electronic and structural dimerization. At the Majumdar-Ghosh (MG) point [31], $\alpha = 1/2$, the exact ground states for an even number of spins N are the Kekulé valence bond (VB) diagrams $|K1\rangle$ and $|K2\rangle$ sketched in Fig. 4.11. Each diagram is a product of $N/2$ singlet-paired spins shown as lines

$$(r, r+1) \quad = \left(\alpha_r \beta_{r+1} - \beta_r \alpha_{r+1}\right)/\sqrt{2}. \tag{4.14}$$

$|K1\rangle$ has odd r and paired spins $(1,2)(3,4)...(N-1,N)$ while $|K2\rangle$ has even r and paired spins $(2,3)(4,5)$ $...(1,N)$. Either diagram has perfectly ordered bonds. The linear combinations $|K1\rangle \pm |K2\rangle$ are even and odd, respectively, under inversion at sites and also have long-range bond-bond order.

The linear HAF has $\alpha = 0$ and $J_1(1 \pm \delta)$ at dimerization δ. The limits $\delta = \pm 1$ lead to $N/2$ two-level systems with singlet ground states $|K1\rangle$ and $|K2\rangle$ for odd and even r in Eq. 4.14. Since the *nondegenerate*

ground state of the $\delta = \pm 1, \alpha = 0$ chains have perfectly ordered bonds, just as do the *degenerate* ground states of the $\delta = 0, \alpha = 1/2$ chain, we conclude that $\delta_e = \pm 1$ at the MG point. Any observable associated with the electronic ground state must be identical. The energy spectrum is otherwise quite different. Bond-bond correlation functions generalize $\delta_e(\alpha)$ to frustration α in the ground state and then to $\delta_e(T, \alpha)$.

The ground state $|G, \alpha\rangle$ of the $J_1 - J_2$ model, Eq. 4.4, with $\delta = 0$, is nondegenerate in the gapless phase $\alpha \leq \alpha_c$. Since the degenerate ground states of the gapped phase are even and odd under inversion at sites, the symmetry adapted $|G, \alpha, \pm 1\rangle$ are also nondegenerate. Correlations between bonds $r, r+1$ and $r', r'+1$ then depend only on $p = r' - r$ and are described by four-spin correlation functions

$$C_4(p, \alpha) = \langle S^z_r S^z_{r+1} S^z_{r+p} S^z_{r+p+1} \rangle. \tag{4.15}$$

At the MG point, we evaluate $C_4(p, 1/2)$ for $(|K1\rangle \pm |K2\rangle)/\sqrt{2}$. Bonds separated by odd p are in different diagrams and return $C_4(p, 1/2) = 0$. When p is even, $C_4(p, 1/2)$ is $1/16$ or 0, respectively, for the diagram that contains both or neither bond. It follows that $32C_4(p, 1/2) = 1$ or 0 for even or odd p.

Spin-spin correlation functions also depend only on $p = r' - r$ in systems with periodic boundary conditions,

$$C_2(p, \alpha) = \langle S^z_r S^z_{r+p} \rangle. \tag{4.16}$$

Spin-spin correlations are critical in the gapless phase $\alpha \leq \alpha_c$ and have been extensively characterized [1, 146] for the HAF where $C_2(p, 0)$ goes as $(-1)^p (\ln p)^{1/2}/p$ for $p \gg 1$. The range is finite in gapped phases and is just nearest neighbors at the MG point. When distant bonds are uncorrelated, four-spin correlation functions factor as

$$C_4(p, \alpha) = C_2(1, \alpha)^2. \qquad (p \gg 1) \tag{4.17}$$

Since the exact $C_2(1, 0)$ is $-(\ln 2 - 1/4)/3$, the $p \to \infty$ limit is $32C_4(p, 0) = 0.698$ and is approached from below as p^{-2}.

We anticipate that bond-bond correlations are long ranged in gapped phases with electronic dimerization $\delta_e(\alpha)$. We combine Eq. 4.17 and $\delta_e(1/2) = 1$ for Kekulé diagrams to obtain correlations between

distant bonds at any frustration

$$C_4\,(p,\alpha) = C_2(1,\alpha)^2 + (-1)^p \delta_e\,(\alpha)/64. \quad (p \gg 1) \tag{4.18}$$

The difference between even and odd p, if any, is $\delta_e(\alpha)/32$.

We turn to the numerical analysis of finite chains of $N = 4n$ spins. Except at the MG point, the ground state is nondegenerate and there is small finite-size gap $E_\sigma(\alpha, N)$ to the singlet with the opposite inversion symmetry. We compute the correlation function of the most distant bonds, $p = 2n$, at frustration α in increasingly large $N = 4n$ chains

$$C_4(2n,\alpha) = \langle G(\alpha,4n)|S^x_1 S^x_2 S^x_{2n+1} S^x_{2n+2}|G(\alpha,4n)\rangle. \tag{4.19}$$

The next most distant bond has $p = 2n-1$ and correlation function $C_4(2n-1,\alpha)$. The difference is

$$D_4(2n,\alpha) = C_4(2n,\alpha) - C_4(2n-1,\alpha). \tag{4.20}$$

The size dependence is strong in the gapless phase and weak for $\alpha > 1/2$ due to large $\Delta(\alpha)$. Accordingly, we compute correlations to $N = 96$ for $\alpha = 0.35$ or less and to $N = 64$ otherwise.

Fig. 4.12 shows the size dependence of bond-bond correlations at $\alpha = 0$, α_c and 0.35. The solid line $A_4(2n,\alpha)$ in the upper panel is the arithmetic mean of $C_4(2n,\alpha)$ and $C_4(2n-1,\alpha)$ from $N = 24$ to 96; the dashed line is $C_2(1,\alpha,4n)^2$, the square of the nearest neighbor spin correlation function at system size $N = 4n$. They are equal within our numerical accuracy and go as N^{-2}. The extrapolated $\alpha = 0$ intercept agrees with the exact 2.182 based on Eq. 4.17. The lower panel shows $D_4(2n,\alpha)$ from $N = 24$ to 96. The size dependence at α_c is remarkably linear in $1/N$ as expected. The decrease is faster at $\alpha = 0$, again as expected, while $\alpha = 0.35$ in the gapped phase has finite $D_4 = 0.0036$ in the thermodynamic limit and electronic dimerization $\delta_e(0.35) = 0.115$ in Eq. 4.18. The $D_4(2n,\alpha)$ results confirm that long-range bond-bond correlations are finite in the dimer phase.

The upper panel of Fig. 4.13 shows bond-bond correlation functions at $0 \le \alpha \le 3/4$ with unit amplitude at the MG point. $C_4(2n,\alpha)$ correlations of bonds in the same Kekulé diagram decrease with system size while the $C_4(2n-1,\alpha)$ correlations of bonds in different diagrams increase. They converge

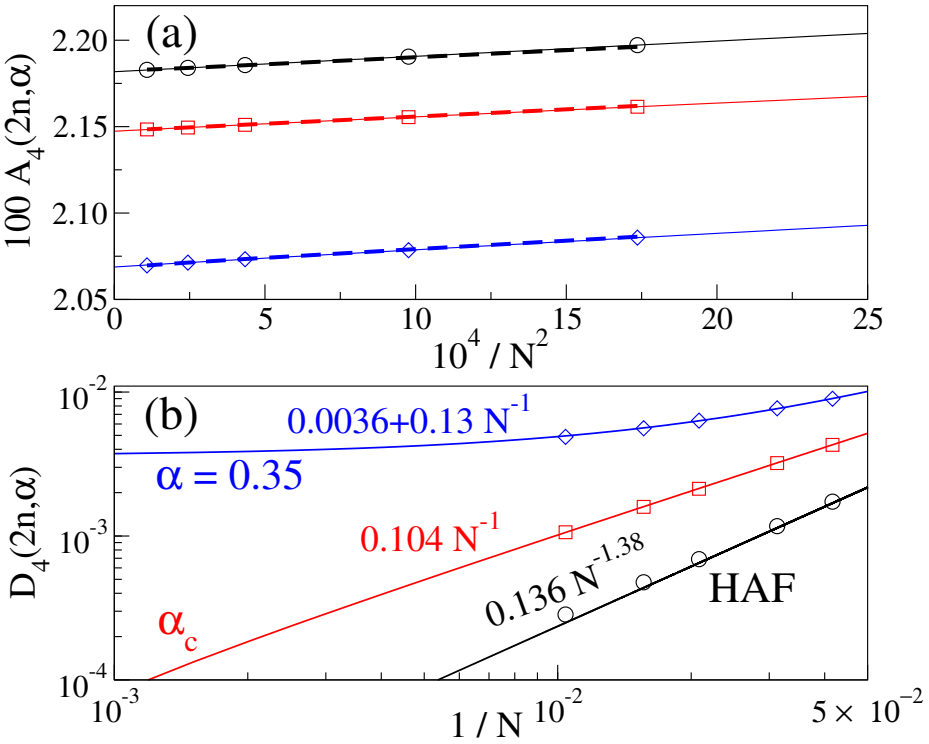

Figure 4.12: Size dependence of bond-bond correlation functions $C_4(2n,\alpha)$ in Eq. 4.19 up to $N = 4n = 96$ at $\alpha = 0$, a_c and 0.35. (a) Lines $A_4(2n,\alpha)$ are the arithmetic mean of $C_4(2n,\alpha)$ and $C_4(2n-1,\alpha)$; dashed lines are $C_2(1,\alpha,4n)^2$, Eq. 4.17, the square of the first neighbor spin correlation function. (b) The difference $D_4(2n,\alpha)$ in Eq. 4.20.

in the gapless phase to $C_2(1,\alpha)^2$ in the thermodynamic limit. The dashed line extends $C_2(1,\alpha)^2$ into the gapped phase. The lower panel shows $D_4(2n,\alpha)$ for distant bonds in finite systems whose thermodynamic limit is $\delta_e(\alpha)/32$ in Eq. 4.18. For $\alpha - 1/2 \ll 1$, the lowest-order corrections to $|K1\rangle$ are VB diagrams in which the adjacent paired spins such as $(1,2)(3,4)$ are paired instead as $(1,4)(2,3)$. Adjacent pairs $(2,3)(4,5)$ in $|K2\rangle$ are changed to $(2,5)(3,4)$.

Standard VB methods [147] verify that such corrections decrease $C_4(2n,1/2)$ for large n and lead to $C_4(2n-1,\alpha) < 0$ for $\alpha > 1/2$. The $\alpha > 1/2$ ground state $|G,\alpha\rangle$ that corresponds to $|K1\rangle$ at $\alpha = 1/2$ has AFM correlations $C_2(1,\alpha)$ between spins $2r$, $2r-1$ and ferromagnetic correlations between spins $2r$, $2r+1$. The spin correlations are reversed in the ground state that corresponds to $|K2\rangle$ at $\alpha = 1/2$. The net result is a maximum around $\alpha \sim 0.60$ in the lower panel that corresponds to $\delta_e(0.6) > 1$ in one broken-symmetry ground state and $\delta_e(0.6) < -1$ in the other.

To understand the thermodynamic limit of bond-bond correlations, it is instructive to consider the $J_1 - J_2$ model at $\alpha > 1$. The $J_1 = 0$ limit ($\alpha \to \infty$) corresponds to noninteracting HAFs on sublattices of

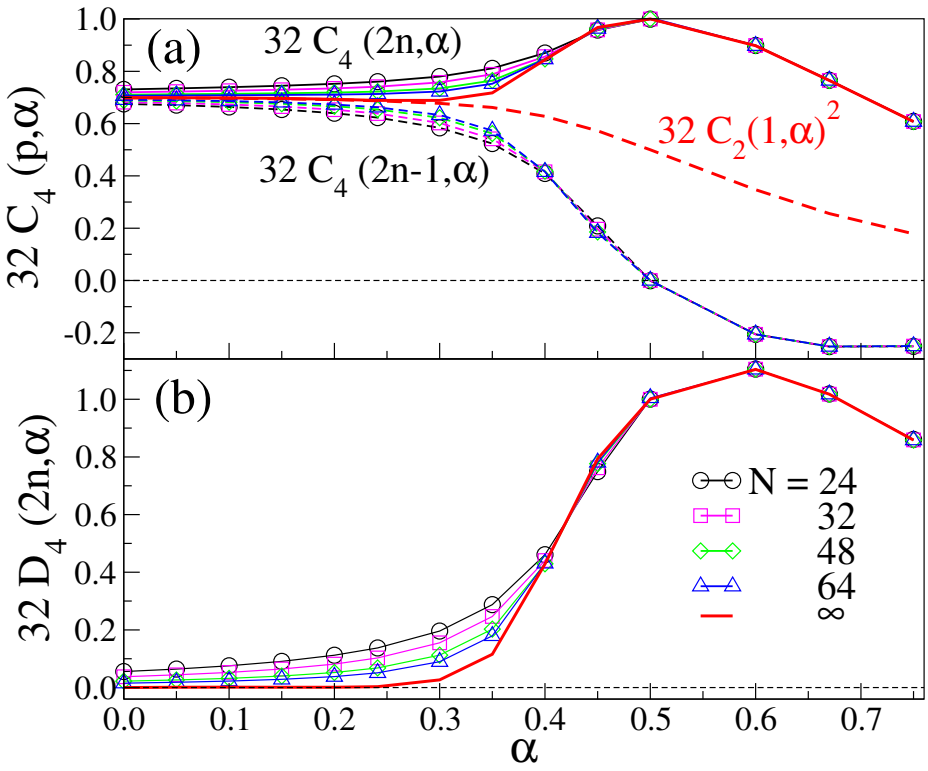

Figure 4.13: Bond-bond correlation functions at frustration α for $N = 4n$ spins in Eq. 4.4. (a) $C_4(2n,\alpha)$ and $C_4(2n-1,\alpha)$ in Eq. 4.20 are the most and second most distant bonds; $C_2(1,\alpha)$ is the thermodynamic limit of the first neighbor spin correlation function. (b) $32D_4(2n,\alpha)$ is electronic dimerization $\delta_e(\alpha)$ in the limit $n \to \infty$.

odd and even numbered sites, respectively, with known spin correlation functions. It follows immediately at $J_1 = 0$ that (1) spin-spin correlation functions such as $C_2(1,0)$ with odd $p = r' - r$ in Eq. 4.16 are identically zero and that (2) bond-bond correlation functions in Eq. 4.15 factor into products of sublattice spin-spin correlation functions such as

$$C_4(2n) = \left\langle S_1^x S_{2n+1}^x \right\rangle \left\langle S_2^x S_{2n+2}^x \right\rangle . \quad (J_1 = 0) \tag{4.21}$$

Since both HAF correlations are between nth neighbors, $C_4(2n)$ is positive and decreases as n^{-2} for distant spins. The corresponding expression for $C_4(2n-1)$ has spin correlations between nth neighbors of one sublattice and $(n-1)$th neighbors on the other; $C_4(2n-1)$ is negative and increases as n^{-2}. All correlation functions in Fig. 4.13 are zero at $J_1 = 0$ in the thermodynamic limit. The gapped phase terminates at the quantum critical point [21] $\alpha_2 = 2.27$ at the onset of a gapless decoupled phase with nondegenerate ground state and quasi-long-range-order at wave vector $q = \pi/2$.

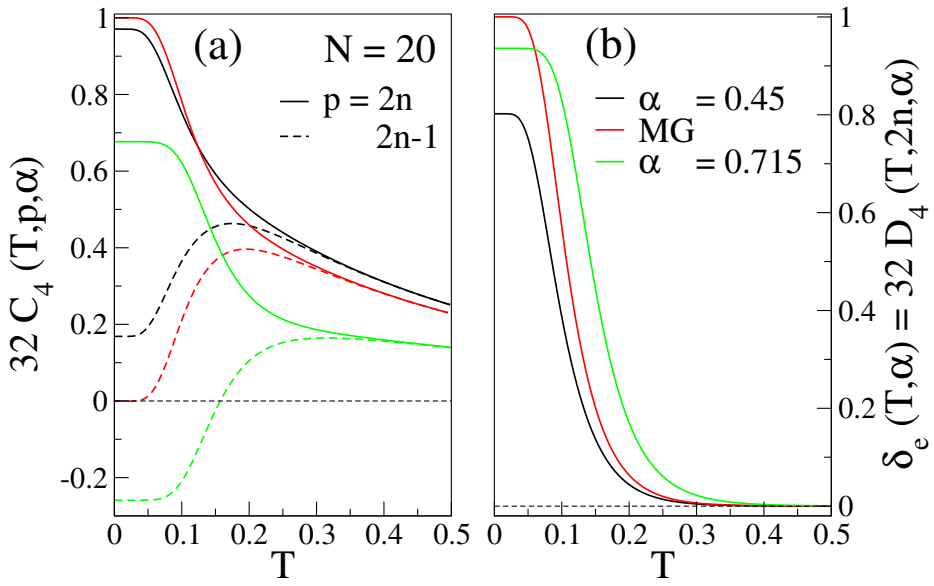

Figure 4.14: (a)Temperature dependence of bond-bond correlation functions $C_4(T,p,\alpha)$ at system size $N = 4n = 20$ and $\alpha = 0.45, 0.50$ and 0.715; lines for $p = 2n$, dashed lines for $p = 2n-1$. (b) electronic dimerization $\delta_e(T,\alpha) = 32D_4(T,2n,\alpha)$.

The T dependence of bond-bond correlation functions is obtained as usual. The partition function $Q(T,\alpha,N)$ is the sum of $\exp(-\beta E_j(\alpha,N))$ over 2^N states ($\beta = 1/k_BT$). We have

$$C_4(T,p,\alpha,N) = \frac{1}{(Q(T,\alpha,N))}\sum_j \left\langle j|S_1^{\alpha}S_2^{\alpha}S_{1+p}^{\alpha}S_{2+p}^{\alpha}|j\right\rangle \exp(-\beta E_j(\alpha,N)). \qquad (4.22)$$

Similar expressions hold for the spin-spin correlations $C_2(T,p,\alpha,N)$. Fig. 4.14 presents ED results for $N = 20$ at several α with large $\Delta(\alpha)$. The finite size gap $E_\sigma(\alpha,N)$ contributes at $T \sim 0$ but hardly matters around $T \sim \Delta(\alpha)$ in the region of interest where $N = 20$ is in, or almost in, the thermodynamic limit. We measured excitation energies in Eq. 4.22 from $E_\sigma(\alpha,N)/2$ and averaged the matrix elements of the two singlets.

T initially suppresses correlations between distant bonds, as shown by increasing $C_4(T,2n-1)$ for bonds in different Kekulé diagrams and decreasing $C_4(T,2n)$ for bonds in the same diagram. The T dependence of $C_2(T,1,\alpha)^2$ is related to the gap $\Delta(\alpha)$. Electronic dimerization $\delta_e(T,\alpha)$ decreases rapidly when $\beta\Delta(\alpha) < 1$.

The thermodynamic limit holds for $T > T_{SP} = 0.09$ in $J_1 - J_2$ models with $N \sim 50$ and $0 \le \alpha \le 3/4$ in Eq. 4.4. The calculated $\chi(T,\alpha,T_{SP})$ in Fig. 4.15 are quantitative for models with equilibrium $\delta(T,\alpha)$.

The logarithmic scale emphasizes low T. The units of χ are $J_1/N_A g^2 \mu_B^2$ where N_A is Avogadro's number, $g = 2.003$ is the free electron value (isotropic exchange excludes spin-orbit coupling) and μ_B is the Bohr magneton. The $T > T_{SP}$ susceptibility varies with frustration α in both gapped and gapless phases, but the $\chi(T, \alpha)$ maximum around 0.14 is roughly constant. The Curie law at high T is $1/4T$.

The measured $\chi(T)$ of $CuGeO_3$ indicated $\alpha = 0.35$ and $J_1 = 160$ K in crystals with $T_{SP} = 14$ K in Section 4.2. Electron spin resonance (ESR) with the applied magnetic field along the crystal c axis fixed [6] $g = 2.256$. The parameters α, J_1 and T_{SP} account for $\chi(T)$ over the entire range to 950 K and for the specific heat anomaly, as shown in Fig. 4.6. The coupling $T_{SP}/J_1 = 0.09$ motivated the choice of T_{SP} in Fig. 4.1. The measured [2] $\chi(T)$ of the organic SP crystal TTF-$CuS_4C_4(CF_3)_4$ with $T_{SP} = 12$ K and $g = 1.997$ from ESR is quantitatively modeled with $J_1 = 79$ K, $\alpha = 0$ and T_{SP} in Fig. 4.5. Since the coupling $T_{SP}/J_1 = 0.15$ is stronger, the thermodynamic limit is reached at $N \sim 32$.

The initial $\chi(T)$ analysis [2] was based on the HAF with correlated states for $T > T_{SP}$ and a mean-field approximation at lower T. As noted explicitly, the quantitative fit shown in Fig. 5 of Ref. [2] or in Fig. 10 of Ref. [3] required another parameter. The free fermions or BCS relation with $T_{SP} = 12$ K gave the observed T dependence but overestimated $\Delta(0)$ while the parameter $\Delta(0)$ needed for $\chi(T)$ at low T returned [2] $T_{SP} = 9$ K, a 25% discrepancy. The inconsistency is due to the mean-field approximation. The influential but incorrect conclusion [3] that the HAF gap relation is close to BCS strongly influenced the discussion of INS data in Fig. 4.8.

The $J_1 - J_2$ model with $\delta = 0, \alpha \neq 0$ in Eq. 4.4 has many additional quantum phases [114, 127] when $J_1 < 0$ and an applied magnetic field are considered as well as $J_1 > 0$. Physical realizations of gapped phases are very rare, however. $CuGeO_3$ may well be the first. Half-filled Hubbard-type models also support gapped quantum phases [37, 148, 149] with doubly degenerate BOW ground states and broken inversion symmetry at sites, but only over narrow ranges of parameters. Such models have charge as well as spin degrees freedom. Dimerization is associated with alternating transfer integrals $t(1 \pm \delta)$ along the chain. BOW phases and thermodynamics are less well characterized, both because interactions between charges require effective parameters that are poorly understood and because the models have about 4^N instead of 2^N states.

The defining features of BOW phases are magnetic and spectroscopic evidence for broken inversion symmetry at atomic or molecular sites in crystals whose structure has inversion symmetry ($\delta = 0$) at sites.

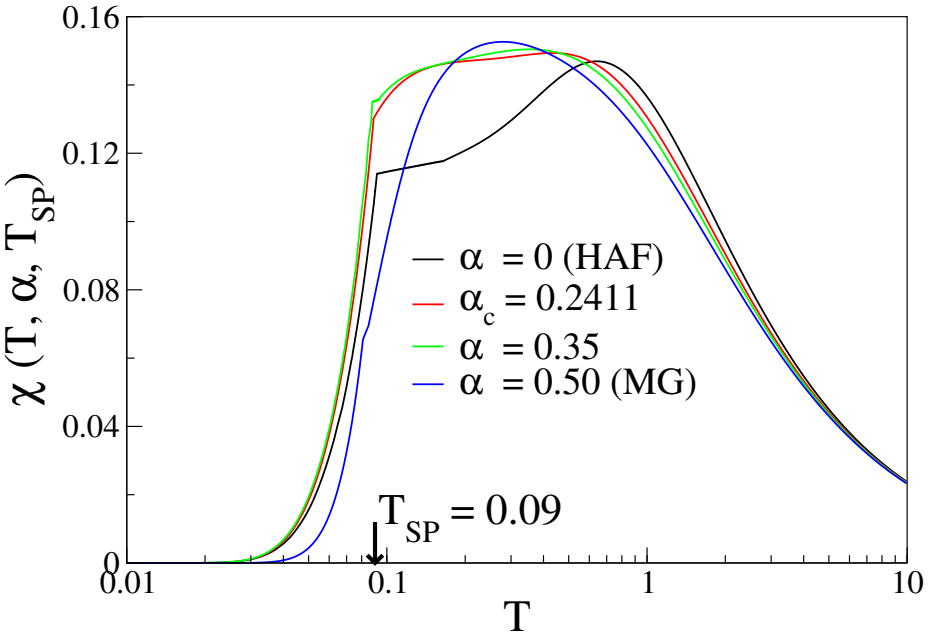

Figure 4.15: Magnetic susceptibility $\chi(T, \alpha, T_{SP})$ of chains with $T_{SP} = 0.09$ and variable α in Eq. 4.4.

Inversion symmetry at sites is trivially broken on dimerization ($\delta \neq 0$). It is also broken in linear combinations of the degenerate ground states $|G, \alpha, \pm 1\rangle$ of $\delta = 0$ chains with $\alpha > \alpha_c$ and $\delta_e(\alpha) \neq 0$.

The analysis at the MG point holds qualitatively in general. We contrast in Fig. 4.15 the T dependencies of *structural* dimerization $\delta(T)/\delta(0)$ and *electronic* dimerization $\delta_e(T)/\delta_e(0)$ in chains with $\alpha = 1/2$ and $T_{SP} = 0.06$. The magnitude of $\chi(T, 1/2, T_{SP})$ is given on the right (note the different scale). The gap $\Delta(1/2) = 0.233$ reduces the susceptibility maximum around $T \sim 0.25$ by over 50% at $T_{SP} = 0.09$ and by even more at $T_{SP} = 0.06$. The stiffness $1/\varepsilon_d$ is the parameter related to T_{SP} in deformable chains subject to Peierls or SP transitions and equilibrium $\delta(T, \alpha)$ at $T \leq T_{SP}$ while long-range bond-bond correlations leads to $\delta_e(T)$ in gapped deformable chains for $T \geq T_{SP}$.

In the present context, either dimerization can be studied by an appropriate probe of the electronic wave function, for example an intensity $I(T)$. Hubbard-type models have long been applied to face-to-face stacks of planar $S = 1/2$ molecular ions in organic salts or charge-transfer crystals [150]. Regular ($\delta = 0$) stacks with inversion symmetry at sites have Raman active, IR silent, totally symmetric (a_g) vibrations. Some a_g modes become strongly IR active in dimerized stacks, as also seen in polyacetylene, and are analyzed in terms of electron-phonon coupling [39, 151]. Since the IR intensity $I(T)$ turns on sharply at the transition, it provided a convenient and widely used way to identify Peierls transitions.

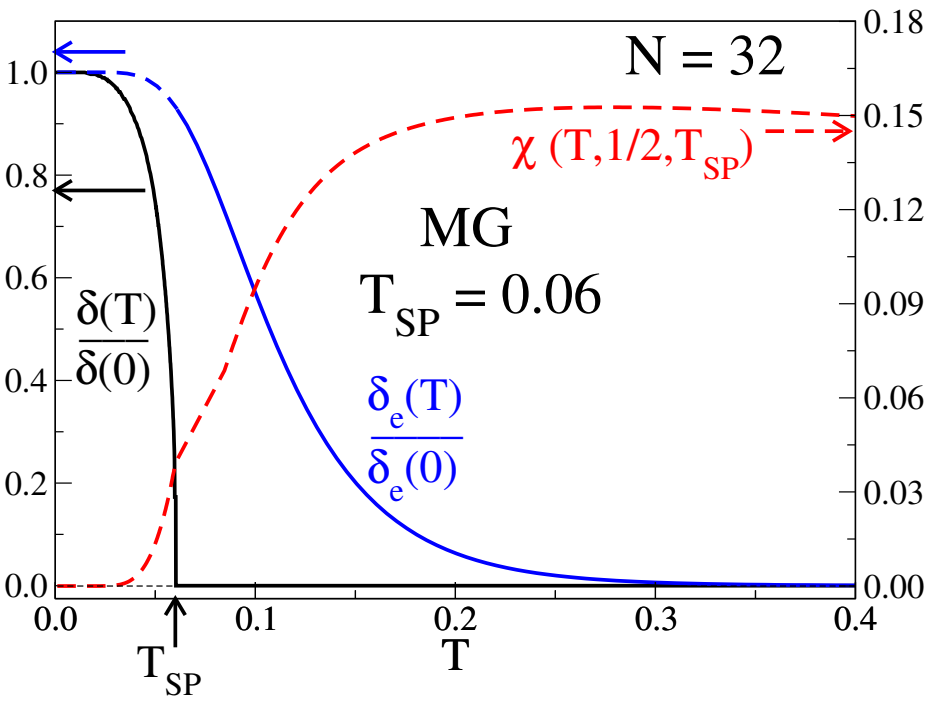

Figure 4.16: Equilibrium dimerization $\delta(T, 1/2)$ and susceptibility $\chi(T, 1/2, T_{SP})$ at the MG point for chains with $T_{SP} = 0.06$ and $N = 32$ spins. Electronic dimerization $\delta_e(T, 1/2)$ for $T \geq T_{SP}$ is discussed together with Eq. 4.22. The finite chain with $\alpha = 1/2$ and $T_{SP} = 0.06$ is in the thermodynamic limit.

The symmetry argument also applies to BOW phases that were not recognized at the time and where $I(T)$ follows $\delta_e(T)$ for $T \geq T_{SP}$. Smoothly decreasing $I(T)$ were reported [152, 153] as in Fig 4.16 in rare exceptional cases. The estimated $T_P \sim 220$ K of Rb-TCNQ(II) crystals was based [152] on $I(T_P)/I(25) \sim 1/2 \sim \chi(T_P)/\chi(300)$. The 100 K crystal structure [154] was subsequently found to be in the same space group, triclinic $P\bar{1}$, as the 295 K structure, thereby definitively ruling out a transition between 100 and 300 K. The evidence for a BOW system is compelling but qualitative. The 300 K structure of TMPD-TCNQ crystals has regular ($\delta = 0$) stacks and a large singlet-triplet gap. The IR intensity $I(T)$ decreased [153] gradually with T to $I(300)/I(15) \sim 20\%$ and to 10% at 350 K, the limit of thermal stability. The structure at lower T has not been reported. The peculiar combination in BOW systems of sites with C_i symmetry, large magnetic gaps and broken electronic C_i symmetry occurs naturally in gapped phases with doubly degenerate ground states.

4.6 Discussion

Structural changes at Peierls or SP transitions as well as thermal expansion or contraction have been probed by elastic X-ray or neutron scattering, as discussed in reviews of widely different classes of quasi-1D crystals [34, 155, 156]. We note that 3D changes are always found that in some cases exceed those of the 1D chain. While delicate growth conditions leave open the definitive $CuGeO_3$ structure, the largest change below T_{SP} is along the b axis rather than the $\sim 1\%$ dimerization of the chain along the c axis [157]. Small displacement $\pm u$ of Cu ions along c is consistent with the small calculated $\delta(0) = 0.025$ in the correlated model; they are related by the linear spin-phonon coupling constant. Elastic scattering below T_{SP} from superlattice points is due to structural changes, not just dimerization, that are all initiated at T_{SP} but do not necessarily vary identically with T.

We have applied the hybrid ED/DMRG method to the best characterized SP transitions and to the $J_1 - J_2$ model, Eq. 4.4, with frustration $0 \leq \alpha \leq 0.50$ and isotropic exchange J_1, $J_2 = \alpha J_1$ between first and second neighbors. We exploit the fact that $\delta(0)$ limits the range of spin correlations at $T = 0$ while finite T limits the range at $\delta = 0$. Internal consistency requires T_{SP} to govern both the stiffness $1/\varepsilon_d$ and dimerization $\delta(T)$. The relevant system size depends on T_{SP}/J_1, about 32 spins for the transitions modeled. When the thermodynamic limit can be reached, the SP transition becomes essentially model exact. The general problem is the SP transition at arbitrary T_{SP} while we have modeled specific systems with known T_{SP}.

Correlated states account quantitatively for the magnetic susceptibility of both crystals. On the theoretical side, $\delta(T)$ of that HAF deviates from free fermions or BCS, contrary to previous expectations based on mean field. We place $CuGeO_3$ in the dimer phase with $\alpha = 0.35$ on the basis of $\chi(T)$, the specific heat, the ratio $\Delta(T)/\Delta(0)$ of the singlet-triplet gap and INS data that provide an independent determination of $J_1 = 160$ K. The first inorganic SP system is also, to the best of our knowledge, the first physical realization of the dimer phase of the $J_1 - J_2$ model.

Isotropic exchange is assumed in 1D models studied by field theory or numerical methods, and that is indeed the dominant magnetic interaction that governs the thermodynamics of spin chains. But the models are approximate because corrections to isotropic exchange due to spin-orbit coupling are neglected. he spin-orbit coupling is more important in Cu(II) systems than for organic radicals. They are incomplete

because dipolar interactions between spins are neglected, as well as the hyperfine interactions with nuclear spins. The interchain interactions are also neglected.Neutron [9–12] and esr [158] data indicate $J' \sim J_1/10$ between chains and corrections to isotropic exchange, respectively, in $CuGeO_3$. More complete specific models are required for the low-T properties of materials with quasi-1D spin chains. Simpler 1D models with isotropic exchange are is the proper starting point for finer low-T modeling and are adequate for SP transitions.

We quantified long-range bond order in the degenerate ground states $|G, \alpha, \pm 1\rangle$ of gapped phases using the four-spin correlation functions $C_4(p, \alpha)$ in Eq. 4.15. Linear combinations of $|G, \alpha, \pm 1\rangle$ are BOWs with broken inversion symmetry and electronic dimerization $\delta_e(0, \alpha)$ that remains finite for $\Delta(\alpha)/T > 1$ in models with inversion symmetry at sites. The different T dependencies of $\delta(T, \alpha)$ for $T \leq T_{SP}$ and $\delta_e(T, \alpha)$ in Fig. 4.16 could in principle be evidence for physical realizations of BOW systems.

A static magnetic field H can readily be added to Eq. 4.4 as $-g\mu_B H S^Z$ where S^Z is the total spin component along H and μ_B is the Bohr magneton. Since total S is conserved, the energy spectrum $\{E(\delta, N)\}$ of correlated states has resolved Zeeman energies when $H > 0$, and the tensor g may often be taken as a scalar. Multiple studies of the SP transition of $CuGeO_3$ in applied fields a few Tesla have been reviewed [129]. The field dependence has been successfully modeled. We anticipate at most minor changes on analyzing magnetic field effects using correlated states.

The SP transitions may include all structural, spectroscopic, transport and thermodynamic characterization of condensed matter systems. The comprehensive review of Heeger et al. [35] of trans-polyacetylene, a prototypical Peierls system, discusses the consequences of dimerization, but there is no transition up to the limit of thermal stability. Some planar π-electron donors (D) and acceptors (A) crystallize in mixed face-to-face stacks $\ldots D^{\rho} A^{-\rho} D^{\rho} A^{-\rho} \ldots$ with charge transfer ρ that varies from $\rho \sim 0$ in neutral closed-shell molecules to $\rho \sim 1$ spin-1/2 radical ions. The reviews in Ref. [156] describe their neutral-ionic transitions or crossovers on cooling or under pressure. Inversion symmetry at sites at high T is broken on dimerization. Microscopic modeling becomes far more challenging in correlated systems with both charge and spin degrees of freedom. Refs. [34] and [155] discuss the characterization of other quasi-1D systems with charge and spin degrees of freedom and Peierls transitions to incommensurate as well as dimerized chains.

The structural changes at Peierls transitions are 3D rather than restricted to 1D chains or stacks. Conversely, a dimerization transition may have other origins. The cation radical stack in Wurster's blue per-

chlorate dimerizes at 180 K when perchlorate rotation stops. Considerable evidence and analysis are needed to recognize crystals with quasi-1D spin chains and a transition driven by a Peierls instability. Weak interactions between chains are more likely to induce a 2D or 3D transition at low T.

In summary, we have modeled the SP transition of the HAF and $J_1 - J_2$ model with $\alpha \leq 0.5$ in Eq. 4.4 using correlated states. The thermodynamic limit of finite chains is reached under conditions that are satisfied by T_{SP} of TTF-$CuS_4C_4(CF_3)_4$ and $CuGeO_3$. We have also observed that the SP transition depends strongly on frustration $\alpha = J_2/J_1$ because the $\alpha < \alpha_c = 0.2214$ phase is gapless with a nondegenerate ground state while $\alpha > \alpha_c$ is gapped with a doubly degenerate ground state.

5

Low temperature thermodynamics of correlated 1D fermionic models

5.1 Introduction

With an aim to demonstrate the applicability of the hybrid ED/DMRG method to 1D strongly correlated systems, we do not restrict our study only to spin systems. We also explore the fermionic models which play crucial role in analysing the electronic and magnetic properties in many organic salts and polymers [33–35]. These models have some interesting phase transitions which are the manifestation of the competition between hopping of electrons between sites and the interaction between electrons. Although fermionic models with both active charge and spin degrees of freedom are more general models than the spin models, solving the Hamiltonian matrix of fermionic models are numerically more challenging in most of the cases except when the electron is restricted to very low or very high filling. The reason lies in the fact that the Hilbert space dimension rises more rapidly with growth of the fermionic systems than the spin systems [for a chain of N sites, the number of basis goes as 2^N in spin models and 4^N in fermionic models in the thermodynamic limit]. Acknowledging the hybrid method general for all 1D correlated systems certainly demands its application to this numerically tough area of quantum many body models.

In this Chapter [1], we apply the ED/DMRG method to fermionic models. We consider 1D fermionic systems of N sites with periodic boundary conditions, N_e electrons or holes and electron transfer t with spin conservation between first neighbors. The noninteracting limit is a tight-binding band with single-particle energies $\varepsilon_k = -2t\cos k$, wavevectors $-\pi < k = 2\pi m/N \leq \pi$ in the first Brillouin zone and bandwidth $4t$. The Hubbard model has on-site repulsion $U > 0$ while the extended Hubbard model (EHM) also has spin-independent interaction V between neighbors. The same analysis holds for spin-independent interactions V_r of any range, for example in the Pariser-Parr-Pople model for π electrons in aromatic hydrocarbons. The models conserve the total spin $S \leq N_e/2$ and its z component S^Z.

The EHM Hamiltonian with sites r and $t = 1$ as the unit of energy is

$$H(U,V) = -\sum_{r,\sigma}(c^\dagger_{r,\sigma}c_{r+1,\sigma} + h.c.) + U\sum_r c^\dagger_{r,\alpha}c^\dagger_{r,\beta}c_{r,\beta}c_{r,\alpha} + V\sum_r n_r n_{r+1}. \tag{5.1}$$

The operators $c^\dagger_{r,\sigma}(c_{r,\sigma})$ create (annihilate) an electron with spin σ at site r, $h.c.$ is the Hermitian conjugate and $n_r = \sum_\sigma c^\dagger_{r,\sigma}c_{r,\sigma}$ is the number operator. The half-filled Hubbard model with $n = N_e/N = 1$ and $V = 0$ has been of special interest mathematically. Using the Bethe ansatz, Lieb and Wu [159] proved that $U > 0$ opens a gap for conduction and generates a paramagnetic Mott insulator. Takahashi [14] obtained the magnetic susceptibility at $T = 0$. More recently, Jüttner, Klümper and Suzuki [160] obtained the exact thermodynamics and elementary excitations at arbitrary filling, and they related their results to other models to which the Bethe ansatz is applicable. Exact results are limited to $V = 0$ and to models on rigid lattices with one site per unit cell.

1D models on deformable lattices with electron-phonon coupling are subject to the Peierls instability that lowers the symmetry and is essential for physical realizations. The Peierls instability of polyacetylene is associated with bond length alternation, topological solitons and mid-gap excitations [35]. The ground state of Eq. 5.1 at V = 0 is unconditionally unstable to dimerization when $N_e = N$, while quarter filling with either electrons or holes leads to tetramerized chains in organic molecular crystals that include superconductors. Peierls instabilities or transitions have been studied [34, 131, 155] in many materials with quasi-1D chains, both inorganic and organic, both conductors and insulators at $T > T_P$. Although we

[1] The work reported here is based on " *Density matrix renormalization group approach to the low temperature thermodynamics of correlated* 1*d fermionic models*", Sudip Kumar Saha, Debasmita Maiti, Manoranjan Kumar, and Zoltán G. Soos, arXiv:2101.04362 [cond-mat.str-el] (2021).

limit discussion to rigid lattices that allow sharp comparison with theory, the motivation is to analyze thermodynamic data at cryogenic temperatures, or reduced $T \sim 0.01$ in systems with electronic integrals of order $t \sim 10^3$ K. The ED/DMRG method is equally applicable to deformable lattices with spin-phonon coupling and spin-Peierls transitions [161].

The molar magnetic susceptibility $\chi(T)$ provides by far the most direct contact with experiment since electronic spins dominate the magnetism. The spin specific heat $C(T)$ can be extracted from lattice (phonon) contributions at $T < 20$ K or in systems with high-spin, low-spin transitions. Even with magnetic fields of ~ 20 T, substantial magnetization of systems with AFM interactions is limited to $T < 100$ K. The reduced unit for $\chi(T)$ is $N_A g^2 \mu_B^2 / t$ where N_A is the Avogadro constant, μ_B is the Bohr magneton and $g = 2.0032$ is the free electron value. Since S is conserved, the models in Eq. 5.1 do not have spin-orbit coupling. The half-filled band at 0 K has filled states $\varepsilon_k = -2 \cos k$ up to the Fermi wavevector $k_F = \pm\pi/2$. The Pauli paramagnetism is

$$\chi(T) = \frac{\beta}{4\pi} \int_0^{\pi/2} \frac{dk}{\cosh^2(\beta \cos k)} \tag{5.2}$$

with $\beta = 1/T$ in reduced (T/t) units. The band limit poses a natural and challenging test of methods based on finite systems. At issue is the extreme size dependence of the $T \sim 0$ thermodynamics that follows from the Hückel $4p$, $4p + 2$ rule. The ground state is 6-fold degenerate (a triplet and three singlets) when $N_e = 4p$. There are two electrons in the degenerate states at $k_F = \pm\pi/2$ when $N = N_e$ and $\chi(T, N)$ diverges as $1/NT$. The singlet ground state is nondegenerate when $N_e = 4p + 2$, all states up to k_F are doubly occupied and $\chi(0, N) = 0$.

The upper panel of Figure 5.1 shows $\chi(T, N)$ at the indicated system sizes, exact up to N = 14. Larger N is based on DMRG and a truncated energy spectrum discussed later. The $\chi(T, N)$ curves merge or cross from above and below for $N = 4p$ and $4p + 2$, respectively, at points T_N shown as points. The points clearly require only the low-energy part of the spectrum $\{E(N)\}$. The blue line in the lower panel is $\chi(T, 14)$ at high T, connects the points T_N at low T and is extrapolated to $T = 0$. The red line is the thermodynamics limit, Eq. 5.2, with $\chi(0) = 1/4\pi$. The ED/DMRG line deviates from the band result at intermediate and high T for reasons discussed in Section 5.2. The method is approximate for fermionic systems, in contrast to spin chains [81] where $\chi(T, N)$ converges to $\chi(T)$ exactly at high T.

Spin degrees of freedom dominate the low T thermodynamics of half-filled models with $U \geq 4$ or

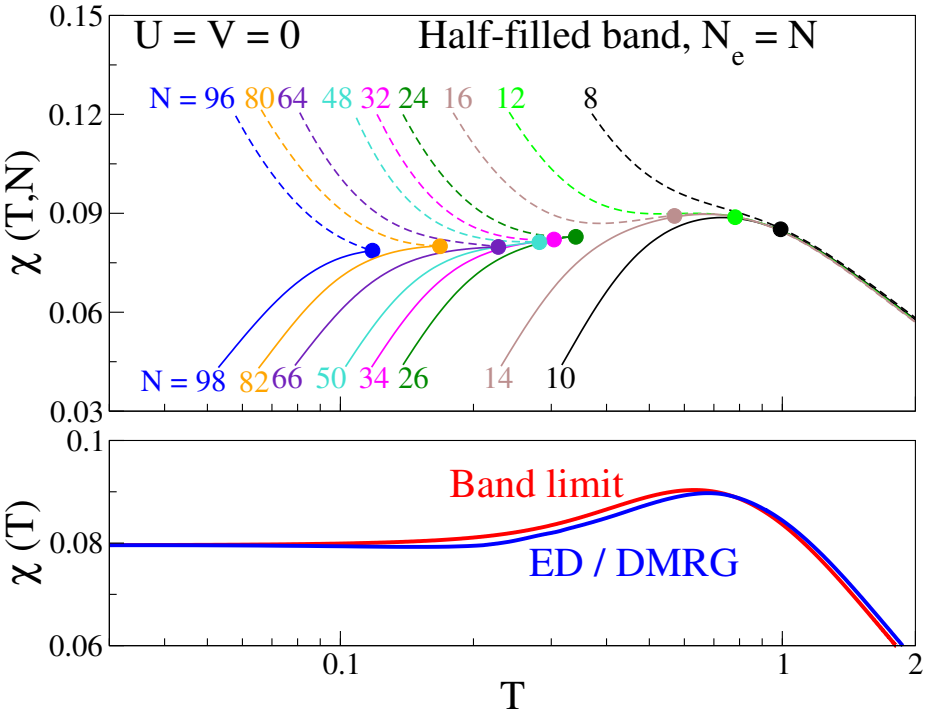

Figure 5.1: Upper panel: Molar magnetic susceptibility $\chi(T,N)$ of systems with $N_e = N$ and $U = V = 0$ in Eq. 5.1, exact for $N \leq 14$. DMRG for larger N is shown up to the crossing or merging points T_N at system size $N = 4p, 4p+2$. Lower panel: The band limit is Eq. 5.2; ED/DMRG is through the points T_N and extrapolated to $T = 0$.

$U - V \geq 4$ in Eq. 5.1. Klein and Seitz [162] derived the spin Hamiltonian of the half-filled Hubbard model in powers of $(t/U)^2$, as required for virtual transfers between spin states with $n_r = 1$ at all sites. The first two terms are exchanges J_1 and J_2 between first and second neighbors,

$$J_1 = \frac{4t^2}{U} - \frac{16t^4}{U^3}, \qquad J_2 = \frac{4t^4}{U^3}. \tag{5.3}$$

Von Dongen [163] obtained the same exchanges for the EHM with $U-V$ instead of U in the denominator of the t^2 term and $(U-V)^3/(1+V/U)$ instead of U^3 in the denominator of the t^4 terms. The Hamiltonian with periodic boundary conditions and spins $S_r = 1/2$ is

$$H(J_1,J_2) = J_1 \sum_r \vec{S}_r \cdot \vec{S}_{r+1} + J_2 \sum_r \vec{S}_r \cdot \vec{S}_{r+2}. \tag{5.4}$$

Spin-1/2 chains describe the low T thermodynamics of half-filled fermionic models when interactions exceed the bandwidth; J_1 is typically of order 10 to 100 K. The smaller Hilbert space of 2^N spin states is of course very advantageous numerically.

The Chapter is organized as follows. The method developed in Section 5.2 begins with the scaled partition function that accounts for the size dependence of the many-fermion basis. The DMRG procedure is then summarized for targeting hundreds of correlated states $E_p(N)$ in sectors $S^Z \leq N_e/2$ at system size N and compared to excitations of noninteracting fermions. Finally, energy cutoffs with $E_p(N) \leq E_C(N)$ are introduced to obtain the low T thermodynamics in a narrow range at system size N. Section 5.3 discusses representative applications of Eq. 5.1 that include half-filled Hubbard models with (a) $U \leq 4$, the bandwidth; (b) $U > 4$ and spin-charge separation with low T thermodynamics given by Eq. 5.4; (c) Quarter-filled models; (d) Half-filled EHM with $U = 4$ and $V \sim 2$ in the range of the bond-order-wave (BOW) quantum phase. ED/DMRG results, primarily for $\chi(T)$ and the entropy $S(T)$ per site, are related to exact and TMRG results. Section 5.4 contains brief comments about the method.

5.2 Methods

5.2.1 Scaled partition function

Fermionic models with N sites and N_e electrons have a large but finite number of states $W(N, N_e)$. Since the Boltzmann factors are unity in the high T limit, the entropy density or entropy per site is $N^{-1} \ln W(N, N_e)$ and must be a continuous function of $n = N_e/N \leq 2$ in the thermodynamic limit. Fermionic systems differ in this respect from spin-S systems with $W(N, S) = (2S+1)^N$ and $N^{-1} \ln W(N, S) = (2S+1)$ for any integer N. To obtain the proper high T limit, we introduce below a scale factor $\lambda(N, n)$ that returns for finite N the thermodynamic limit at $n = N_e/N$.

Distributions of N_e fermions on N sites lead to $q \leq N_e/2$ doubly occupied sites with $n_r = 2, N_e - 2q$ singly occupied sites with $n_r = 1$ and spin α or β, and $N - N_e + q$ unoccupied sites with $n_r = 0$. The dimension of the many fermion basis is

$$W(N, N_e) = \sum_{q=0}^{N_e/2} \frac{N!\, 2^{N_e-2q}}{q!\,(N - N_e + q)!\,(N_e - 2q)!}. \tag{5.5}$$

The probability of q doubly occupied sites is $W(q, N, N_e)/W(N, N_e)$, and the most probable distribution becomes exact in the thermodynamic limit. We treat q/N as continuous, find the maximum of $\ln W(q, N, n)$ at $n = N_e/N$ with respect to q and obtain $q_{mp}(n)/N = n^2/4$. With this value for q, the

Table 5.1: Number of states $W(N, N_e)$, Eq. 5.5, and $N^{-1} \ln \lambda(N, n)$ for N sites and $N_e = N$ or $N/2$.

N	$W(N, N)$	$N^{-1} \ln \lambda(N, 1)$	$W(N, N/2)$	$N^{-1} \ln \lambda(N, 1/2)$
8	12870	0.203	1820	0.186
10	184756	0.174	15504	0.160
12	$2.70E+06$	0.152	134596	0.141
16	$6.01E+08$	0.123	$1.05E+07$	0.114
20	$1.38E+11$	0.104	$8.48E+08$	0.0968
28	$7.65E+15$	0.0801	$5.81E+12$	0.0750
36	$4.43E+20$	0.0658	$4.14E+16$	0.0618
48	$6.44E+27$	0.0523	$2.61E+22$	0.0493
64	$2.40E+37$	0.0415	$1.48E+30$	0.0392
96	$3.61E+56$	0.0297	$5.15E+45$	0.0283

thermodynamic limit of $N^{-1} \ln W(N, N_e)$ is

$$N^{-1} \ln W(N, n) \to \ln \left(4n^{-n} (2-n)^{n-2} \right) \equiv \ln g(n). \tag{5.6}$$

The straightforward interpretation is that there are $nN/2$ sites with either spin α or β. The density of doubly occupied sites is $n^2/4$; the density of unoccupied sites is $(1 - n/2)^2$; the remaining $n(1 - n/2)$ sites are singly occupied. We define the scale factor $\lambda(N, n)$ as

$$\lambda\,(N, n)\; W\,(N, N_e) = g(n)^N \tag{5.7}$$

Scaling increases $W(N, N_e)$ such that it matches the thermodynamics limit. We have $g(1) = 4$ at half filling, $g(1/2) = g(3/2) = 16/3^{3/2}$ and $g(n) \to 0$ for $n \to 0$ or 2. Table 5.1 lists $N^{-1} \ln \lambda(N, n)$ and $W(N, N_e)$ at $n = 1$ and $1/2$. The dimension of the basis involves counting and holds for arbitrary interactions. The size dependence is still appreciable at $N \sim 100$.

The canonical partition function $Q(T, N, N_e)$ is the Boltzmann weighted sum over the spectrum $\{E(N, N_e)\}$ of models with N sites and N_e electrons. ED returns the full spectrum of correlated states of small systems. The scaled partition function with $\beta = 1/T$ is

$$Q_\lambda\,(T, N, N_e) = \lambda(N, n) \sum_j \exp -\beta E_j(N, N_e). \tag{5.8}$$

Scaling ensures that the numerical value of $N^{-1} \ln Q_\lambda(T, N, N_e)$ in the high T limit is $\ln g(n)$ in Eq. 5.7.

The details of $\{E(N,N_e)\}$ do not matter when T is large compared to energy differences and the sum in Eq. 5.8 becomes an integral over excitation energies. Of course, finite-size gaps inevitably become important at low T when, however, only low-energy excitations contribute to the partition function.

We compute the entropy per site and use $S_\lambda(T,N,N_e)$ for the scaled entropy,

$$S_\lambda(T,N,N_e) = S(T,N,N_e) + N^{-1}\ln\lambda(N,n). \tag{5.9}$$

As shown below, $S_\lambda(T,N,N_e)$ greatly facilitates finding the thermodynamic limit $S(T,n)$ even though the energy spectrum of finite systems is retained. First, we address the difference between the band and ED/DMRG $\chi(T)$ in the lower panel of Fig. 5.1.

The energy spectrum of Eq. 5.1 in a static magnetic field h has Zeeman components $E_j(N,N_e) - mhS_j$ with m ranging from $-S_j$ to S_j in states with spin S_j. The susceptibility is given by derivatives of $\ln Q(T,N,N_e,h)$ evaluated at $h=0$. Nevertheless, $\chi(T,N,N_e)$ depends on system size. The high T limit of $\chi(T,N,N_e)$ is a Curie law, $1/4T$ in reduced units, for a density $\rho_1(N,N_e)$ of $S=1/2$ sites. The size dependence of $\rho_1(N,N)$ follows from Eq. 5.5,

$$\rho_1(N,N) = \sum_{q=0}^{N/2}\left(1-\frac{2q}{N}\right)W(q,N,N)/W(N,N). \tag{5.10}$$

We have $\rho_1 = 0.53333$ and 0.52631 at $N=8$ and 10, larger than the thermodynamic limit $\rho_1(1) = 0.50$. Hence $\chi(T,14)$ in Fig. 5.1 is larger than $\chi(T)$ at high T by a known amount that can be verified quantitatively and can explicitly be shown to depend on system size but not on interactions. Deviations at $T\sim 1$ occur in larger systems with, for example, $\rho_1 = 0.51064$ and 0.50526 at $N=24$ and 48, respectively. It follows that $\chi(T,N)\to\chi(T)$ with increasing N, although numerical results are then limited to very low T. We approximate the thermodynamic limit of $\chi(T)$ to an accuracy shown in Fig. 5.1 for noninteracting fermions with ED to $N=14$. The high T limit of finite spin chains, by contrast, returns the thermodynamic limit because $N^{-1}\ln W(N) = (2S+1)$ is size independent without scaling.

Fig. 5.2 shows exact entropy densities of half-filled noninteracting systems. The band limit (red curve) is initially linear in T and reaches $2\ln 2$ at high T. The $N=8$ and 12 curves start at $S(0,4p) = (4p)^{-1}\ln 6$ and cross at finite T. The $N=10$ and 14 curves have finite size gaps and $S(T,14)$ is larger than $S(T,10)$ at

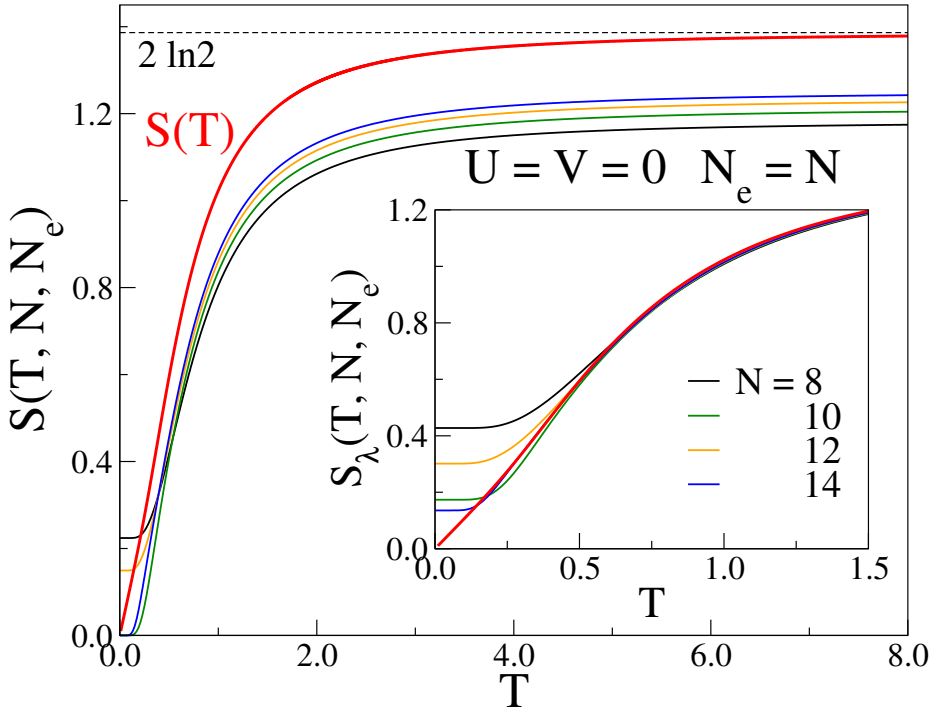

Figure 5.2: Exact entropy per site $S(T, N, N_e)$ of systems with $N = N_e \leq 14$ and $U = V = 0$ in Eq. 5.1; the band limit is $S(T)$. Inset: Scaled $S_\lambda(T, N, N_e)$ and $S(T)$ up to $T = 1.5$. The high T limit of $S(T)$ or $S_\lambda(T, N, N_e)$ is $2ln2$.

all T. The inset shows the scaled entropy $S_\lambda(T, N, N_e)$ at the same system sizes. The thermodynamic limit $S(T)$ is reached at $T > 0.6$ with $N = 4p$ converging from above and $N = 4p + 2$ crossing $S(T)$ at low T. An upward shift of $N^{-1} \ln \lambda(N, 1)$ of the $S(T, N, N)$ returns $S(T)$ for $T > 0.6$. In this case, $S_\lambda(T, 14, 14)$ is an excellent approximation to $S(T)$ for $T > 0.15$.

Finite models have $S_\lambda(0, N, N_e) > 0$ while gapless models with a nondegenerate ground state have linear $S(T)$ close to $T = 0$. It follows that the $S_\lambda(T, N, N_e)$ and $S(T)$ curves cross at low T in gapless models with $N_e = 4p + 2$. Entropy conservation and convergence to $S(T)$ at $T > T(N, N_e)$ then ensure convergence from below to the thermodynamic limit with increasing system size. Aside from the crossing region at low T, models with a nondegenerate ground states and $N_e = 4p + 2$ satisfy

$$S_\lambda(T, N_e) \leq S(T, n). \tag{5.11}$$

Let us suppose that DMRG returns the energy spectrum $E(N, N_e) \leq E_C(N, N_e)$ up to a cutoff that leads to a truncated $S_C(T, N, N_e)$. Since Boltzmann factors and excitation energies are non-negative, truncation cannot increase the entropy. The crossings shown in the inset for noninteracting fermions provide

a general approach to correlated systems: Truncated $S_\lambda(T, N_e)$ with $N_e = 4p + 2$ converge from below to $S_\lambda(T, N_e)$ on increasing $E_C(N)$ and $S_\lambda(T, N_e)$ converges from below to $S(T, n)$ on increasing N. In principle, $S(T, n)$ can be obtained by first increasing $E_C(N)$ and then N.

5.2.2 DMRG

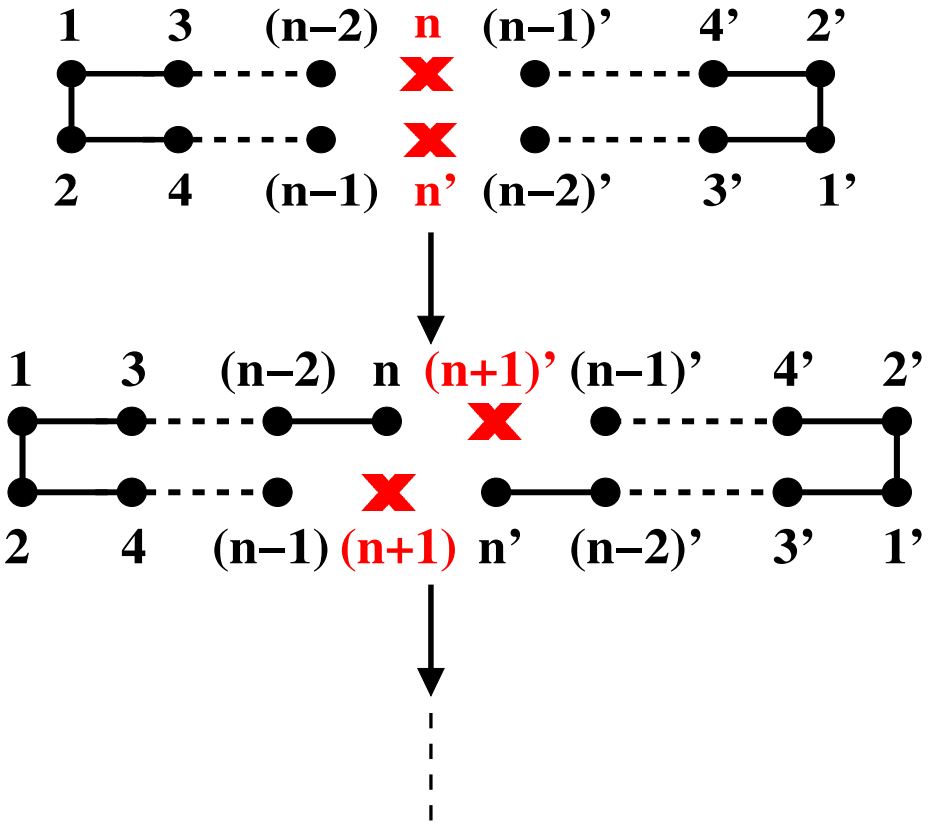

Figure 5.3: Infinite DMRG algorithm for a system with periodic boundary conditions. Left and right block sites are numbered as unprimed and primed integers, respectively. Sites of left and right blocks are shown as black circles and new sites added at DMRG steps are represented by red crosses.

The models in Eq. 5.1 conserve S and $S^Z \leq N_e/2$. DMRG calculations are performed in sectors with fixed S^Z using an algorithm for periodic boundary conditions similar to Ref. [37]. The superblock consists of two new sites, a left new and right new site in addition to the left and right blocks. For improved implementation of periodic boundary conditions, we modified the addition of new sites in the infinite DMRG algorithm. New sites are now added alternately at each end of the left and right block as shown in the Fig. 5.3. The left and right block are increased by one site at each step of infinite DMRG until the desired system size N is reached. We chose $m = 500$ eigenvectors of the density matrix of the system

block that corresponds to the highest eigenvalues after testing $m = 300$ and 400. The dimension of the superblock, the Hamiltonian matrix, is $m^2 4^2$, and the computational cost to diagonalize the Hamiltonian goes as $O(m^3)$. To optimize the efficiency our calculation we use $m \sim 500$ and $5 - 10$ sweeps of finite DMRG for all the calculation.

We seek the low energy excitations $E_p(N)$ at system size N instead of the ground state. To improve the accuracy of the low lying spectrum, we construct the system block density matrices $\rho_l(N)$ with l targeted energy levels of the superblock at system size N and define an effective density $\rho'(\beta', l)$

$$\rho'(\beta', l, N) = \sum_{p=1}^{l} \frac{\rho_p(N) \exp\left[-\beta' E_p(N)\right]}{Q_l(T, N)}. \tag{5.12}$$

The $l = 1$ case is simply $\rho'(\beta, 1) = \rho_1$ when the ground state is sought. Contributions for $l > 1$ are governed by β', an effective inverse T. We set $\beta' = 10$ (in units of $1/t$) since $T \sim 0.1$ is the range of interest. Variations of β' by 10% to 20% hardly change the accuracy of the spectrum. The effective density matrix becomes important when the lowest excitations are closely spaced and projection of all the degenerate states of superblock have equal contribution in constructing the density matrix of the system block.

The system block Hamiltonian and all operators are renormalized by $\rho'(\beta, l, N)$ to obtain the energy spectrum of the model Hamiltonian at system size N. We perform two calculations. We first take $l = 5$ or 10 in order to obtain the lowest excitations very accurately. The second calculation has $l > 100$ (most calculations have $l = 200$). The entire spectrum is red shifted by approximately a constant amount because the density matrix now has projections from many excited states. Accordingly, we shift back the spectrum by a constant and use the first calculation for the lowest excitations.

The absolute ground state of the models studied is in the $S^Z = 0$ sector, which contains a Zeeman component of all states with $S > 0$. The sectors $S^Z > 0$ are doubly degenerate and $l = 200$ contains states at higher energy than $l = 200$, $S^Z = 0$ or $S^Z = 1$. As shown in Section 5.2.3, fewer states suffice for converged thermodynamics at low T.

We have already mentioned the single-particle states $\varepsilon_k = -2\cos k, -\pi < k \leq \pi$ of Eq. 5.1 with $U = V = 0$ at system size N. The ground-state degeneracy in the $S^Z = 0$ sector is 4 or 1 for $N_e = 4p$ or $4p + 2$. The exact excitation spectrum for $S^Z = 0$ and its degeneracy are easily obtained for a single electron-hole pair or for two e-h pairs. We compare exact and DMRG excitations in the $S^Z = 0$ sector for

half-filled systems in Table 5.2 and Table 5.3 and quarter-filled systems in Table 5.4. The exact excitations $E_{p-p'}$ are degenerate from states p to p'. The DMRG accuracy decreases from a percent or so at p to about 10% to 20% at p', as seen both for different $E_{p-p'}$ at fixed N and same $E_{p-p'}$ at different N. We also notice that the accuracy decreases from p to p' for highly degenerate excitations.

The ground state $E_1(N, N_e)$ is nondegenerate for $N = N_e = 4n + 2$ in Eq. 5.1 with $U = V = 0$. The $S^Z = 0$ spectrum starts with 8-fold degenerate $E_2(N) = 4 \sin \pi/N$. The 16-fold degenerate $E_9 = 2(\sin \pi/N + \sin 3\pi/N)$ and 18-fold degenerate $E_{26} = 8 \sin \pi/N$ are closely spaced. The DMRG entries in Table 5.2 are the lowest and highest excitations p and p' in the indicated range. Similar accuracy is found at $N = 26$ and 50 for $E_2(N)$. The accuracy decreases at higher energy. As discussed in Section 5.2.3, the spectrum converges to the thermodynamic limit at and slightly above $T(N)$, and $T(26) = 0.34$, $T(50) = 0.26$ are comparable to the finite size gaps.

Table 5.2: Exact and DMRG excitations $E_p(N)$ of half-filled bands in the $S^Z = 0$ sector of Eq. 5.1 with $U = V = 0$ at $N = 26$ and 50. The ground state is $E_1(N) = 0$.

$N = 26, p$ to p'	Exact	DMRG, p	DMRG, p'
$2 - 9$	0.48215	0.48424 (0.4%)	0.49841 (3.3%)
$10 - 25$	0.95028	0.96018 (1.03%)	1.01408 (6.3%)
$26 - 43$	0.96429	1.01472 (5.0%)	1.04654 (7.9%)
$44 - 59$	1.3772	1.42575 (3.4%)	1.47179 (6.4%)
$60 - 67$	1.41842	1.47328 (3.7%)	1.48670 (4.6%)
$68 - 139$	1.43243	1.48690 (3.7%)	1.75015 (18%)
$N = 50, p$ to p'	Exact	DMRG, p	DMRG, p'
$2 - 9$	0.25116	0.25465 (1.4%)	0.28588 (12%)
$10 - 25$	0.50034	0.53080 (5.7%)	0.60177 (17%)
$26 - 43$	0.50232	0.60315 (17%)	0.78581 (36%)
$44 - 59$	0.74362	0.84416 (12%)	0.92243 (19%)
$60 - 67$	0.74953	0.92554 (19%)	0.96228 (22%)
$68 - 139$	0.75151	0.96438 (22%)	1.31098 (43%)

The $N = N_e = 4n$ ground state is 4-fold degenerate in the $S^Z = 0$ sector. The DMRG excitation E_4 is 2×10^{-4} at $N = 24$ and 3×10^{-3} at $N = 48$. The exact excitation $E_5(N) = 2 \sin 2\pi/N$ is 16-fold degenerate, as is $E_{21} = 2 \sin 4\pi/N$, while the double e-h excitation $E_{37} = 4 \sin 2\pi/N$ is 6-fold degenerate in Table 5.3. $T(24) = 0.34$ and $T(48) = 0.28$ are again comparable to the finite size gaps.

Table 5.3: Exact and DMRG excitations $E_p(N)$ of half-filled bands in the $S^Z = 0$ sector at $N = 24$ and 48. The ground state is $E_1(N) = 0$.

$N = 24, p$ to p'	Exact	DMRG, p	DMRG, p'
$5 - 20$	0.51764	0.51943 (0.4%)	0.54288 (4.4%)
$21 - 36$	1.0	1.05572 (5.3%)	1.06220 (5.9%)
$37 - 84$	1.03528	1.06265 (2.6%)	1.33922 (23%)
$85 - 150$	1.51764	1.61214 (5.9%)	1.75258 (13%)
$N = 48, p$ to p'	Exact	DMRG, p	DMRG, p'
$5 - 20$	0.26105	0.26435 (1.3%)	0.31114 (16%)
$21 - 36$	0.51764	0.55063 (6.0%)	0.56949 (9.1%)
$37 - 84$	0.52210	0.57378 (9.0%)	0.74625 (30%)
$85 - 150$	0.76537	0.87253 (12%)	1.06347 (28%)

Table 5.4: Exact and DMRG excitations $E_p(N)$ of quarter-filled bands in the $S^Z = 0$ sector at $N = 64$ and 68. We have $E_1(N) = 0, E_4(64) = 10^{-3}$ and $T(68) = 0.12$ is close to the finite size gap.

$N = 64, p$ to p'	Exact	DMRG, p	DMRG, p'
$5 - 12$	0.13181	0.13278 (0.7%)	0.14694 (10%)
$13 - 20$	0.14543	0.15945 (8.8%)	0.17789 (18%)
$21 - 28$	0.24873	0.28279 (12%)	0.29121 (15%)
$29 - 32$	0.26361	0.29169 (9.6%)	0.29283 (10%)
$33 - 72$	0.27723	0.29288 (5.3%)	0.44203 (37%)
$73 - 76$	0.29085	0.44422 (35%)	0.45941 (37%)
$77 - 84$	0.30307	0.46292 (35%)	0.46870 (35%)
$85 - 88$	0.34963	0.46943 (26%)	0.47284 (26%)
$N = 68, p$ to p'	Exact	DMRG, p	DMRG, p'
$2 - 9$	0.13063	0.13184 (0.9%)	0.14315 (8.8%)
$10 - 17$	0.24864	0.26296 (5.4%)	0.27749 (10%)
$18 - 35$	0.26125	0.28334 (7.8%)	0.34264 (24%)
$36 - 43$	0.27275	0.34701 (21%)	0.40600 (33%)
$44 - 51$	0.35304	0.40615 (13%)	0.41282 (15%)
$52 - 91$	0.37927	0.41485 (8.6%)	0.54523 (30%)
$92 - 99$	0.39077	0.54834 (28%)	0.57525 (32%)

The excitations in quarter-filled bands are shown in Table 5.4. The Fermi level at $k_F = \pm\pi/4$ has 2 or 4 electrons when $N_e = N/2$ is $4p$ or $4p + 2$. The $4p$, $S^Z = 0$ ground state is 4-fold degenerate while the $4p + 2$ ground state is nondegenerate. The degeneracy of exact excitations is lower than at $N = N_e$ because $\varepsilon(k)$ is not symmetric about $k_F = \pm\pi/4$.

As in standard DMRG, accuracy and computational effort increase with m. We found $m = 500$ to be clearly superior to 300 or 400 and almost comparable to $m = 600$ in some test calculations. The

choice of l or β' in Eq. 5.12 for targeting correlated spectra at system size N is less tested. Thermodynamic comparisons with band theory or with exacts results for correlated systems are more appropriate in our opinion than excitation spectra, except for the spin or charge gaps that are accessible to standard DMRG.

5.2.3 Energy cutoff

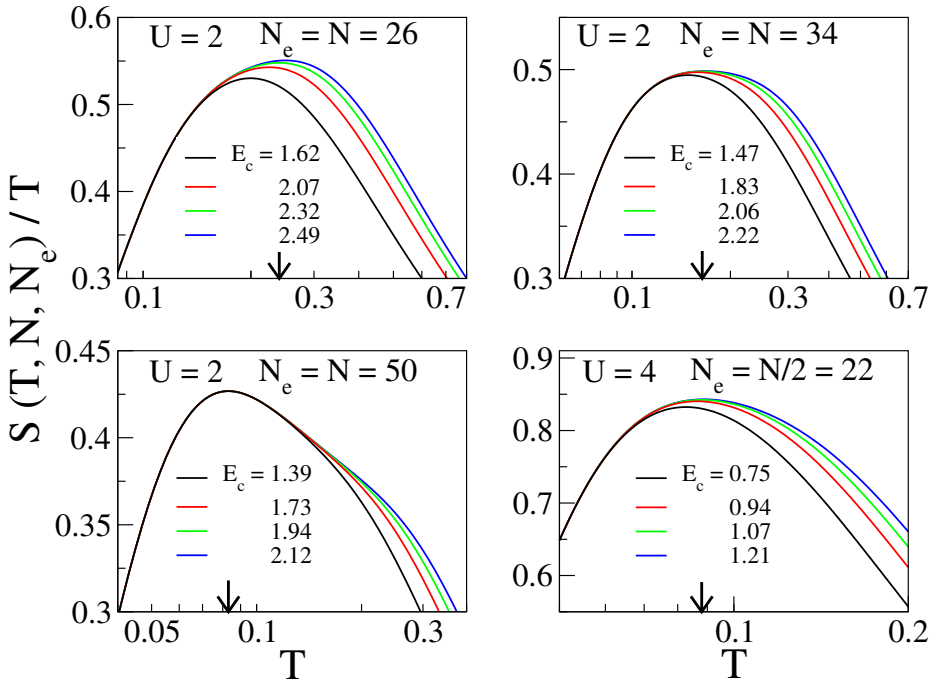

Figure 5.4: Dependence of truncated $S(T, N, N_e)/T$ in the energy cutoff E_C in systems with N sites, N_e electrons, $V = 0$ and U in Eq. 5.1. The arrows mark $T(N)$, the maximum of $S(T, N, N_e)/T$ for E_C corresponding the green curves.

We seek a cutoff $E_C(N, N_e)$ at system size N and retains all states $R(N, N_e)$ with $E_p(N, N_e) \leq E_C(N, N_e)$. The cutoff must be high enough to suppress finite-size effects and yet low enough for the truncated spectrum to return converged thermodynamics in a narrow range $T(N)$ at each system size.

We typically increase $E_C(N, N_e)$ to include $200 - 300$ states in the $S^Z = 0$ sector that contains the ground state. $R(N, N_e)$ is three or four times larger due to contributions from sectors with Zeeman degeneracy $2S+1$. The truncated entropy $S_C(T, N, N_e)$ has $E_j(N, N_e) \leq E_C(N, N_e)$ in Eq. 5.8. The cutoff criterion [81] is to converge or almost converge the maximum of $S_C(T, N)/T$. Fig. 5.4 shows the dependence of $S_C(T, N, N_e)/T$ on $E_C(N, N_e)$ for representative cases, three panels with $N_e = N$ and one with $N_e = N/2$. As expected, convergence to $S_C(T, N, N_e)$ is excellent at low T. Once reached, the maximum $T(N)$ marked by arrows becomes insensitive to additional increase of the cutoff.

Table 5.5: Number of states $R(N, N_e)$ in systems with $N_e = N$ electrons, $U = 2$ and $V = 0$ up to the cutoff $E_C(N)$. $\Delta(N)$ is the finite size gap; $T(N)$ is discussed in the text.

N	$T(N)$	$E_C(N)$	$R(N, N_e)$	$\Delta(N)$
14	0.490	3.03	927	0.537
18	0.320	2.7	591	0.416
22	0.271	2.42	481	0.342
26	0.240	2.32	402	0.292
30	0.195	2.1	501	0.245
34	0.164	2.06	532	0.217
50	0.083	1.94	611	0.143
66	0.056	1.92	713	0.106

The cutoffs used in most of the following calculations are the green curves in Fig. 5.4, the second highest E_C. Table 5.5 lists $E_C(N, N_e)$, $T(N)$ and $R(N, N_e)$. Higher E_C is an option but is time intensive. As also found for noninteracting fermions in Table 5.2, Table 5.3 and Table 5.4, $T(N)$ is close to the finite size gap $\Delta(N)$ at system size N. Convergence to the thermodynamic limit requires, quite reasonably, $T(N) \sim \Delta(N)$. The DMRG excitations are the most accurate in this range. With $E_C/T(N) \sim 10$ at $U = 2$ in Table 5.5, the Boltzmann factors of neglected states are less than 5×10^{-5} and are also small for less accurate excitations close to the cutoff.

We obtain the thermodynamic limit $S(T, n)$ by interpolation of DMRG results. $S(T)$ is initially linear in T in gapless models. Its thermodynamic limit at high T is given by $S_\lambda(T, N)$ in Fig. 5.2, inset. DMRG yields $S_\lambda(T, N)$ up $T(N)$ when the spectrum is truncated at E_C. At intermediate T, we interpolate $S_\lambda(T, N)$ between higher T and lower T. Convergence to $S(T, n)$ is from below for $N = 4p + 2$. It follows that $S(T, n)$ is given by $S_\lambda(T, N, N_e)$ with progressively larger N at lower T.

The upper panel of Fig. 5.5 shows $S_\lambda(T, N, N_e)$ for $U = 0$ and $N_e = N$ up to $T = 1$, beyond which ED returns the thermodynamic limit. The solid red line is the band limit. The inset zooms in on $T \leq 0.1$. The $N \leq 14$ curves are ED and converge from above (below) for $N = 4p$ $(4p + 2)$. The $N = 4p + 2$ systems are lower bounds. The color-coded points indicate the system sizes that gives the calculated $S(T)$ shown in the lower panel. Agreement with the band limit is almost quantitative; the largest difference in Fig. 5.5 is 0.006. The entropy derivative is $S'(T) = C(T)/T$ where $C(T)$ is the specific heat per site. The calculated $S'(T)$ is compared in the lower panel to the band limit, offset by 0.10.

The entropy analysis in Fig. 5.5 came as a surprise. With good reason, deviations from the thermodynamic limit have been associated with finite size gaps. That remains the case for spin chains, which have

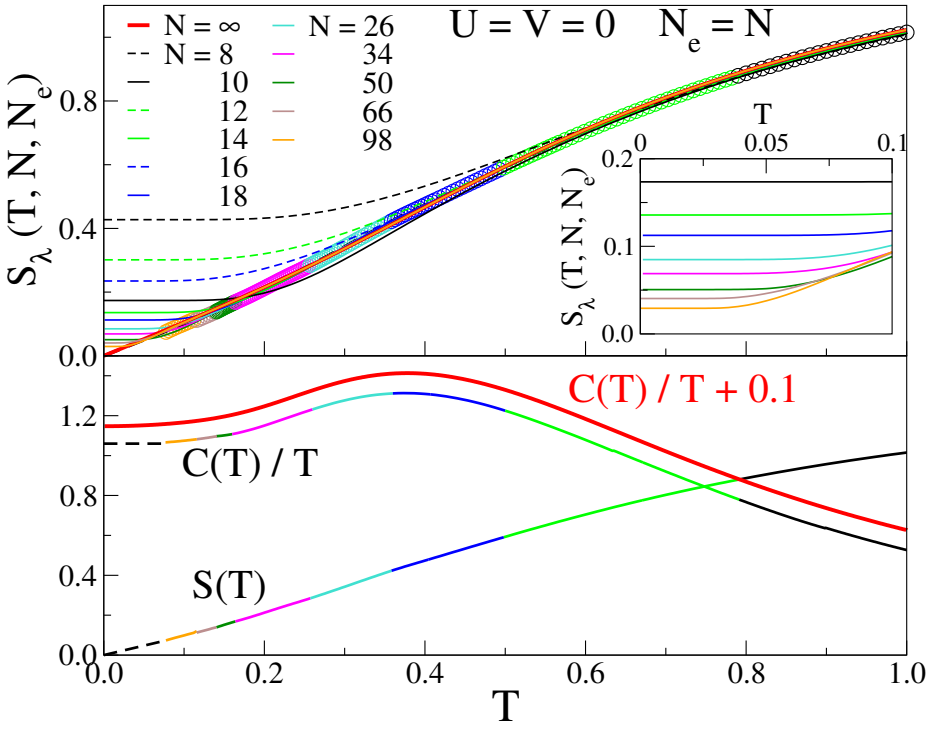

Figure 5.5: Upper panel: Scaled entropy $S_\lambda(T, N, N_e)$ per site at $T < 1$ for $N = N_e$ and $U = V = 0$ in Eq. 5.1. The full red line is the band limit. The color coding indicates the system size that approximates the thermodynamic limit. The inset zooms in on $T \leq 0.1$. Lower panel: The calculated $S(T)$ and its derivative $S'(T) = C(T)/T$; the band limit $C(T)/T$ is offset by 0.10 for clarity.

indeed been modeled the most. However, the size dependence of the many-fermion basis is just as important as gaps for the entropy or free energy of fermionic models. Scaling the partition function by $\lambda(N, 1)$ to ensure the proper high T limit shifts the $S(T, N, N)$ curves to $S(T)$ at progressively lower T with increasing N.

The ED/DMRG procedure illustrated above for $U = 0$ and $N_e = N$ is accurate down to at least $T \sim 0.03$ for both $\chi(T)$ in Fig. 5.1 and for $S(T)$ and $S'(T)$ in Fig. 5.5. The method tends to perform better in models with less dramatic $N_e = 4p, 4p + 2$ variations. Larger systems are computationally more demanding. The actual limit [81] is set by the accuracy of the dense spectrum of large systems, which is highly model dependent.

5.3 Representative results

We apply the ED/DMRG method to fermionic models such as Eq. 5.1 and seek accurate low T thermodynamics. The large U limit of half-filled models leads to spin-1/2 chains, Eq. 5.4, that can also be treated

using ED/DMRG. We focus on the molar magnetic susceptibility $\chi(T)$ and entropy $S(T)$ per site. Gapless systems have finite $\chi(T)$ and $S'(T)$ at $T = 0$ while gapped systems have $\chi(0) = S'(0) = 0$ and $E_{ST} > 0$ to the lowest triplet. Finite systems with a singlet ground state and periodic boundary conditions have decreasing $E_{ST}(N)$ with N. It follows that $\chi(T, N_e)$ converges to $\chi(T, n)$ from below for $N_e = 4p + 2$,

$$\chi(T, N_e) \leq \chi(T, n) . \tag{5.13}$$

The ED/DMRG line in the lower panel of Fig. 5.1 is based on the crossing or merging points T_N of $N = 4p, 4p + 2$ susceptibilities. The 96/98 curves cross at $T_{98} = 0.118$, slightly below the $\Delta(T, 98)/T$ maximum at $T(98) = 0.14$. The calculated $\chi(T)$ based on $\chi(T, 4p + 2)$ and Eq. 5.13 is closely similar, with maximum deviation of 3×10^{-4} at $T = 0.13$ or 0.27. We use both merging points and $4p + 2$ convergence in the following.

5.3.1 Hubbard model, $U < 4$

We start with half-filled Hubbard models with $U \leq 4$, less than or equal to the bandwidth, and $V = 0$ in Eq. 5.1. Fig. 5.6, upper panel, shows $\chi(T, N)$ at $U = 2$ using ED up to $N = 12$ and DMRG for larger systems. The notation follows Fig. 5.1. The bold dashed line is the thermodynamic limit $\chi(T, U)$ inferred from the indicated merging points. Since the ground state is a singlet for $U > 0$, small $N = 4p$ systems merge from above as in the band limit. The $\chi(T, 4p)$ maxima due to finite size decrease and almost disappear by $N = 144$. The $N = 4p+2$ curves that converge from below yield accurate $\chi(T)$ to $T \sim 0.02$ or less for $N = 146$, well below the 144/146 merging point.

The lower panel presents calculated $\chi(T, U)$ at $U = 0$, 1, 2 and 4. The arrows mark the exact $\chi(0, U)$ obtained analytically by Takahashi [14]. All $\chi(T, N)$ increase with N at $U = 4$ and converge from below to $\chi(T)$. Finite $U > 0$ increases $\chi(T, U)$ at low T since the ground and low-energy states have reduced contribution from doubly and unoccupied sites, still appreciable at $U = 4$, whereas spin chains have exclusively singly occupied sites. The exchanges in Eq. 5.3 at $U = 4$ are $J_1 = 3/4$ and $J_2 = 1/16$. ED for $N = 24$ gives the spin $\chi(T)$ shown as a dashed line in the lower panel for $T > 0.09$ where the thermodynamic limit holds. Sites with $n_r = 2$ or 0 reduce $\chi(T, U)$ at low T. The reduction becomes negligible by $U = 8$ where the linear HAF with $J_1 = 1/2$ and $J_2 = 0$ is almost quantitative. Exact HAF results have

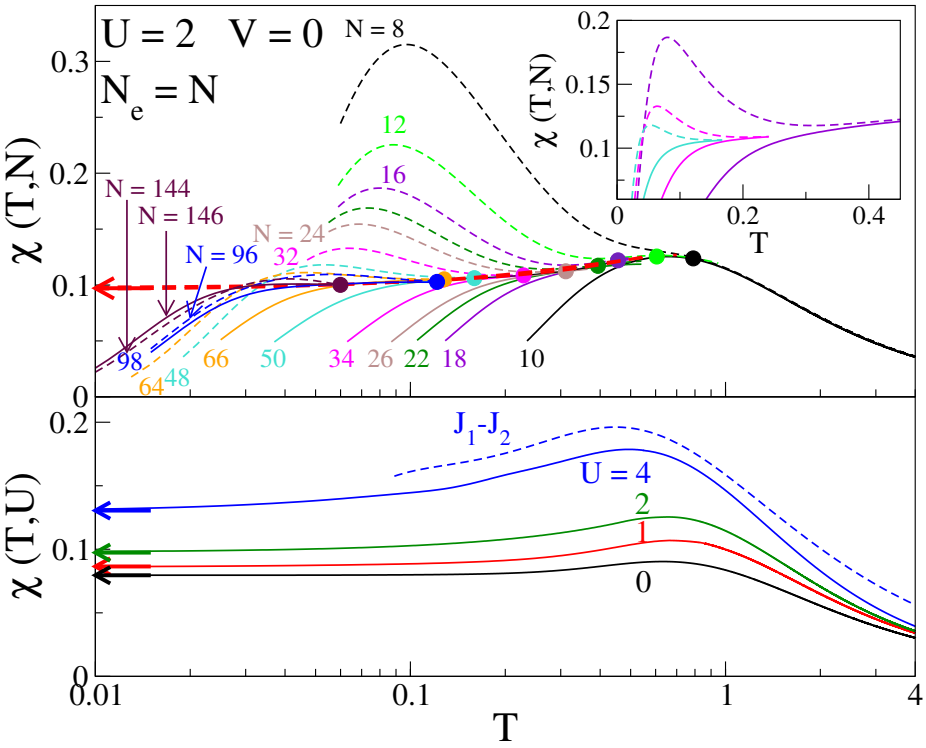

Figure 5.6: Upper panel: Same as Fig. 5.1 for $U = 2$ instead of $U = 0$; $\chi(T, N)$ for $N = 4p$, $4p + 2$ merge at the indicate points that give $\chi(T, U)$ in the thermodynamic limit. The inset shows the merging of $N = 16/18$, 32/34 and 48/50. Lower panel: $\chi(T, U)$ at $U = 0$, 1, 2 and 4. The arrows in both panels are exact $\chi(0, U)$ from Ref. [14]. The dashed line is ED for $N = 24, J_1 = 3/4$ and $J_2 = 1/16$ in Eq. 5.4.

long been used to benchmark numerical methods.

Fig. 5.7, upper panel, shows $S_\lambda(T, N)$ at $U = 2$ and $T \leq 0.4$ for the indicated system sizes. ED at $N = 10$ and 12 for the scaled entropies converge to $S(T, U)$ for $T > 0.4$ as shown in Fig. 5.2, inset, for $U = 0$. Small $N = 4p$ gaps initially increase the entropy. As in Fig. 5.5, the thermodynamic limit $S(T, U)$ is color coded according to the system size that contributes at T. Systems up to $N = 98$ determine $S(T, U)$ directly for $T > 0.06$ and by extrapolation at lower T.

The lower panel of Fig. 5.7 compares the calculated specific heat $C(T, U) = TS'(T, U)$ at $U = 0$, 2 and 4. The dashed line for $T > 0.09$ is the spin chain, Eq. 5.4, with $J_1 = 3/4, J_2 = 1/16$ at $U = 4$. Its $C(T)$ maximum is exclusively due to spins. The $C(T, U)$ maxima for $U = 0$ and 2 have contributions from spin, charge and combined excitations. Increasing U shifts charge excitations to higher energy, thereby reducing the maximum. Combined spin and charge excitations lead to the broad $C(T, 4)$ curve. We include the TMRG curve at $U = 8$ from Ref. [15] that illustrates spin-charge separation. As discussed in Section 5.3.2, ED for $N = 8$ or 10 at $U = 8$ also returns two $C(T)$ peaks. The low T thermodynamics at

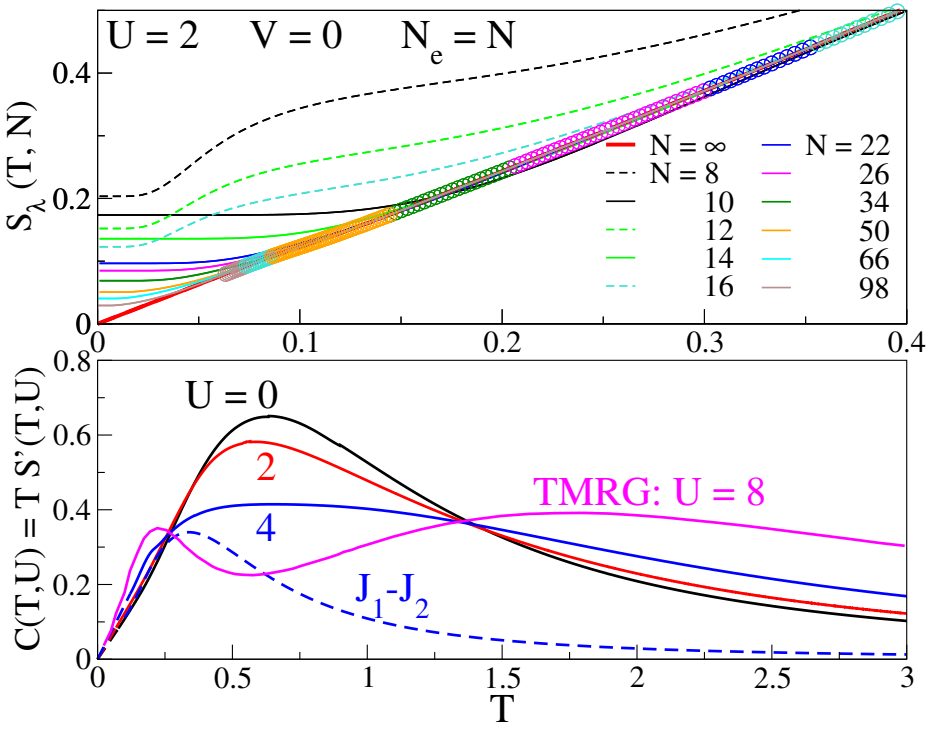

Figure 5.7: Upper panel: Scaled entropy $S_\lambda(T, N)$ per site at $T \leq 0.40$ for $N = N_e$ and $U = 2$, $V = 0$ in Eq. 5.1. The full red line is the band limit. The color coding indicates the system size that approximates the thermodynamic limit. Lower panel: The calculated $C(T, U) = TS'(T, U)$ at $U = 0$, 2 and 4. The dashed $J_1 - J_2$ line is ED for 24 spins with exchanges at $U = 4$ in Eq. 5.3. The TMRG curves at $U = 8$ is from Ref. [15].

$U \geq 4$ are more reliably based on spin chains, Eq. 5.4, even though it only becomes truly quantitative in the large U limit.

5.3.2 Spin-charge separation, $U > 4$

The spin-1/2 chains in Eq. 5.4 describe the thermodynamics of Eq. 5.1 in half-filled systems with $U > 4$ or $U - V > 4$ when interactions exceed the bandwidth $4t$. The atomic limit $U \to \infty$ has noninteracting spins with Curie susceptibility of $\chi_{Curie}(T) = 1/4T$ while the band limit is $1/8T$ since half of the sites are singly occupied at high T.

The $U = 0$ line in Fig. 5.8 is $T\chi(T)$, the band limit in Eq. 5.2, that increases monotonically to $1/8$. The $U = 4$ line is the thermodynamic limit $T\chi(T, U)$ from Fig. 5.6, lower panel. The maximum at $T \sim 1.8$ is due to spin excitations. The full and dashed lines at $U = 8$ and 16 are $T\chi(T, U, N)$ at system sizes $N = 8$ and 10. The maxima become more pronounced and shift to lower energy. Finite size effects are evident at both low and high T where we have $T\chi(T) > 1/8$ because $\rho_1(N) > 1/2$ as discussed in connection

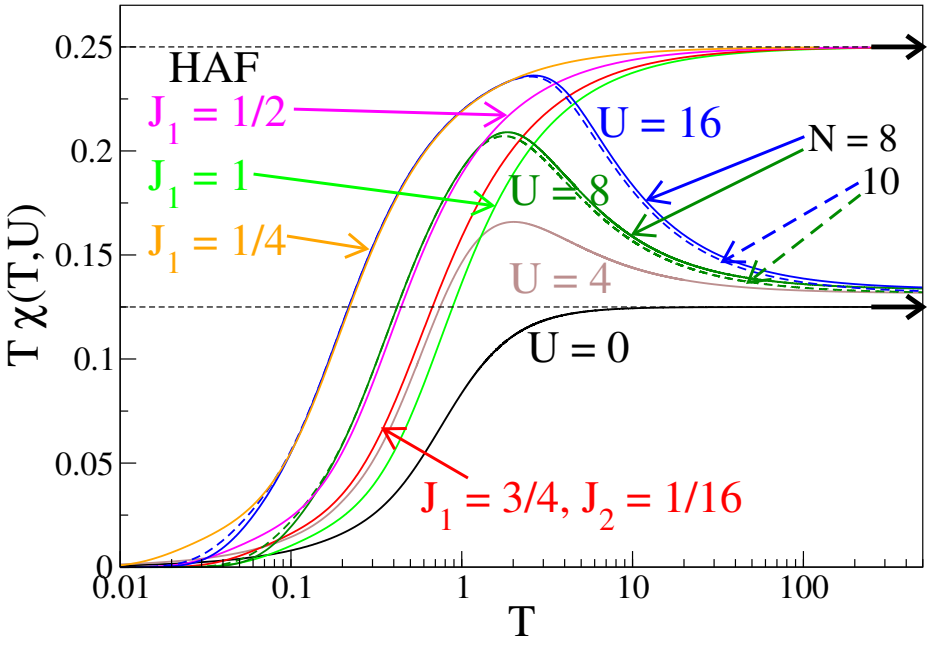

Figure 5.8: Calculated $T\chi(T, U)$ at $U = 0$ (band limit) and 4 in the thermodynamic limit and at $U = 8$ and 16 for $N = 8$ and 10. The spin chains with $T\chi(T) \to 1/4$ at high T are ED for 24 spins: HAFs with $J_1 = 1$, 1/2 and 1/4 and the $J_1 - J_2$ model with $J_1 = 3/4, J_2 = 1/16$.

with Fig. 5.1. The ED/DMRG method is not applicable to systems with spin-charge separation because the thermodynamic limit can be reached at $T < 0.1$ but not at $T > 1$. The low-energy states accessible by DMRG limit convergence to $T \leq T(N) < 1/2$ in Table 5.5.

We turn instead to spin chains and ED for $N = 24$ spins in Eq. 5.4 to compute $T\chi(T)$. The thermodynamic limit holds for $T > 0.1$ before any DMRG calculation. The exchanges are $J_1 = 3/4$ and $J_2 = 1/16$ at $U = 4$. To lowest order in $(t/U)^2$, we have $J_2 = 0$ and an HAF with $J_1 = 1$. The impact of J_2 on $T\chi(T)$ is evident in Fig. 5.8. The HAF substantially underestimates the $U = 4$ susceptibility at low T while the $J_1 - J_2$ model slightly overestimates it as has already been noted. The HAF has $J_1 = 1/2$ and 1/4 at $U = 8$ and 16, respectively, where J_2 is negligible; it accounts very well for $T\chi(T)$ in Fig. 5.8 between $T = 0.1$ and 1. Spin excitations of order $1/U$ are increasingly well separated from charge excitations of order U.

Charge degrees of freedom contribute directly to the entropy of Hubbard models. The contrast with spin chains is equally prominent. Fig. 5.9 shows the band limit and exact $S(T, U, N)$ curves with $U = 8$ and 16 at system sizes 8 and 10. Finite size effects are again seen at both low and high T. Convergence to $2 \ln 2$ requires the scaled entropy discussed in Section 5.2. The HAF with $J_1 = 1/2$ and 1/4, respectively, fits $S(T, U, N)$ in the intervals $0.12 < T < 0.9$ at $U = 8$ and $0.08 < T < 1.4$ at $U = 16$. The spin chain

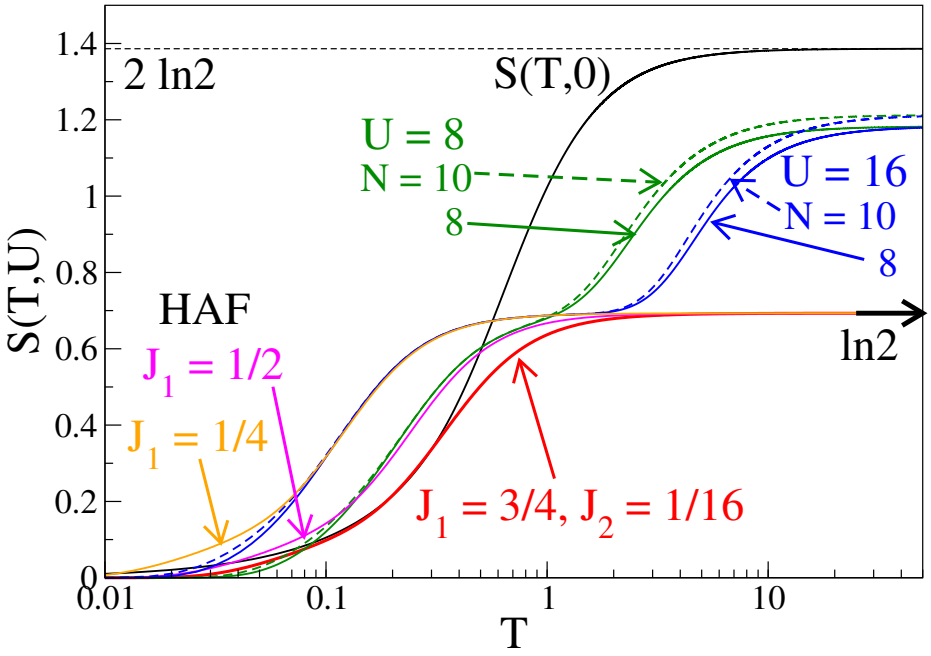

Figure 5.9: Calculated $S(T, U, N)$ at $U = 8$ and 10 at system sizes 8 and 10; the band limit is $S(T, 0)$. The spin $S(T)$ are HAFs with $J_1 = 1/4$ and 1/2, and the $J_1 - J_2$ model with $J_1 = 3/4, J_2 = 1/16$.

gives the thermodynamic limit to much lower T when combined with DMRG for $N > 24$.

The band entropy $S(T, 0)$ in Fig. 5.9 is surprisingly close to the spin entropy of the $J_1 = 3/4, J_2 = 1/4$ chain up to $T \sim 0.3$. Finite U initially shifts spin excitations to lower energy and charge excitations to higher energy. Offsetting entropy changes are a qualitative explanation for similar $S(T, U)$ at low T for $U = 0$ and 4. By inspection, the derivative $S'(T, U, N)$ at $U = 8$ or 16 has two maxima separated by a minimum that is close to zero around $T \sim 1$ and widens with increasing U. Hence $C(T, U, N) = TS'(T, U, N)$ also has two maxima.

Spin-charge separation at $U = 8$ was highlighted in the exact thermodynamics of the half-filled Hubbard model [160]. The exact $\chi(T, 8)$ and $C(T, 8)$ are used in Ref. [15] to demonstrate the impressive accuracy of TMRG down to $T \sim 0.1$ and to emphasize that the method is applicable to models whose exact thermodynamics is not known. We make exactly the same case for ED/DMRG and the low T thermodynamics that is less or not accessible to TMRG.

5.3.3 Quarter-filled models

We consider Eq. 5.1 with $N_e = N/2$ electrons or holes. Exact thermodynamics are readily obtained in the band limit ($U = V = 0$). Shiba [16] reported the $T = 0$ susceptibility $\chi(0, U, n)$ at any U or filling n and

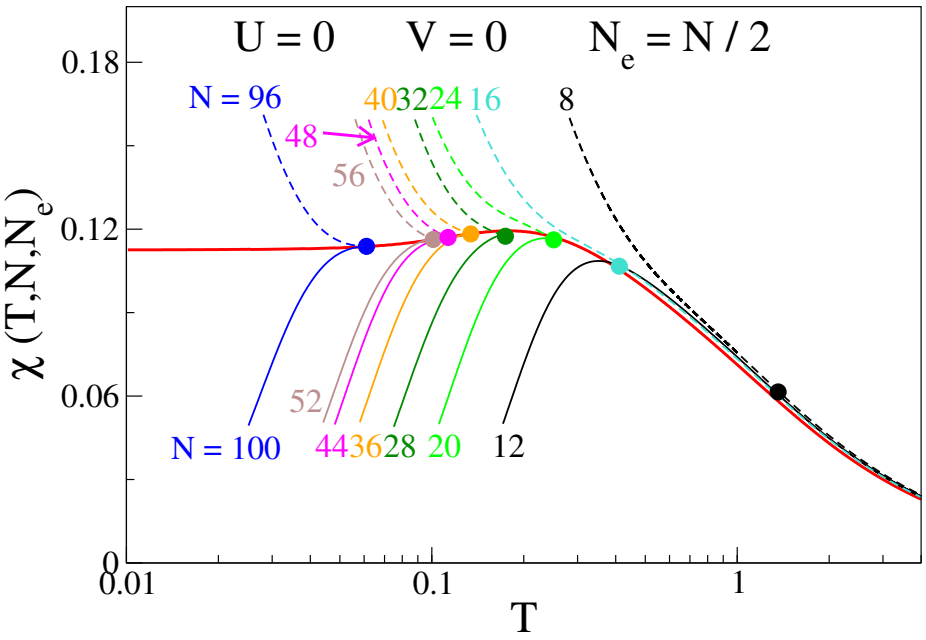

Figure 5.10: Susceptibility $\chi(T, N, N_e)$ of quarter-filled models with $U = V = 0$ in Eq. 5.1. The points are the merging of $N_e = 4p, 4p + 2$ lines and define the thermodynamic limit as discussed in Fig. 5.1 for half-filled models. The red line is the exact band limit $\chi(T, 1/2)$ for noninteracting fermions.

$V = 0$.

Fig. 5.10 compares the band limit $\chi(T)$ to $\chi(T, N)$ at $n = 1/2$ using the notation in Fig. 5.1. The $T = 0$ susceptibility is $\sqrt{2}$ larger and the $\chi(T)$ maximum is at lower T. Finite systems with $N_e = 4p$ and $4p + 2$ converge from above and below, respectively, for $N = 2N_e$. ED up to $N = 16$ deviates upward at high T where the thermodynamic limit of the fraction of singly occupied sites is $\rho_1(n) = n(1 - n/2) = 3/8$. The fraction $\rho_1(N, N/2)$ follows from Eq. 5.5

$$\rho_1(N, N/2) = \sum_{q=0}^{N/4} \left(\frac{N - 4q}{2(N - q)} \right) W(q, N, N/2)/W(N, N/2). \tag{5.14}$$

We obtain $\rho_1(N, N/2) = 0.4085$ and 0.4063 at $N = 12$ and 16. DMRG calculations lead to $\chi(T, N)$ curves $N, N+4$ that merge at points that define the thermodynamic limit as discussed in connection with half-filled systems. The accuracy at quarter filling is quite comparable to half filling.

Fig. 5.11 has EHM results for $\chi(T, N)$ with $U = 4$, $N_e/N = 1/2$ and $V = 0, 2$ and 4. ED to $N = 12$ is followed by DMRG to $N = 100$. The upper panel has $V = 2$ and shows the merging points of systems

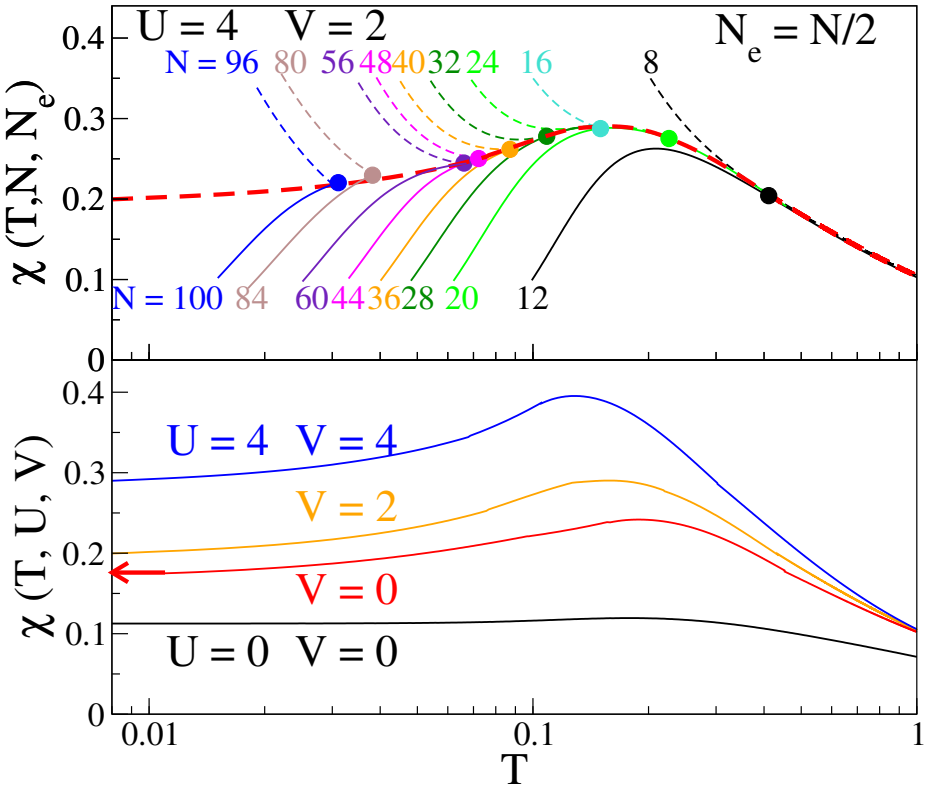

Figure 5.11: Upper panel: $\chi(T, N, N_e)$ of quarter-filled models with $U = 4$, $V = 2$ in Eq. 5.1. The points are the merging of $N_e = 4p, 4p+2$ lines that generate the thermodynamic limit shown a red dashed line. Lower panel: Thermodynamic limit of quarter-filled models at the indicated U, V. The arrow at $\chi(0)$ is exact [16].

with $N_e = 4p$ and $4p + 2$. The thermodynamic limit is the bold dashed red line. The same construction gives the thermodynamic limit of $\chi(T)$ in the lower panel for the indicated U, V and the band limit. The arrow marks [16] the exact $\chi(0)$. Increasing either U or V increases the susceptibility by reducing the density of doubly occupied diamagnetic sites or by reducing the density of adjacent singly occupied sites that form singlet pairs. The large U, V limit at quarter filling has $n_r = 1$ at every other site. The system has a singlet ground state, weak AFM interactions and a charge gap.

Arbitrary filling poses difficulties for ED/DMRG. Since the ground state of Eq. 5.1 is a singlet for the parameters of interest, the relevant finite systems must have integral N and even N_e. ED for $N_e = 4$ and 6 is minimally required to demonstrate convergence at high T, and adding two electrons sets the minimum increase of the system size N. The method calls for highly commensurate N_e, N such as half or quarter filling. For example, either sublattice of TTF-TCNQ has $n \sim 0.6$. The smallest system has 6 electrons on 10 sites, suitable for ED. The next smallest are 12/20, 18/30, ... On the other hand, small variations of $n = N_e/N$ such as 8/13 or 10/17 may nevertheless provide useful approximations.

5.3.4 BOW PHASE

The quantum phase diagram of the half-filled EHM illustrates competition among on-site repulsion U, nearest-neighbor interaction V and electron transfer t. As predicted by Nakamura [36], intermediate U leads to a narrow bond-order-wave (BOW) phase with a finite singlet-triplet gap E_{ST} and doubly degenerate singlet ground state. Ongoing studies discuss BOW properties of the EHM and related models [37] with other intersite interactions in Eq. 5.1. The quantum critical points V_s and V_c at the BOW boundaries are estimated in finite systems using level crossing [164]. For constant $U < 7$ and $N = 4p$, the EHM has $E_{ST}(4p) = E_\sigma(4p)$ at $V_s(4p) < U/2$, where $E_\sigma(4n)$ is the gap between the lowest two singlets, and $E_\sigma(4p) = E_J(4p)$ at $V_c(4p) > U/2$, where $E_J(4p)$ is the gap to the lowest singlet with opposite electron-hole symmetry to the ground state. The weak size dependence of the critical points allows accurate extrapolation to the thermodynamic limit as discussed [30, 49] for the quantum critical point $J_2/J_1 = 0.2241$ of the spin chain, Eq. 5.4.

Sirker et al. reported [15] a comprehensive TMRG study of the thermodynamics of the half-filled EHM, including $U = 4$ and variable V. They find $V_c = 2.165$, fully consistent with level crossing, and note that thermodynamics does not determine $V_s = 2.02 \pm 0.06$ accurately. The charge gap $E_J(V)$ vanishes at the boundary V_c between the BOW and the charge-density-wave (CDW) phases. Level crossing returns $V_s \sim 1.86$ for the Kosterlitz-Thouless transition where an exponentially small $E_{ST}(V)$ opens. We compare below ED/DMRG results for $\chi(T)$ for $U = 4$ and variable V with TMRG results in Fig. 13 of Ref. [15].

Fig 5.12 shows $\chi(T, N)$ of gapped models: $V = 2.20$ in the upper panel is just above V_c while $V = 2.15$ in the lower panel is in the BOW phase. The points indicate the merging of $\chi(T, N)$ for $N = 4p, 4p + 2$ using DMRG for $N \geq 14$ and ED for $N = 8, 10$ and 12. Here the strong $4p$, $4p + 2$ dependence is due $E_\sigma(4p) = 0$ at $V_1(4p)$, but there is no such degeneracy for $4p + 2$. The roles are reversed for antiperiodic boundary conditions [164], when $E_\sigma(4n + 2) = 0$ at $V_1(4p + 2)$. The thermodynamic limit is reached at $N > 1/E_{ST}$ when finite size effects become small compared to $E_{ST}(V)$. The $V = 2.20$ panel shows almost converged $\chi(T, 4p)$ at low T at system size $4p = 48$; this is an accurate lower bound on $\chi(T)$ at $V = 2.20$. The smaller gap in the $V = 2.15$ panel is evident from the $\chi(T, 4p)$ size dependence up to $4p = 64$. We estimate that convergence to $\chi(T)$ requires $4p \sim 100$.

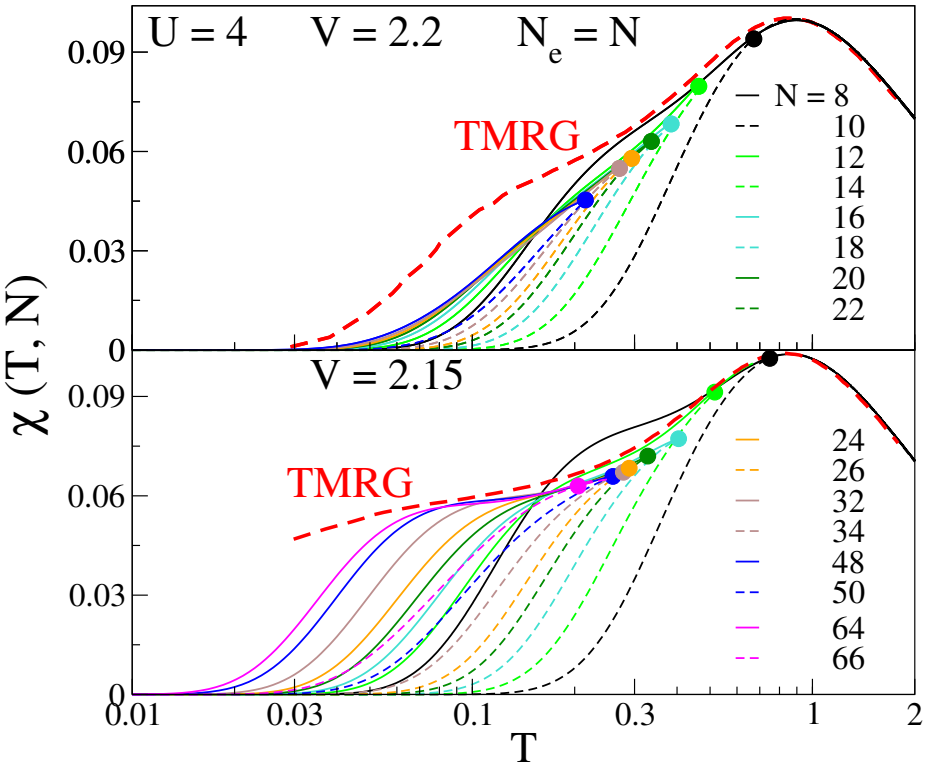

Figure 5.12: Susceptibilities $\chi(T, N)$ of half-filled EHM with $U = 4$ and $V = 2.20$ (upper panel) and $V = 2.15$ (lower panel) and merging points $N = 4p, 4p + 2$. The TMRG curves are from Fig. 13 of Ref. [15].

TMRG substantially overestimates $\chi(T)$ at $V = 2.20$ for $T < 0.8$ because the reported [15] $E_{ST} = 0.11$ is smaller than 0.182 obtained by DMRG and $1/N$ extrapolation of $E_{ST}(N)$ up to $N = 100$. TMRG at $V = 2.15$ and the slight downturn of $\chi(T)$ is the first indication of finite $E_{ST} = 0.039$, again smaller than 0.065, the extrapolated DMRG gap. There is fair agreement for $T > 0.1$ and good agreement in both panels for $T > 0.5$.

We also studied $V = 1.80$ in the gapless phase and $V = 2.05$ in the BOW phase. Agreement with TMRG is good at $T > 0.1$ in both cases. The $\chi(T, U, V)$ curves in Fig. 5.13 are based on ED at high T and the DMRG merging points at low T, as shown Fig. 5.12 for $V = 2.15$ and 2.20, and in Fig. 5.6 for $U = 2$, $V = 0$. Increasing V decreases $\chi(T, 4, V)$ by raising the energy of adjacent $n_r = 1$ sites. Since the EHM has some resemblance to a Hubbard model with $U_{eff} = U - V$, similar $\chi(T, U, V)$ at $T > 1$ is as expected.

The low T behavior in Fig. 5.13 are quite different. The $V = 1.80$ results for $\chi(T, N)$ have $4p, 4p + 2$ patterns similar to those in the upper panel of Fig. 5.6 for $U = 2$, $V = 0$. Convergence occurs at smaller system size 48/50. Extrapolation gives finite $\chi(0)$ in gapless systems. As noted above, $N = 48$ is close to

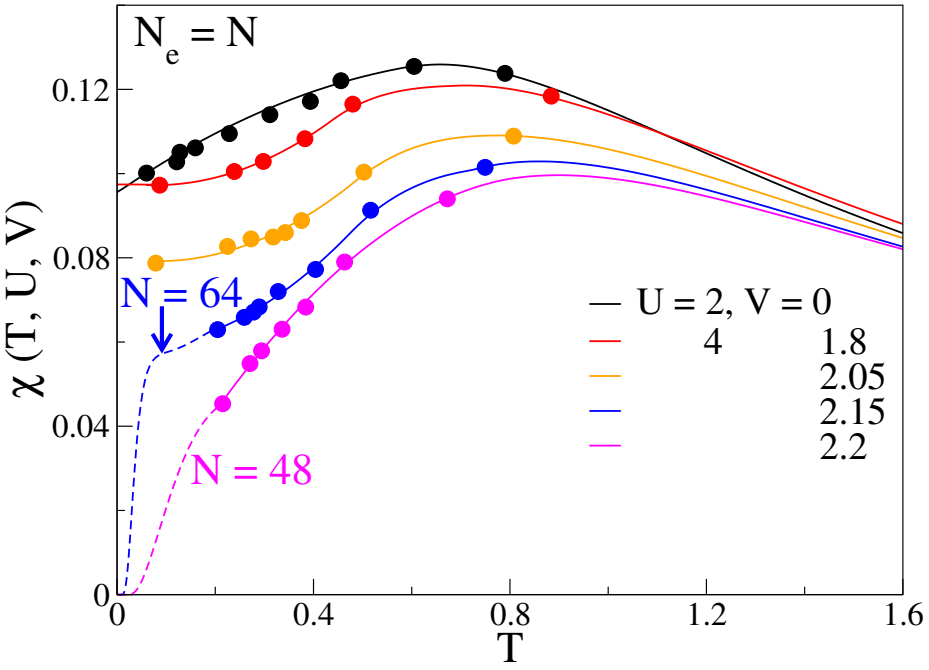

Figure 5.13: Thermodynamic limit of $\chi(T, U, V)$ inferred from DMRG calculation with $N = 4p, 4p + 2$ merging points shown and discussed in the text; ED give higher T. The dashed $V = 2.20$ and 2.15 lines are based on $N = 48$ and 64, respectively. Gapless models have $\chi(0, U, V) > 0$. The small gap for $V = 2.05$ requires larger systems.

the thermodynamic limit at $V = 2.20$ while $N = 64$ is a lower bound at $V = 2.15$. The sharp initial increase of $\chi(T)$ is governed by finite E_{ST}. Accordingly, the tiny gap at $V = 2.05$ presumably leads to an even more abrupt $\chi(T)$ rise in Fig. 5.13 to the $\chi(T) \sim 0.08$ plateau in systems of several hundred sites. Exponentially small E_{ST} at V slightly larger than V_s is not relevant to the thermodynamics except at exponentially low T.

The calculated $\{E(N)\}$ that return $\chi(T, U, V)$ also yield $S(T, U, V)$ as shown in Figs. 5.5 and 5.7 using the scaled entropy of finite systems. The entropy at $T \sim 1$ is roughly 75% of the high T limit, consistent with a single energy scale in systems with comparable bandwith, U and V. The $T > 0.4$ range is given by ED for $N = 10$. DMRG for larger $N = 4p + 2$ systems gives $S(T, N)$ down to $T \sim 0.1$. We fit the $T < 0.4$ results for $S(T, U, V)$ to a 4th order polynomial and differentiate to obtain the $S'(T, U, V) = C(T, U, V)/T$ curves in Fig. 5.14 for the same systems as in Fig. 5.13. The gapless $V = 1.80$ and Hubbard curves are extrapolated to finite $S'(0)$. Extrapolation of gapped systems with $S'(0) = 0$ requires larger systems. In contrast to $\chi(T, U, V)$, we find similar $S'(T, U, V)$ for the EHMs and clear differences with the Hubbard curve.

Since the area under $S'(T, U, V)$ curves is $2 \ln 2$ in half-filled systems, the $U = 2$, $V = 0$ maximum at

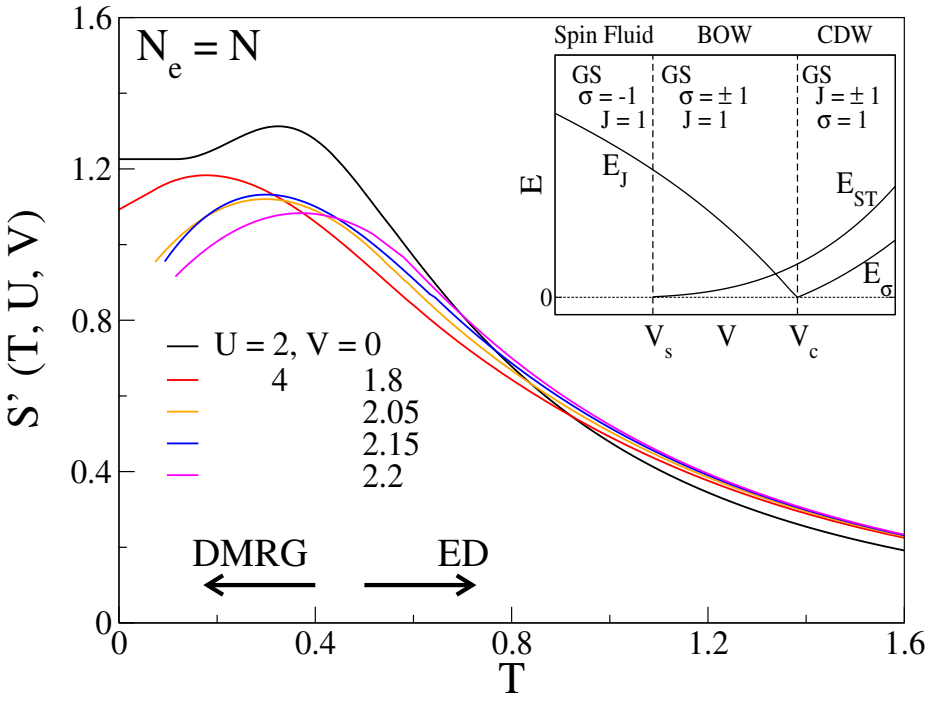

Figure 5.14: Thermodynamic limit of entropy derivative $S'(T,U,V) = C(T,U,V)/T$ inferred from DMRG calculations at $T < 0.4$ discussed in the text and ED at higher T. The inset shows the BOW boundaries V_s and V_c, the ground state degeneracy and the spin and charge gaps.

$T \sim 0.4$ is offset by lower $S'(T,2,0)$ at $T > 0.8$. The small $S'(T,4,V)$ differences among EHM curves are largely compensated by $T \sim 1$. As sketched in the inset, the charge gap is less than E_{ST} on either side of $V_c = 2.165$. The ground state is nondegenerate in the gapless phase with $V < V_s$ and doubly degenerate in the gapped BOW and CDW phases. The smallest gap governs the low T entropy while the susceptibility depends on the spin gap. We understand why there are spin gaps at $V = 2.20$ and 2.15 in Fig. 5.13 but do not see a charge gap in Fig. 5.14 at system sizes 48 and 64, respectively, for $V = 2.20$ and 2.15.

5.4 Discussion

We have applied the ED/DMRG method to the low T thermodynamics of representative 1D fermionic models. The method is general. The diagonalization of the superblock is the most time-intensive step at each cycle of DMRG calculations. The computational cost for obtaining the lowest few eigenvalues goes as $O(m^3)$ where m (here 500) is number of eigenvectors of the density matrix corresponding to largest eigenvalues kept in the calculation. The time increases linearly with system size since the dimension of the superblock matrix in Section 5.2.2 is kept constant. The system size is limited by the numerical accuracy

required for the dense low-energy spectrum $\{E(N)\}$, which is of course highly model dependent. Hence the lowest accessible T depends on the model as well as on effort. It is in the range $0.01 < T/t < 0.05$ for the illustrative systems in Section 5.3 and extrapolation to lower T is often possible.

Fermionic models are more complex than spin chains. The energy spectrum $\{E(N)\}$ of fermionic systems depends on the filling $n = N_e/N$ as well as the system size in models with $W(N, N_e)$ states. The scaled partition function in Section 5.2.1 increases $W(N, N_e)$ by the factor $\lambda(N, n)$ in Eq. 5.7 that involves counting and holds for arbitrary interactions. As noted in Section 5.2, ED/DMRG is not exact at high T due to the size dependence of the basis. Its accuracy is shown by comparisons to the band limit or to exact $T = 0$ results at half and quarter filling. The method is limited to models with one energy scale and is best suited for commensurate $n = 1$ or $1/2$.

The low T thermodynamics are obtained by independent calculations on increasingly large systems. We have exploited systematic variations with N and convergence to the thermodynamic limit from above or below with increasing T. Explicit results for finite systems provide some clues about the largely unknown spectrum $\{E(N)\}$ of correlated states. Extrapolations based on systems size have been widely used from the outset.

6
Conclusion

The quantum many body model Hamiltonians plays a vital role in modeling electronic properties and understanding exotic phases in condensed matter systems. Unfortunately, obtaining exact ground state properties of these systems is either very difficult or impossible in most of the cases due to many body nature of systems. In these systems, the exponential rise of the Hilbert space dimension with system size N is a major issue for the numerical solution since the computational cost of diagonalization of Hamiltonian matrix of size $m \times m$ goes as $O(m^3)$. To analyse the experimental findings which are obtained at finite T, the full spectrum and their wavefunctions of the model Hamiltonians are required. Several numerical methods are available in literature to solve the thermodynamic properties of these correlated systems, but each of these methods has their own limitations. For example, exact diagonalization numerical technique is restricted to small system sizes, whereas the quantum Monte Carlo, although is capable to solve large system sizes, has sign problem with frustrated spin systems and fermionic systems away from half filling. Motivated by the need for a general method to solve eigenvalues and eigenvectors of a low dimensional quantum many body Hamiltonian, we have developed a hybrid ED/DMRG approach to calculate the thermodynamical properties of quantum many body model systems. We have also demonstrated its efficiency to access the finite T properties for both spin and fermionic model Hamiltonians.

The hybrid method has two main aspects: first, the high-T properties are calculated from small systems using the ED as the thermal fluctuation at finite T tends to diminish the correlation between electrons.

At very high T, the correlation length is small due to dominance of thermal fluctuation over quantum fluctuation and, as a result, the finite size effect is suppressed. Therefore small systems are enough to obtain the thermodynamic limit at high T. Second aspect is long correlation length that persists at low T and small system size does not capture the thermodynamic properties. In this circumstance, the DMRG plays an important role in solving the spectrum of larger system sizes. The calculation of temperature dependent quantities requires partition function $Q(T, N)$ at finite T and it is the Boltzmann sum of all energy levels of finite system size N. However, accurate full spectrum of large systems is beyond the scope of the DMRG method. The advantage of the hybrid ED/DMRG method is that it does not require full spectrum of large systems. At low T, high energy states have exponentially small contribution to the $Q(T, N)$ and it is constructed with Boltzmann sum of all low energy spectrum $E_j(N)$ below cutoff energy $W_C(N)$. Since the DMRG is established to provide accurate ground state and a few low energy excited states for 1D systems, the low T thermodynamics from low excitations is obtained with excellent accuracy. Number of excitation gaps from DMRG is kept large enough in this method such that the finite systems satisfy the thermodynamic limit for a narrow T regime. For example, the maxima of $S_C(T, N)/T$ and $\chi_C(T, N)$ in spin system in Fig. 3.2 of Chapter 3, the merging of $\chi(T, N, N_e)$ of systems with electron number $N_e = 4p$ and $4p + 2$ systems for half filled fermionic system in Fig. 5.1 and Fig. 5.6 and for quarter-filled models in Fig. 5.10 and Fig. 5.11. Any increase of the cutoff energy of the low-lying excitations does not change the thermal properties up to the maxima or the merging points. Progressively larger system sizes are used for the thermodynamic limit at lower T and the low energy excitation gaps required for the partition function at lower T are also smaller. It is the main advantage of this method in reducing the numerical cost for large system size.

The most time-intensive step in this method is the diagonalization of the superblock at each cycle of the DMRG calculations. The time increases linearly with system size since the dimension of the superblock matrix is kept constant. However, the DMRG calculation is limited by the numerical accuracy for large systems with dense low-energy spectrum such as in frustrated spin system in Eq. 3.3 with ferromagnetic nearest neighbor exchange J_1 interaction. The effectiveness of the hybrid method in this difficult regime is discussed in Chapter 3 which sets a benchmark of this method for strongly correlated low dimensional systems.

The results of this method are benchmarked by comparison with well known thermodynamic results of

1D HAF spin-1/2 model and tight binding model and details of the comparisons are discussed in Chapter 3 and Chapter 5. In most of the cases, the method leads to the thermodynamics to low enough T for accurate extrapolation to $T = 0$ except systems with very tiny gaps, e.g., in the BOW phase of EHM model discussed in Chapter 5. The extrapolations in both the spin and fermionic systems agree quite well with the ground state properties which are already known. The analysis of magnetic susceptibility and entropy can help experimentalists to determine magnetic gap in the system.

We have also studied the finite T properties of two well known spin-Peierls (SP) systems: organic TTF-$CuS_4C_4(CF_3)_4$ and inorganic $CuGeO_3$ in Chapter 4. The small displacement of TTF^+ and Cu spin-1/2 ion causes the T dependent structural dimerization in the AFM spin-1/2 chain below the SP transition temperature T_{SP}. Unlike most of the studies in the literature, our analysis of SP transition is not limited to the mean field approach. Since structural dimerization in SP systems for $T < T_{SP}$ limits the correlation length by increasing ST gap, small system size ($N = 32$) is shown to be sufficient to reach the thermodynamic limit in Fig. 4.2 and Fig. 4.3. The anomaly in magnetic susceptibility and INS data near the transition is well explained through our calculation in Chapter 4.

To establish that the hybrid ED/DMRG is a general method we also solve the fermionic models where spin and charge degrees of freedom are active. These models are more complex than spin chains, as the energy spectrum $\{E(N)\}$ of fermionic system depends on the filling $n = N_e/N$ as well as the dimension of the basis $W(N, N_e)$ in finite systems. Finite system of fermions suffers from strong size dependence at $N_e = 4p$ and $4p + 2$ at low T at small values of onsite interaction U. We demonstrate that the merging of $N_e = 4p$ and $4p + 2$ of progressively large systems from above and below eventually leads the thermodynamic limit to low T. The accuracy of this method is benchmarked in Chapter 5 by comparisons to the exact thermodynamic limit for the noninteracting system ($U = 0$) where the DMRG has largest truncation error. We also reproduce $T = 0$ results for half and quarter filled interacting systems.

We conclude that the hybrid ED/DMRG method is a general method for strongly correlated 1D systems and one can apply the hybrid ED/DMRG technique to calculate various thermodynamic properties, and we hope many research groups will be benefited from this method in their respective calculations for 1D systems at finite T.

References

[1] A. W. Sandvik, "Computational studies of quantum spin systems," *AIP Conf. Proc.*, vol. 1297, no. 1, pp. 135–338, 2010.

[2] I. S. Jacobs, J. W. Bray, H. R. Hart, L. V. Interrante, J. S. Kasper, G. D. Watkins, D. E. Prober, and J. C. Bonner, "Spin-Peierls transitions in magnetic donor-acceptor compounds of tetrathiafulvalene (TTF) with bisdithiolene metal complexes," *Phys. Rev. B*, vol. 14, pp. 3036–3051, Oct 1976.

[3] J. W. Bray, L. V. Interrante, I. S. Jacobs, and J. C. Bonner, *The Spin-Peierls Transition*, vol. 3, pp. 353–416. New York: Plenum Press, 1983.

[4] M. Hase, I. Terasaki, and K. Uchinokura, "Observation of the spin-Peierls transition in linear Cu^{2+} (spin-1/2) chains in an inorganic compound $cugeo_3$," *Phys. Rev. Lett.*, vol. 70, pp. 3651–3654, Jun 1993.

[5] M. Hase, I. Terasaki, K. Uchinokura, M. Tokunaga, N. Miura, and H. Obara, "Magnetic phase diagram of the spin-Peierls cuprate $CuGeO_3$," *Phys. Rev. B*, vol. 48, pp. 9616–9619, Oct 1993.

[6] K. Fabricius, A. Klümper, U. Löw, B. Büchner, T. Lorenz, G. Dhalenne, and A. Revcolevschi, "Reexamination of the microscopic couplings of the quasi-one-dimensional antiferromagnet $CuGeO_3$," *Phys. Rev. B*, vol. 57, pp. 1102–1107, Jan 1998.

[7] T. Lorenz, U. Ammerahl, R. Ziemes, B. Büchner, A. Revcolevschi, and G. Dhalenne, "Thermodynamic properties of the incommensurate phase of $CuGeO_3$," *Phys. Rev. B*, vol. 54, pp. R15610–R15613, Dec 1996.

[8] X. Liu, J. Wosnitza, H. Löhneysen, and R. Kremer, "Specific heat of the spin-Peierls compound $CuGeO_3$," *Z. Phys. B*, vol. 98, pp. 163–165, June 1995.

[9] M. Nishi, O. Fujita, and J. Akimitsu, "Neutron-scattering study on the spin-Peierls transition in a quasi-one-dimensional magnet $CuGeO_3$," *Phys. Rev. B*, vol. 50, pp. 6508–6510, Sep 1994.

[10] J.-G. Lussier, S. M. Coad, D. F. McMorrow, and D. M. Paul, "The temperature dependence of the spin - Peierls energy gap in $CuGeO_3$," *J. Phys.: Condens. Matter*, vol. 8, pp. L59–L64, jan 1996.

[11] M. C. Martin, G. Shirane, Y. Fujii, M. Nishi, O. Fujita, J. Akimitsu, M. Hase, and K. Uchinokura, "Temperature dependence of the spin-Peierls energy gap and anomalous line shapes in $CuGeO_3$," *Phys. Rev. B*, vol. 53, pp. R14713–R14716, Jun 1996.

[12] L. P. Regnault, M. Aïn, B. Hennion, G. Dhalenne, and A. Revcolevschi, "Inelastic-neutron-scattering investigation of the spin-Peierls system $CuGeO_3$," *Phys. Rev. B*, vol. 53, pp. 5579–5597, Mar 1996.

[13] M. Arai, M. Fujita, M. Motokawa, J. Akimitsu, and S. M. Bennington, "Quantum spin excitations in the spin-Peierls system $CuGeO_3$," *Phys. Rev. Lett.*, vol. 77, pp. 3649–3652, Oct 1996.

[14] M. Takahashi, "Magnetic Susceptibility for the Half-Filled Hubbard Model," *Progress of Theoretical Physics*, vol. 43, pp. 1619–1619, 06 1970.

[15] S. Glocke, A. Klümper, and J. Sirker, "Half-filled one-dimensional extended Hubbard model: Phase diagram and thermodynamics," *Phys. Rev. B*, vol. 76, p. 155121, Oct 2007.

[16] H. Shiba, "Magnetic Susceptibility at Zero Temperature for the One-Dimensional Hubbard Model," *Phys. Rev. B*, vol. 6, pp. 930–938, Aug 1972.

[17] S.-i. Tomonaga, "Remarks on Bloch's Method of Sound Waves applied to Many-Fermion Problems," *Progress of Theoretical Physics*, vol. 5, pp. 544–569, 07 1950.

[18] J. M. Luttinger, "An exactly soluble model of a many-fermion system," *Journal of Mathematical Physics*, vol. 4, no. 9, pp. 1154–1162, 1963.

[19] D. C. Mattis and E. H. Lieb, "Exact solution of a many-fermion system and its associated boson field," *Journal of Mathematical Physics*, vol. 6, no. 2, pp. 304–312, 1965.

[20] T. Giamarchi, *Quantum Physics in One Dimension*. A Clarendon Press Publication, 2004.

[21] Z. G. Soos, A. Parvej, and M. Kumar, "Numerical study of incommensurate and decoupled phases of spin-1/2 chains with isotropic exchange J_1 , J_2 between first and second neighbors," *J. Phys.: Condens. Matter*, vol. 28, no. 17, p. 175603, 2016.

[22] S. E. Dutton, M. Kumar, M. Mourigal, Z. G. Soos, J.-J. Wen, C. L. Broholm, N. H. Andersen, Q. Huang, M. Zbiri, R. Toft-Petersen, and R. J. Cava, "Quantum spin liquid in frustrated one-dimensional $LiCuSbO_4$," *Phys. Rev. Lett.*, vol. 108, p. 187206, 2012.

[23] A. Parvej and M. Kumar, "Multipolar phase in frustrated spin-1/2 and spin-1 chains," *Phys. Rev. B*, vol. 96, p. 054413, 2017.

[24] S. K. Saha, M. S. Roy, M. Kumar, and Z. G. Soos, "Modeling the spin-Peierls transition of spin-$\frac{1}{2}$ chains with correlated states: J_1–J_2 model, $CuGeO_3$, and TTF $-$ $CuS_4C_4(CF_3)_4$," *Phys. Rev. B*, vol. 101, p. 054411, Feb 2020.

[25] M. Kumar, B. J. Topham, R. Yu, Q. B. D. Ha, and Z. G. Soos, "Magnetic susceptibility of alkali-tetracyanoquinodimethane salts and extended hubbard models with bond order and charge density wave phases," *The Journal of Chemical Physics*, vol. 134, no. 23, p. 234304, 2011.

[26] G. D. Mahan, *Many-Particle Physics*. Springer US, 3 ed., 2000.

[27] M. Kumar and Z. G. Soos, "Decoupled phase of frustrated spin-$\frac{1}{2}$ antiferromagnetic chains with and without long-range order in the ground state," *Phys. Rev. B*, vol. 88, p. 134412, 2013.

[28] T. Hamada, J.-i. Kane, S.-i. Nakagawa, and Y. Natsume, " Exact Solution of Ground State for Uniformly Distributed RVB in One-Dimensional Spin-1/2 Heisenberg Systems with Frustration ," *J. Phys. Soc. Jpn.*, vol. 57, no. 6, pp. 1891–1894, 1988.

[29] J. Sirker, V. Y. Krivnov, D. V. Dmitriev, A. Herzog, O. Janson, S. Nishimoto, S.-L. Drechsler, and J. Richter, "$J_1 - J_2$ Heisenberg model at and close to its $z = 4$ quantum critical point," *Phys. Rev. B*, vol. 84, p. 144403, 2011.

[30] K. Okamoto and K. Nomura, "Fluid-dimer critical point in $S = 1\,2$ antiferromagnetic Heisenberg chain with next nearest neighbor interactions," *Phys. Lett. A*, vol. 169, no. 6, pp. 433 – 437, 1992.

[31] C. K. Majumdar and D. K. Ghosh, "On Next-Nearest-Neighbor Interaction in Linear Chain. II," *J. Math. Phys.*, vol. 10, no. 8, pp. 1399–1402, 1969.

[32] Z. G. Soos, "Theory of π-molecular charge-transfer crystals," *Annual Review of Physical Chemistry*, vol. 25, no. 1, pp. 121–153, 1974.

[33] J. S. Miller, ed., *Extended Linear Chain Compounds*, vol. 3. New York: Plenum Press, 1983.

[34] D. Jérome, "Organic conductors: From charge density wave TTF – TCNQ to superconducting $(TMTSF)_2\,PF_6$," *Chem. Rev.*, vol. 104, pp. 5565–5592, October 2004.

[35] A. J. Heeger, S. Kivelson, J. R. Schrieffer, and W. P. Su, "Solitons in conducting polymers," *Rev. Mod. Phys.*, vol. 60, pp. 781–850, Jul 1988.

[36] M. Nakamura, "Tricritical behavior in the extended Hubbard chains," *Phys. Rev. B*, vol. 61, pp. 16377–16392, Jun 2000.

[37] M. Kumar, S. Ramasesha, and Z. G. Soos, "Tuning the bond-order wave phase in the half-filled extended Hubbard model," *Phys. Rev. B*, vol. 79, p. 035102, Jan 2009.

[38] M. Kumar, S. Ramasesha, R. A. P. jr., and Z. G. Soos, "Dimerization transition of alkali-TCNQ salts: Charge degrees of freedom near the CDW boundary," *EPL (Europhysics Letters)*, vol. 83, p. 37001, jun 2008.

[39] A. Girlando, A. Painelli, S. A. Bewick, and Z. G. Soos, "Charge fluctuations and electron–phonon coupling in organic charge-transfer salts with neutral–ionic and peierls transitions," *Synthetic Metals*, vol. 141, no. 1, pp. 129 – 138, 2004. Michael J. Rice Memorial Festschrift.

[40] T. Ohama, H. Yasuoka, M. Isobe, and Y. Ueda, "Mixed valency and charge ordering in $\alpha^{'}-NaV_2O_5$," *Phys. Rev. B*, vol. 59, pp. 3299–3302, Feb 1999.

[41] F. Nad, P. Monceau, C. Carcel, and J. M. Fabre, "Dielectric response of the charge-induced correlated state in the quasi-one-dimensional conductor $(TMTTF)_2PF_6$," *Phys. Rev. B*, vol. 62, pp. 1753–1756, Jul 2000.

[42] D. S. Chow, F. Zamborszky, B. Alavi, D. J. Tantillo, A. Baur, C. A. Merlic, and S. E. Brown, "Charge ordering in the tmttf family of molecular conductors," *Phys. Rev. Lett.*, vol. 85, pp. 1698–1701, Aug 2000.

[43] H. Seo and H. Fukuyama, "Charge ordering and spin gap in NaV_2O_5," *Journal of the Physical Society of Japan*, vol. 67, no. 8, pp. 2602–2605, 1998.

[44] S. Mazumdar, S. Ramasesha, R. Torsten Clay, and D. K. Campbell, "Theory of coexisting charge- and spin-density waves in $(TMTTF)_2Br$, $(TMTSF)_2PF_6$, and $\alpha - (BEDT - TTF)_2MHg(SCN)_4$," *Phys. Rev. Lett.*, vol. 82, pp. 1522–1525, Feb 1999.

[45] H. Seo and H. Fukuyama, "Antiferromagnetic phases of one-dimensional quarter-filled organic conductors," *Journal of the Physical Society of Japan*, vol. 66, no. 5, pp. 1249–1252, 1997.

[46] F. Mila, "Deducing correlation parameters from optical conductivity in the bechgaard salts," *Phys. Rev. B*, vol. 52, pp. 4788–4793, Aug 1995.

[47] C. Schuster and U. Schwingenschlögl, "One-dimensional hubbard model at quarter filling on periodic potentials," *Phys. Rev. B*, vol. 75, p. 045124, Jan 2007.

[48] R. E. Peierls, *Quantum Theory of Solids*. Oxford University Press, London, 1955.

[49] M. Kumar, A. Parvej, and Z. G. Soos, "Level crossing, spin structure factor and quantum phases of the frustrated spin-1/2 chain with first and second neighbor exchange," *Journal of Physics: Condensed Matter*, vol. 27, p. 316001, July 2015.

[50] D. Dey, M. Kumar, S. E. Dutton, R. J. Cava, and Z. G. Soos, "Spin-specific heat determination of the ratio of competing first- and second-neighbor exchange interactions in frustrated spin-$\frac{1}{2}$ chains," *Phys. Rev. B*, vol. 97, p. 064407, 2018.

[51] D. Maiti, D. Dey, and M. Kumar, "Frustrated spin-1/2 ladder with ferro- and antiferromagnetic legs," *Journal of Magnetism and Magnetic Materials*, vol. 446, pp. 170–176, 2018.

[52] M. Kumar, S. Ramasesha, and Z. G. Soos, "Bond-order wave phase, spin solitons, and thermodynamics of a frustrated linear spin-$\frac{1}{2}$ Heisenberg antiferromagnet," *Phys. Rev. B*, vol. 81, p. 054413, Feb 2010.

[53] K. G. Wilson, "The renormalization group: Critical phenomena and the kondo problem," *Rev. Mod. Phys.*, vol. 47, pp. 773–840, Oct 1975.

[54] S. R. White, "Density matrix formulation for quantum renormalization groups," *Phys. Rev. Lett.*, vol. 69, pp. 2863–2866, Nov 1992.

[55] U. Schollwöck, "The density-matrix renormalization group in the age of matrix product states," *Annals of Physics*, vol. 326, no. 1, pp. 96 – 192, 2011. January 2011 Special Issue.

[56] D. C. Handscomb, "A monte carlo method applied to the heisenberg ferromagnet," *Mathematical Proceedings of the Cambridge Philosophical Society*, vol. 60, no. 1, p. 115–122, 1964.

[57] M. Suzuki, "Relationship between d-Dimensional Quantal Spin Systems and (d+1)-Dimensional Ising Systems: Equivalence, Critical Exponents and Systematic Approximants of the Partition Function and Spin Correlations," *Progress of Theoretical Physics*, vol. 56, pp. 1454–1469, 11 1976.

[58] B. B. Beard and U.-J. Wiese, "Simulations of discrete quantum systems in continuous euclidean time," *Phys. Rev. Lett.*, vol. 77, pp. 5130–5133, Dec 1996.

[59] A. W. Sandvik and J. Kurkijärvi, "Quantum monte carlo simulation method for spin systems," *Phys. Rev. B*, vol. 43, pp. 5950–5961, Mar 1991.

[60] P. Henelius, P. Fröbrich, P. J. Kuntz, C. Timm, and P. J. Jensen, "Quantum monte carlo simulation of thin magnetic films," *Phys. Rev. B*, vol. 66, p. 094407, Sep 2002.

[61] A. W. Sandvik, "Stochastic series expansion method for quantum ising models with arbitrary interactions," *Phys. Rev. E*, vol. 68, p. 056701, Nov 2003.

[62] S. Wessel, F. Alet, M. Troyer, and G. G. Batrouni, "Quantum monte carlo simulations of confined bosonic atoms in optical lattices," *Phys. Rev. A*, vol. 70, p. 053615, Nov 2004.

[63] R. G. Melko, *Stochastic Series Expansion Quantum Monte Carlo*, vol. 176, pp. 185–206. Springer, Berlin, Heidelberg: Springer Series in Solid-State Sciences, 2013.

[64] H. G. Evertz, "The loop algorithm," *Advances in Physics*, vol. 52, no. 1, pp. 1–66, 2003.

[65] O. F. Syljuåsen and A. W. Sandvik, "Quantum monte carlo with directed loops," *Phys. Rev. E*, vol. 66, p. 046701, Oct 2002.

[66] R. H. Swendsen and J.-S. Wang, "Nonuniversal critical dynamics in monte carlo simulations," *Phys. Rev. Lett.*, vol. 58, pp. 86–88, Jan 1987.

[67] S. R. White, "Density-matrix algorithms for quantum renormalization groups," *Phys. Rev. B*, vol. 48, pp. 10345–10356, Oct 1993.

[68] U. Schollwöck, "The density-matrix renormalization group," *Rev. Mod. Phys.*, vol. 77, pp. 259–315, Apr 2005.

[69] K. A. Hallberg, "New trends in density matrix renormalization," *Adv. Phys.*, vol. 55, no. 5-6, pp. 477–526, 2006.

[70] T. Nishino, "Density matrix renormalization group method for 2d classical models," *J. Phys. Soc. Jpn.*, vol. 64, no. 10, pp. 3598–3601, 1995.

[71] R. J. Bursill, T. Xiang, and G. A. Gehring, "The density matrix renormalization group for a quantum spin chain at non-zero temperature," *Journal of Physics: Condensed Matter*, vol. 8, pp. L583–L590, sep 1996.

[72] J. Sirker, "Thermodynamics of multiferroic spin chains," *Phys. Rev. B*, vol. 81, p. 014419, 2010.

[73] X. Wang and T. Xiang, "Transfer-matrix density-matrix renormalization-group theory for thermodynamics of one-dimensional quantum systems," *Phys. Rev. B*, vol. 56, pp. 5061–5064, Sep 1997.

[74] H. T. Lu, Y. J. Wang, S. Qin, and T. Xiang, "Zigzag spin chains with antiferromagnetic-ferromagnetic interactions: Transfer-matrix renormalization group study," *Phys. Rev. B*, vol. 74, p. 134425, 2006.

[75] Sirker, J. and Klümper, A., "Temperature-driven crossover phenomena in the correlation lengths of the one-dimensional -j model," *Europhys. Lett.*, vol. 60, no. 2, pp. 262–268, 2002.

[76] T. Xiang, "Thermodynamics of quantum heisenberg spin chains," *Phys. Rev. B*, vol. 58, pp. 9142–9149, 1998.

[77] A. Kemper and A. Schadschneider, "Thermodynamic properties and thermal correlation lengths of a hubbard model with bond-charge interaction," *Phys. Rev. B*, vol. 68, p. 235102, Dec 2003.

[78] A. E. Feiguin and S. R. White, "Finite-temperature density matrix renormalization using an enlarged hilbert space," *Phys. Rev. B*, vol. 72, p. 220401, Dec 2005.

[79] S. R. White and A. E. Feiguin, "Real-time evolution using the density matrix renormalization group," *Phys. Rev. Lett.*, vol. 93, p. 076401, Aug 2004.

[80] A. E. Feiguin and S. R. White, "Time-step targeting methods for real-time dynamics using the density matrix renormalization group," *Phys. Rev. B*, vol. 72, p. 020404, Jul 2005.

[81] S. K. Saha, D. Dey, M. Kumar, and Z. G. Soos, "Hybrid exact diagonalization and density matrix renormalization group approach to the thermodynamics of one-dimensional quantum models," *Phys. Rev. B*, vol. 99, p. 195144, May 2019.

[82] S. K. Saha, M. Kumar, and Z. G. Soos, "Bond-bond correlations, gap relations and thermodynamics of spin-1/2 chains with spin-Peierls transitions and bond-order-wave phases," *Journal of Magnetism and Magnetic Materials*, vol. 519, p. 167472, 2021.

[83] S. K. Saha, D. Maiti, M. Kumar, and Z. G. Soos, "Density matrix renormalization group approach to the low temperature thermodynamics of correlated 1d fermionic models," 2021.

[84] C. Lanczos, "An iteration method for the solution of the eigenvalue problem of linear differential and integral operators," *J. Res. Natl. Bur. Stand.*, vol. 45, pp. 255–282, 1950.

[85] C. Lanczos, "Solution of systems of linear equations by minimized iterations," *J. Res. Natl. Bur. Stand.*, vol. 49, pp. 33–53, 1952.

[86] E. R. Davidson, "The iterative calculation of a few of the lowest eigenvalues and corresponding eigenvectors of large real-symmetric matrices," *Journal of Computational Physics*, vol. 17, no. 1, pp. 87–94, 1975.

[87] E. R. Davidson and W. J. Thompson, "Monster matrices: Their eigenvalues and eigenvectors," *Computers in Physics*, vol. 7, no. 5, pp. 519–522, 1993.

[88] C. W. Murray, S. C. Racine, and E. R. Davidson, "Improved algorithms for the lowest few eigenvalues and associated eigenvectors of large matrices," *Journal of Computational Physics*, vol. 103, no. 2, pp. 382–389, 1992.

[89] S. Rettrup, "An iterative method for calculating several of the extreme eigensolutions of large real non-symmetric matrices," *Journal of Computational Physics*, vol. 45, no. 1, pp. 100–107, 1982.

[90] U. Schollwöck, "The density-matrix renormalization group," *Rev. Mod. Phys.*, vol. 77, pp. 259–315, Apr 2005.

[91] S. R. White and D. A. Huse, "Numerical renormalization-group study of low-lying eigenstates of the antiferromagnetic $S = 1$ heisenberg chain," *Phys. Rev. B*, vol. 48, pp. 3844–3852, Aug 1993.

[92] S. R. White, "Density matrix renormalization group algorithms with a single center site," *Phys. Rev. B*, vol. 72, p. 180403, Nov 2005.

[93] M. Kumar, S. Ramasesha, D. Sen, and Z. G. Soos, "Scaling exponents in spin-$\frac{1}{2}$ Heisenberg chains with dimerization and frustration studied with the density-matrix renormalization group," *Phys. Rev. B*, vol. 75, p. 052404, Feb 2007.

[94] D. Dey, M. Kumar, and Z. G. Soos, "Boundary-induced spin-density waves in linear heisenberg antiferromagnetic spin chains with $s \geq 1$," *Phys. Rev. B*, vol. 94, p. 144417, Oct 2016.

[95] R. Chitra, S. Pati, H. R. Krishnamurthy, D. Sen, and S. Ramasesha, "Density-matrix renormalization-group studies of the spin-1/2 heisenberg system with dimerization and frustration," *Phys. Rev. B*, vol. 52, pp. 6581–6587, Sep 1995.

[96] S. R. White and I. Affleck, "Dimerization and incommensurate spiral spin correlations in the zigzag spin chain: Analogies to the kondo lattice," *Phys. Rev. B*, vol. 54, pp. 9862–9869, Oct 1996.

[97] R. M. Noack, S. R. White, and D. J. Scalapino, "The density-matrix renormalization group for fermion systems," in *Computer Simulation Studies in Condensed-Matter Physics VII* (D. P. Landau, K. K. Mon, and H.-B. Schüttler, eds.), (Berlin, Heidelberg), pp. 85–98, Springer Berlin Heidelberg, 1994.

[98] S. R. White, R. M. Noack, and D. J. Scalapino, "Density matrix renormalization group calculations for doped hubbard ladders," *Journal of Low Temperature Physics*, vol. 99, pp. 593–598, 1995.

[99] M. Kumar, A. Parvej, S. Thomas, S. Ramasesha, and Z. G. Soos, "Efficient density matrix renormalization group algorithm to study y junctions with integer and half-integer spin," *Phys. Rev. B*, vol. 93, p. 075107, Feb 2016.

[100] M. Singh Roy, M. Kumar, J. D. Sau, and S. Tewari, "Fermion parity gap and exponential ground state degeneracy of the one-dimensional fermi gas with intrinsic attractive interaction," *Phys. Rev. B*, vol. 102, p. 125135, Sep 2020.

[101] M. Singh Roy, M. Kumar, and S. Das, "Tunneling density of states in a y junction of tomonaga-luttinger liquid wires: A density matrix renormalization group study," *Phys. Rev. B*, vol. 102, p. 035130, Jul 2020.

[102] T. D. Kühner, S. R. White, and H. Monien, "One-dimensional bose-hubbard model with nearest-neighbor interaction," *Phys. Rev. B*, vol. 61, pp. 12474–12489, May 2000.

[103] M. Kumar, S. Sarkar, and S. Ramasesha, "Supersolid phase in one-dimensional bose–hubbard model with extended range interactions: Dmrg and field theoretic study at different densities," *International Journal of Modern Physics B*, vol. 25, no. 01, pp. 159–169, 2011.

[104] M. Qin, C.-M. Chung, H. Shi, E. Vitali, C. Hubig, U. Schollwöck, S. R. White, and S. Zhang, "Absence of superconductivity in the pure two-dimensional hubbard model," *Phys. Rev. X*, vol. 10, p. 031016, Jul 2020.

[105] M. Kumar, Z. G. Soos, D. Sen, and S. Ramasesha, "Modified density matrix renormalization group algorithm for the zigzag spin-$\frac{1}{2}$ chain with frustrated antiferromagnetic exchange: Comparison with field theory at large J_2/J_1," *Phys. Rev. B*, vol. 81, p. 104406, Mar 2010.

[106] M. Kumar, S. Ramasesha, and Z. G. Soos, "Density matrix renormalization group algorithm for bethe lattices of spin-$\frac{1}{2}$ or spin-1 sites with heisenberg antiferromagnetic exchange," *Phys. Rev. B*, vol. 85, p. 134415, Apr 2012.

[107] D. Dey, D. Maiti, and M. Kumar, "An efficient density matrix renormalization group algorithm for chains with periodic boundary condition," *Papers in Physics*, vol. 8, 2016.

[108] S. R. White and R. M. Noack, "Real-space quantum renormalization groups," *Phys. Rev. Lett.*, vol. 68, pp. 3487–3490, Jun 1992.

[109] P. Pippan, S. R. White, and H. G. Evertz, "Efficient matrix-product state method for periodic boundary conditions," *Phys. Rev. B*, vol. 81, p. 081103, Feb 2010.

[110] H. Bethe, "Zur theorie der metalle," *Z. Phys.*, vol. 71, no. 3, pp. 205–226, 1931.

[111] L. Hulthén, "Über das Austauschproblem eines Kristalls.," *Ark. Mat. Astron. Fys.*, vol. 26, no. 11, p. 106, 1938.

[112] D. C. Johnston, R. K. Kremer, M. Troyer, X. Wang, A. Klümper, S. L. Bud'ko, A. F. Panchula, and P. C. Canfield, "Thermodynamics of spin $S = 1/2$ antiferromagnetic uniform and alternating-exchange Heisenberg chains," *Phys. Rev. B*, vol. 61, pp. 9558–9606, 2000.

[113] A. V. Chubukov, "Chiral, nematic, and dimer states in quantum spin chains," *Phys. Rev. B*, vol. 44, pp. 4693–4696, 1991.

[114] T. Hikihara, L. Kecke, T. Momoi, and A. Furusaki, "Vector chiral and multipolar orders in the spin-$\frac{1}{2}$ frustrated ferromagnetic chain in magnetic field," *Phys. Rev. B*, vol. 78, p. 144404, Oct 2008.

[115] L. de Jongh and A. Miedema, "Experiments on simple magnetic model systems," *Adv. Phys.*, vol. 23, no. 1, pp. 1–260, 1974.

[116] M. Hase, H. Kuroe, K. Ozawa, O. Suzuki, H. Kitazawa, G. Kido, and T. Sekine, "Magnetic properties of $Rb_2Cu_2Mo_3O_{12}$ including a one-dimensional spin-1/2 Heisenberg system with ferromagnetic first-nearest-neighbor and antiferromagnetic second-nearest-neighbor exchange interactions," *Phys. Rev. B*, vol. 70, p. 104426, Sep 2004.

[117] S.-L. Drechsler, O. Volkova, A. N. Vasiliev, N. Tristan, J. Richter, M. Schmitt, H. Rosner, J. Málek, R. Klingeler, A. A. Zvyagin, and B. Büchner, "Frustrated cuprate route from antiferromagnetic to ferromagnetic spin-$\frac{1}{2}$ Heisenberg chains: Li_2ZrCuO_4 as a missing link near the quantum critical point," *Phys. Rev. Lett.*, vol. 98, p. 077202, Feb 2007.

[118] T. Masuda, A. Zheludev, A. Bush, M. Markina, and A. Vasiliev, "Competition between helimagnetism and commensurate quantum spin correlations in $LiCu_2O_2$," *Phys. Rev. Lett.*, vol. 92, p. 177201, 2004.

[119] S. Park, Y. J. Choi, C. L. Zhang, and S.-W. Cheong, "Ferroelectricity in an $S = 1/2$ chain cuprate," *Phys. Rev. Lett.*, vol. 98, p. 057601, 2007.

[120] A. U. B. Wolter, F. Lipps, M. Schäpers, S.-L. Drechsler, S. Nishimoto, R. Vogel, V. Kataev, B. Büchner, H. Rosner, M. Schmitt, M. Uhlarz, Y. Skourski, J. Wosnitza, S. Süllow, and K. C. Rule, "Magnetic properties and exchange integrals of the frustrated chain cuprate linarite $PbCuSO_4(OH)_2$," *Phys. Rev. B*, vol. 85, p. 014407, 2012.

[121] M. Kumar and Z. G. Soos, "Spin-parity and broken symmetry in finite spin-$\frac{1}{2}$ chains with frustrated exchange: Quantum transition from high to low spin," *Phys. Rev. B*, vol. 85, p. 144415, 2012.

[122] D. Allen and D. Sénéchal, "Non-abelian bosonization of the frustrated antiferromagnetic spin-1/2 chain," *Phys. Rev. B*, vol. 55, pp. 299–308, 1997.

[123] C. Itoi and S. Qin, "Strongly reduced gap in the zigzag spin chain with a ferromagnetic interchain coupling," *Phys. Rev. B*, vol. 63, p. 224423, 2001.

[124] Y.-K. Huang, P. Chen, and Y.-J. Kao, "Accurate computation of low-temperature thermodynamics for quantum spin chains," *Phys. Rev. B*, vol. 86, p. 235102, Dec 2012.

[125] F. Heidrich-Meisner, A. Honecker, and T. Vekua, "Frustrated ferromagnetic spin-$\frac{1}{2}$ chain in a magnetic field: The phase diagram and thermodynamic properties," *Phys. Rev. B*, vol. 74, p. 020403, 2006.

[126] P. Jordan and E. Wigner, "Über das paulische äquivalenzverbot," *Z. Physik*, vol. 47, pp. 631–651, 1928.

[127] J. Sudan, A. Lüscher, and A. M. Läuchli, "Emergent multipolar spin correlations in a fluctuating spiral: The frustrated ferromagnetic spin-$\frac{1}{2}$ Heisenberg chain in a magnetic field," *Phys. Rev. B*, vol. 80, p. 140402, Oct 2009.

[128] J. Riera and A. Dobry, "Magnetic susceptibility in the spin-Peierls system $CuGeO_3$," *Phys. Rev. B*, vol. 51, pp. 16098–16102, Jun 1995.

[129] K. Uchinokura, "Spin-Peierls transition in $CuGeO_3$ and impurity-induced ordered phases in low-dimensional spin-gap systems," *J. Phys.: Condens. Matter*, vol. 14, pp. R195–R237, mar 2002.

[130] J. C. Bonner and M. E. Fisher, "Linear magnetic chains with anisotropic coupling," *Phys. Rev.*, vol. 135, pp. A640–A658, 1964.

[131] W. P. Su, J. R. Schrieffer, and A. J. Heeger, "Soliton excitations in polyacetylene," *Phys. Rev. B*, vol. 22, pp. 2099–2111, Aug 1980.

[132] G. Beni and P. Pincus, "Instability of the Uniform Antiferromagnetic Chain. I. XY Model in the Adiabatic Approximation," *J. Chem. Phys.*, vol. 57, no. 8, pp. 3531–3534, 1972.

[133] L. Del Freo, A. Painelli, and Z. G. Soos, "Giant infrared intensity of the Peierls mode at the neutral-ionic phase transition," *Phys. Rev. Lett.*, vol. 89, p. 027402, Jun 2002.

[134] T. Barnes, J. Riera, and D. A. Tennant, "S $= \frac{1}{2}$ alternating chain using multiprecision methods," *Phys. Rev. B*, vol. 59, pp. 11384–11397, May 1999.

[135] S. K. Saha, M. Kumar, and Z. G. Soos, "Spin-Peierls transition of the dimer phase of the $J_1 - J_2$ model: Energy cusp and $CuGeO_3$ thermodynamics," 2019.

[136] M. C. Cross and D. S. Fisher, "A new theory of the spin-Peierls transition with special relevance to the experiments on TTFCuBDT," *Phys. Rev. B*, vol. 19, pp. 402–419, Jan 1979.

[137] M. Hidaka, M. Hatae, I. Yamada, M. Nishi, and J. Akimitsu, "Re-examination of the room temperature crystal structure of $CuGeO_3$ by x-ray diffraction experiments: observation of new superlattice reflections," *J. Phys.: Condens. Matter*, vol. 9, pp. 809–824, jan 1997.

[138] G. Castilla, S. Chakravarty, and V. J. Emery, "Quantum Magnetism of $CuGeO_3$," *Phys. Rev. Lett.*, vol. 75, pp. 1823–1826, Aug 1995.

[139] G. Bouzerar, O. Legeza, and T. Ziman, "Minimal model to describe the magnetism of $CuGeO_3$," *Phys. Rev. B*, vol. 60, pp. 15278–15284, Dec 1999.

[140] T. Wei, A. J. Heeger, M. B. Salamon, and G. E. Delker, "Specific heat studies of the spin-Peierls transition," *Solid State Commun.*, vol. 21, no. 6, pp. 595–598, 1977.

[141] G. Müller, H. Thomas, H. Beck, and J. C. Bonner, "Quantum spin dynamics of the antiferromagnetic linear chain in zero and nonzero magnetic field," *Phys. Rev. B*, vol. 24, pp. 1429–1467, Aug 1981.

[142] L. Faddeev and L. Takhtajan, "What is the spin of a spin wave?," *Physics Letters A*, vol. 85, no. 6, pp. 375 – 377, 1981.

[143] J. des Cloizeaux and J. J. Pearson, "Spin-wave spectrum of the antiferromagnetic linear chain," *Phys. Rev.*, vol. 128, pp. 2131–2135, Dec 1962.

[144] M. Karbach, G. Müller, A. H. Bougourzi, A. Fledderjohann, and K.-H. Mütter, "Two-spinon dynamic structure factor of the one-dimensional s= Heisenberg antiferromagnet," *Phys. Rev. B*, vol. 55, pp. 12510–12517, May 1997.

[145] M. Mourigal, M. Enderle, A. Klöpperpieper, J.-S. Caux, A. Stunault, and H. M. Rønnow, "Fractional spinon excitations in the quantum Heisenberg antiferromagnetic chain," *Nature Physics*, vol. 9, pp. 435–441, 2013.

[146] I. Affleck, D. Gepner, H. J. Schulz, and T. Ziman, "Critical behaviour of spin-s heisenberg antiferromagnetic chains: analytic and numerical results," *Journal of Physics A: Mathematical and General*, vol. 22, no. 5, p. 511, 1989.

[147] S. Ramasesha and Z. G. Soos, "Correlated states in linear polyenes, radicals, and ions: Exact ppp transition moments and spin densities," *J. Chem. Phys.*, vol. 80, no. 7, pp. 3278–3287, 1984.

[148] M. Nakamura, "Tricritical behavior in the extended hubbard chains," *Phys. Rev. B*, vol. 61, pp. 16377–16392, Jun 2000.

[149] P. Sengupta, A. W. Sandvik, and D. K. Campbell, "Bond-order-wave phase and quantum phase transitions in the one-dimensional extended hubbard model," *Phys. Rev. B*, vol. 65, p. 155113, Apr 2002.

[150] Z. G. Soos, "Theory of π-molecular charge-transfer crystals," *Annual Review of Physical Chemistry*, vol. 25, no. 1, pp. 121–153, 1974.

[151] M. J. Rice, "Towards the experimental determination of the fundamental microscopic parameters of organic ion-radical compounds," *Solid State Communications*, vol. 31, no. 2, pp. 93 – 98, 1979.

[152] R. Bozio and C. Pecile, "Phase transitions of (1:1) alkaline salts of tcnq as studied by vibronic intensity enhancement in the infrared spectra," *The Journal of Chemical Physics*, vol. 67, no. 9, pp. 3864–3868, 1977.

[153] A. Girlando, A. Painelli, and C. Pecile, "Molecular vibration analysis of lonicity and phase transition in tmpd-tcnq (1:1) charge transfer salt," *Molecular Crystals and Liquid Crystals*, vol. 112, no. 3-4, pp. 325–343, 1984.

[154] T. M. McQueen, D. M. Ho, C. J. Cahua, R. J. Cava, R. A. Pascal, and Z. G. Soos, "Realization of the bond order wave (bow) phase of extended hubbard models in rb–tcnq(ii)," *Chemical Physics Letters*, vol. 475, no. 1, pp. 44 – 48, 2009.

[155] J.-P. Pouget, P. Foury-Leylekian, and M. Almeida, "Peierls and Spin-Peierls Instabilities in the $Per_2[M(mnt)_2]$ Series of One-Dimensional Organic Conductors; Experimental Realization of a 1D Kondo Lattice for M = Pd, Ni and Pt ," *Magnetochemistry*, vol. 3, no. 1, 2017.

[156] A. Painelli and A. Girlando, eds., *The Neutral-Ionic Phase Transition*, Crystals 7, 2017.

[157] Q. J. Harris, Q. Feng, R. J. Birgeneau, K. Hirota, K. Kakurai, J. E. Lorenzo, G. Shirane, M. Hase, K. Uchinokura, H. Kojima, I. Tanaka, and Y. Shibuya, "Thermal contraction at the spin-Peierls transition in $CuGeO_3$," *Phys. Rev. B*, vol. 50, pp. 12606–12610, Nov 1994.

[158] M. Honda, T. Shibata, K. Kindo, S. Sugai, T. Takeuchi, and H. Hori, "Electron spin resonance in one-dimensional antiferromagnet $CuGeO_3$," *J. Phys. Soc. Jpn.*, vol. 65, no. 3, pp. 691–694, 1996.

[159] E. H. Lieb and F. Y. Wu, "Absence of mott transition in an exact solution of the short-range, one-band model in one dimension," *Phys. Rev. Lett.*, vol. 20, pp. 1445–1448, Jun 1968.

[160] G. Jüttner, A. Klümper, and J. Suzuki, "The Hubbard chain at finite temperatures: ab initio calculations of Tomonaga-Luttinger liquid properties," *Nuclear Physics B*, vol. 522, no. 3, pp. 471 – 502, 1998.

[161] S. K. Saha, M. S. Roy, M. Kumar, and Z. G. Soos, "Modeling the spin-peierls transition of spin-$\frac{1}{2}$ chains with correlated states: J_1–J_2 model, cugeo$_3$, and TTF – –cus$_4$c$_4$(CF$_3$)$_4$," *Phys. Rev. B*, vol. 101, p. 054411, Feb 2020.

[162] D. J. Klein and W. A. Seitz, "Perturbation expansion of the linear Hubbard model," *Phys. Rev. B*, vol. 8, pp. 2236–2247, Sep 1973.

[163] P. G. J. van Dongen, "Extended Hubbard model at strong coupling," *Phys. Rev. B*, vol. 49, pp. 7904–7915, Mar 1994.

[164] M. Kumar and Z. G. Soos, "Bond-order wave phase of the extended Hubbard model: Electronic solitons, paramagnetism, and coupling to Peierls and Holstein phonons," *Phys. Rev. B*, vol. 82, p. 155144, Oct 2010.